

# **Finite-friction least-thickness self-standing domains of symmetric circular masonry arches.**

## **Part III: Complementary representations, extremal conditions and collapse multiplicity**

Giuseppe COCCHETTI<sup>1,2</sup>, Egidio RIZZI<sup>2,\*</sup>

<sup>1</sup>Politecnico di Milano, Dipartimento di Ingegneria Civile e Ambientale,  
piazza Leonardo da Vinci 32, I-20133 MILANO, Italy

<sup>2</sup>Università degli studi di Bergamo, Dipartimento di Ingegneria e Scienze Applicate,  
viale Guglielmo Marconi 5, I-24044 DALMINE (BG), Italy

\*Corresponding Author: egidio.rizzi@unibg.it

Accepted Preprint: 28 July 2025

### **Abstract**

This work completes an analytical investigation on the role of finite (Coulomb) friction, in the classical “Couplet-Heyman problem” of least-thickness optimization of self-standing symmetric circular masonry arches. Following a source (Part I) companion work, considering classical, approximate Heyman-like uniform self-weight distribution along geometrical centreline, and a Part II addendum, dedicated to the generalization to the true Milankovitch-like uniform self-weight distribution, accounting for the real centres of gravity of the ideal wedge-shaped infinitesimal chunks of the continuous arch, it highlights, for the latter real distribution, diverse final key aspects, for a comprehensive mathematical and physical interpretation. Namely: (a) the complete two- and three-dimensional representation maps of all characteristic solution variables as a function of geometrical and friction parameters are outlined, to show the rich, multi-faceted mechanical features of the solution in terms of physical states; (b) the peculiar extremal conditions for intrinsic non-dimensional horizontal thrust and inner failure joint angular positions are newly derived, at variable inherent friction coefficient, to inspect how friction may affect such self-supporting abilities, with respect to typical underlying purely-rotational collapse modes with no sliding failure at high or infinite friction; (c) the mathematical multiplicity of the collapse states at the interfaces of the failure domains are analyzed, to unveil distinctive kinematical characteristics of the feasible collapse modes. The analytical achievements, corroborated by a separate numerical experimentation, validation and illustration, by a home-made Complementarity Problem/Mathematical Programming (CP/MP) implementation, allow for a full perception of the problem at hand, in the Mechanics (statics) of masonry arches, and specific related role of finite friction, in providing crucial self-bearing structural capacity.

*Keywords:* (*symmetric circular*) *masonry arches*; *Couplet-Heyman problem*; *least thickness*; *collapse modes*; *finite friction*; *analytical 2D and 3D state maps*; *maximum horizontal thrust*; *widest inner-joint angular positions*; *collapse multiplicity*.

# 1 Introduction

This paper retakes, and completes, a recent investigation on the role that finite (Coulomb) friction shall assume in contributing to the self-supporting capacity of masonry arches, within the classical “Couplet-Heyman problem” of least-thickness structural optimization of (symmetric circular) continuous masonry arches. Coming from the usual purely-rotational solution relying on high-enough or infinite friction, up to prevent sliding failure (third classical Heyman hypothesis), possible joint-sliding onset is foreseen, to unveil the possible appearance of collapse modes involving rotation and/or sliding.

Along the much recent, contemporary seminal work, on the “rational” analysis of the Mechanics of masonry arches, in the vein of M. Milankovitch [1, 2] and J. Heyman [3, 4] pioneering contributions, and of various other attempts to the dedicated literature, where different graphical-analytical and numerical strategies have been developed and employed [5–20], including specifically within the context of finite-friction effects [21–39], moreover relying on previous dedicated work by the Authors on the specific topic [40–45] (and therein cited further external literature framing and references), source companion work [46] and subsequent Part II addendum [47] have analytically derived and illustrated the basic resulting characteristic features of thickness-friction self-standing and collapse states of the masonry arch, respectively for the classical, approximate Heyman-like uniform self-weight distribution along geometrical centre-line [46], and for the real Milankovitch-like uniform self-weight distribution accounting for the true locations of the centres of gravity of the ideal wedge-shaped infinitesimal chunks of the continuous arch, endowed with radial stereotomy [47].

Now, in terms of main substantial novelty of the present contribution, still for the latter, true Milankovitch-like uniform self-weight distribution, the analysis is herein completed, by deriving crucial general and specific aspects of the multi-faceted mechanical solution, displaying physical significance for the global understanding of masonry arch behaviour and for the interpretation in terms of practical architectural/engineering applications. Specifically, the following three principal innovation items are outlined:

- (a) The whole two- and three-dimensional state maps of the inherent characteristic solution variables, at given geometrical and friction governing parameters are analytically derived, and illustrated, to show the arising rich, multi-fold features of the mechanical solution.
- (b) The peculiar extremal conditions, on maximum intrinsic horizontal thrust and widest inner-joint angular positions are reconsidered, in view of the role of finite inherent friction, with respect to purely-rotational collapse states, and the corresponding arch geometries, and failure mechanisms, are numerically illustrated, by the independent support of an original Complementarity Problem/Mathematical Programming (CP/MP) formulation and computational implementation.
- (c) The mathematical vs. physical multiplicity of the inherent (symmetric) collapse mechanisms at the interfaces of the collapse domains is analytically investigated, to explore and quantify the amount of underlying linear dependence in the kinematical description.

Accordingly, presentation is herein structured in three main sections. Along line (a), Section 2 recalls the basic underlying mechanical equations and derives and describes the analytical maps of the various characteristic variables and associated collapse states. Toward item (b),

Section 3 highlights the role of finite friction in the extremal (maximum) conditions of intrinsic horizontal thrust and inner-joint angular positions, by also illustrating the associated arch morphologies and collapse states through a dedicated numerical CP/MP self-implementation. Concerning issue (c), Section 4 develops an analytical study on collapse mode multiplicity, in the presence of mechanisms possibly including sliding, as linked to finite inherent friction. Finally, closing Section 5 outlines resuming considerations on the analytical and numerical study, and physical interpretations, towards practical implications, with possible further research perspectives, in the realm of the Mechanics of masonry arches.

## 2 Underlying mechanical equations and analytical maps

### 2.1 Underlying mechanical equations

The present analytical treatment of the mechanical problem refers to framing, methodology and notation introduced in companion works [46, 47], and earlier source contributions [40–45], concerning both classical solution for purely-rotational collapse [40, 41, 44, 45], and insertion of finite friction toward describing possible joint-sliding activation, for mixed modes involving rotation and/or sliding [42, 43], considering both Heyman-like uniform self-weight distribution along geometrical centreline [3] and true Milankovitch-like uniform self-weight distribution accounting for the ideal wedge-shaped chunks of the continuous symmetric circular masonry arch with radial stereotomy [1]. Hereby, the minimum relevant information is reported, on behalf of the reader, for the necessary definitions and toward achieving self-containedness.

The underlying governing equations of the mechanical system may be expressed in terms of the following characteristics parameters and variables, peculiar of symmetric circular masonry arches (Fig. 1):

$$\mu = \tan \varphi, \quad \alpha; \quad \beta = \beta_{r,s}, \quad \eta = \frac{t}{r}, \quad h = \underbrace{\frac{H}{\gamma t d}}_w r = \frac{1}{\eta} \frac{H}{\gamma dr^2} = \frac{1}{\eta} \hat{h}, \quad \hat{h} = \frac{H}{\gamma dr^2} = \eta h \quad (1)$$

where:

- $\mu, \varphi$ : inherent Coulomb friction coefficient  $\mu = \tan \varphi$  and friction angle  $\varphi = \arctan \mu$ ;
- $\alpha$ : half-opening angle of the symmetric circular masonry arch;
- $r, t, d$ : radius, thickness and out-of-plane depth of the arch;
- $\gamma, w = \gamma t d$ : uniform specific weights per unit volume and per unit length of geometrical centreline of the arch;
- $H$ : horizontal thrust within the arch;

and:

- $\beta$ : angular inner-joint position from the crown ( $0 \leq \beta \leq \alpha$ ), either rotational,  $\beta = \beta_r$ , or/and sliding,  $\beta = \beta_s$ ;
- $\eta = t/r$ : thickness-to-radius ratio;
- $h = \hat{h}/\eta$ : classical non-dimensional horizontal thrust;
- $\hat{h} = \eta h$ : intrinsic non-dimensional horizontal thrust truly representing horizontal thrust  $H$  at given external physical arch characteristics ( $\gamma, d, r$ ).

Figure 1.

The (five) governing mechanical equations are expressed in two groups, of (three) rotational equations and (two) sliding equations, in terms of (five) underlying variables:  $\alpha, \mu$  and  $\eta, h$  (or  $\hat{h}$ ),  $\beta = \beta_r$  ( $\beta = \beta_s = \sqrt{h(1-h)}$  being implicitly represented through  $h$ ).

### 2.1.1 Rotational equations

The governing equations for rotational activation [46, 47] can be expressed as follows [40, 44, 45] (at undefined supercritical friction coefficient  $\mu$ ):

- Relative rotational equilibrium of upper or lower half-arch portion, with respect to inner intrados hinge at angular position  $\beta = \beta_r$  ( $h_1 = h_L$  “Lower thrust”, equilibrium from above;  $h_U$  “Upper thrust”, equilibrium from below, see [11, 44]):

$$h = h_1 = h_L(\beta, \eta) = \frac{(2 - \eta)\beta \sin \beta - 2(1 - \cos \beta) \text{fac}_M}{2 + \eta - (2 - \eta) \cos \beta} \quad (2)$$

or

$$h = h_U(\alpha, \beta, \eta) = \frac{(2 + \eta)\alpha \sin \alpha - (2 - \eta)\beta \sin \beta - 2(\cos \beta - \cos \alpha) \text{fac}_M}{(2 - \eta) \cos \beta - (2 + \eta) \cos \alpha} \quad (3)$$

- Absolute rotational equilibrium of whole half-arch, with respect to shoulder extrados hinge, involving half-opening angle  $\alpha$ , just through variable  $A(\alpha) = \alpha \cot(\alpha/2)$ :

$$h = h_2(\alpha, \eta) = A(\alpha) - \frac{2}{2 + \eta} \text{fac}_M, \quad A(\alpha) = \frac{\alpha \sin \alpha}{1 - \cos \alpha} = \alpha \cot \frac{\alpha}{2} \quad (4)$$

- Limit tangency condition of line of thrust (locus of pressure points) at haunch intrados in least-thickness condition (corrected from single term  $h_H$  of classical “approximate” Heyman solution [3] for  $\eta$  small):

$$h = h_e(\beta, \eta) = \underbrace{\beta \cot \beta}_{h_H} + 1 - \frac{2}{2 - \eta} \text{fac}_M = \underbrace{\beta \cot \beta}_{h_H} - \frac{\eta}{2 - \eta} \left( 1 + \frac{2}{\eta} (\text{fac}_M - 1) \right) \quad (5)$$

Thereby, Milankovitch-like real uniform self-weight distribution factor  $\text{fac}_M$ , accounting for the true location of the centres of gravity of each theoretical infinitesimal chunk of the continuous arch, at radial distance  $r_G = r(1 + \eta^2/12)$  (see Fig. 1), may be enabled ( $\delta_M = 1$ ), through on/off control flag  $\delta_M$  ( $\delta_M = 1/0$ ), with respect to Heyman-like uniform self-weight distribution along geometrical centreline ( $\delta_M = 0$ ):

$$\text{fac}_M = (1 + \delta_M \eta^2/12); \quad (\text{fac}_M - 1) = \delta_M \eta^2/12 \quad (6)$$

The explicit analytical representation of the purely-rotational solution, for both Heyman-like and Milankovitch-like uniform self-weight distributions, has been derived in [45], and respectively reported in companion works [46] and [47], in terms of classical rotational triplet  $\beta = \beta_r, \eta, h$ . Here, for the forthcoming purposes of the stationary analysis later delivered in Section 3, the further solution in terms of  $\hat{h} = \eta h$  is reported, and newly analyzed, for the Milankovitch-like self-weight distribution ( $\delta_M = 1$ ), again leading to the solution of a “cubic algebraic problem”, ruled by the following third-order polynomial equation in  $\hat{h}$ :

$$pol_{\hat{h}}^M = 2S^3 \hat{h}^3 - 3S(g - f)(f + g + 2S) \hat{h}^2 + 6(g - f)^2(f + 2S) \hat{h} - 8(g - f)^3 = 0 \quad (7)$$

where

$$\begin{aligned} f &= (\beta S)' = S + \beta C, & g &= fC + \beta S^2 = \beta + SC; \\ S &= \sin \beta, \quad C = \cos \beta; \quad \text{with link } \beta S^2 + Cf - g = 0 \end{aligned} \quad (8)$$

and symbol ' denotes first-order differentiation with respect to angular position  $\beta$ .

The arising two-branched purely-rotational solution in terms of  $\hat{h} = \eta h$  can explicitly be expressed as follows, similarly to what reported for triplet  $A(\beta), \eta(\beta), h(\beta)$  ( $\beta = \beta_r$ ) [45, 47] (same sign, either + or - in the two terms where  $\pm$  appears, i.e.  $+,+$  or  $-,-$ , or  $\mp$  appears, i.e.  $-,-$  or  $+,+$ , in the given order):

$$\begin{aligned}\hat{h}_M = \eta_M h_M &= \frac{g-f}{2S^2} \left( f + g + 2S - \right. \\ &\quad \left( \frac{1 \mp i\sqrt{3}}{2} \right) \frac{(f+g)^2 + 4S(g-S)}{\left( (f+g)^3 + 6gS(f+g) - 12fS^2 + 2S \text{SQRT} \right)^{1/3}} - \\ &\quad \left. \left( \frac{2}{1 \mp i\sqrt{3}} \right) \left( (f+g)^3 + 6gS(f+g) - 12fS^2 + 2S \text{SQRT} \right)^{1/3} \right)\end{aligned}\quad (9)$$

where  $i$  is the imaginary unit and

$$\text{SQRT} = \sqrt{9S^2(g-f)^2 - 2S(g-S)(9f^2 - g^2 - 16gS + 8S^2) - 3(f+g)^2(f^2 - 2gS + S^2)} \quad (10)$$

leading to a characteristic looping returning (to zero) trend on  $\beta = \beta_r$  (with peak point at horizontal tangent, and snap-back point at vertical tangent) and, linking to the similar explicit solution of  $A = \alpha \cot \alpha/2 = A(\beta)$ , to a bell-shaped trend on  $\alpha$  (with peak stationary point), as illustrated, for both, in the plots depicted in Fig. 2. The relevant extremal conditions on  $\hat{h}$ , occurring earlier at increasing  $\beta$  (and  $\alpha$ ), and on  $\beta$ , will newly be discussed in subsequent Section 3, in the context of finite friction.

Figure 2.

### 2.1.2 Sliding equations

The governing equations for sliding activation [46, 47] can be expressed as follows [42] (at undefined supercritical thickness-to-radius ratio  $\eta$ ):

- Sliding relation for activation of shoulder sliding joint:

$$\mu = \mu_{ss}(\alpha, h) = \frac{h \sin \alpha - \alpha \cos \alpha}{h \cos \alpha + \alpha \sin \alpha} \quad \text{or} \quad h = h_\mu(\alpha, \mu) = \alpha \frac{\cos \alpha + \mu \sin \alpha}{\sin \alpha - \mu \cos \alpha} \quad (11)$$

- Sliding relation for activation of inner sliding joint, at angular location  $\beta = \beta_s$ :

$$\mu = \mu_{is}(h) = \left. \frac{(1-h) \cos \beta - \beta \sin \beta}{(1-h) \sin \beta + \beta \cos \beta} \right|_{\beta = \beta_s(h)} = \sqrt{h(1-h)} \quad (12)$$

Purely-sliding collapse is set once both sliding Eqs. (11)-(12) hold, which may be represented by solution triplet  $\beta = \beta_s$ ,  $\mu$ ,  $h$  as a function of  $\alpha$ , as depicted in [46, 47]. Thus, once  $\alpha$  or  $\mu$  is set,  $\mu$  or  $\alpha$  is found, and  $h$  accordingly ( $\hat{h}$  through a coupling to a given  $\eta$ , supercritical to the least-thickness condition), with resulting inner-sliding angular position ruled by thrust  $h$  at  $\beta = \beta_s(h) = \sqrt{h(1-h)}$ .

## 2.2 Analytical maps

The main outcomes from the analytical analysis, based on the above governing mechanical equations are then presented and described, for the real Milankovitch-like uniform self-weight distribution ( $\delta_M = 1$ ), complementing and completing results delivered in earlier companion works [46, 47], which should be seen and appreciated all together, with the present contribution.

Results are first condensed in the two-dimensional plots reported in Figs. 3-8, which depict the analytical planar projection maps of all self-standing and collapse states, as a function of friction coefficient  $\mu$ , as described and discussed one by one, in what follows. Associated peculiar numerical data are also calculated, and provided in tables, with 16 significative digits, though the last one or last couple of ones may result uncertain, from the numerical find-root processes needed to express, to a very end, the obtained “exact” analytical representations, where the numerical solution of transcendental equations is required. Specifically, attached Tables 1-2 provide the characteristic data of the underlying landmark points that appear in the various analytical maps.

[Tables 1-2.](#)

[Figures 3-8.](#)

### 2.2.1 $\eta$ - $\mu$ filled plot

Figure 3 reports the two-dimensional  $\eta$ - $\mu$  filled plot with the **domains** of the recorded collapse states of the symmetric circular masonry arch, and with the concomitant indication of all the underlying analytical equations characterizing the various physical states arising within it. Like that, the planar map automatically shows how to evaluate the  $\eta$ - $\mu$  arch states from the governing analytical equations introduced in Section 2.1. So, each  $\eta$ - $\mu$  point of the plane regions can be calculated by the pertinent indicated equations.

In practice, four main regions (the latter with four sub-regions, for a total of seven regions and inherent collapse modes) are located:

- South-East region of classical Purely-Rotational modes (PR), ruled just by the three rotational equations (with either lower thrust  $h_1 = h_L$  or upper thrust  $h_U$ , and thrusts  $h_e$  and  $h_2$ ), at undefined friction coefficient  $\mu$  (meant as infinite, or finite supercritical one, right from the left border of either shoulder-sliding or inner-sliding activation). This region extends to  $\eta_l = 2(2\sqrt{3} - 3) \simeq 0.93$  as  $\mu \rightarrow \infty$ .
- North-West region of Purely-Sliding modes (PS), ruled just by the two sliding equations (with both  $\mu_{ss}$  and  $\mu_{is}$ , at undefined thickness-to-radius ratio  $\eta$  (meant as supercritical one, above of underneath border of both sliding-joint activations). This region is confined, on top, by physical limit  $\eta = 2$  ( $t = 2r$ ) and thus limited far right by marked Border point B at  $\eta = 2$ .
- Inner pond region among the above, of mixed Sliding-Rotational modes (SR), with shoulder sliding and inner joint rotation, ruled by two rotational equations (with only lower thrust  $h_1 = h_L$ , and thrust  $h_e$ ) and just by shoulder sliding activation (thus, just by  $\mu_{ss}$ ). This region is limited from below-right ( $ss$  branch) and above-left ( $is$  branch) by the two previous regions, and extends up to marked Triple point T, which constitutes a peculiar

watershed, landmark point of the maps of the arch states. This is a pole of direct communication and intertwining of all the described regions, and four main underlying collapse states (with physical and mathematical multiplicity later analyzed in Section 4).

- North-East basin region of mixed Rotational-Sliding modes (RS), with inner sliding and shoulder rotation, ruled by two rotational equations (with only upper thrust  $h_U$ , and thrust  $h_e$ ) and just by inner-sliding activation (thus, just by  $\mu_{is}$ ). Also this region is limited from below-right and above-left by the first two regions of purely-rotational/sliding modes, from above by physical limit  $\eta = 2$  ( $t = 2r$ ), right from Border point B and extends to  $\mu \rightarrow \infty$ , where an immaterial far-East boundary shall be conceived, for thickness-to-radius ratios between  $2(2\sqrt{3} - 3) \leq \eta \leq 2$ .

This latter region of mixed rotational-sliding modes, in turn, may continuously be subdivided into four collapse regions (three regions and the above far-East boundary at  $\mu \rightarrow \infty$ ), namely:

- One sub-region with  $\beta_r > \beta_s$ , which constitutes the main part of mixed rotational-sliding modes below asymptotic limit  $\eta_l \simeq 0.93$ .
- One thin sub-region slice with  $\beta_r < \beta_s$ , hinged among scored Shift point S and Junction point J, extending to the limit with  $\beta_r = 0$  marking the appearance of overturning modes.
- A wider sub-region above such  $\beta_r = 0$  limit of overturning modes, with Overturning-Sliding modes (OS) ruled just by  $h_U$  at  $\beta_r = 0$  and with inner-sliding activation at finite friction and non-zero non-dimensional horizontal thrust  $h$ .
- The above-mentioned far-East boundary segment of Purely-Overturning (PO) modes with  $\beta_r = 0$  and  $h = 0$  at  $\mu \rightarrow \infty$ , for  $2(2\sqrt{3} - 3) \leq \eta \leq 2$ .

### 2.2.2 $\eta$ - $\mu$ plot

Figure 4 further delivers the two-dimensional  $\eta$ - $\mu$  plot with the analytical map of the **boundaries** between the regions of the various collapse states, again with the simultaneous indication of the sets of equations that analytically describe them.

Physically, two main divides are apparent, intertwining at peculiar watershed Triple point T, separating the earlier-described four main macro-regions of collapse modes:

- The first lower then upper line specifically marked by shoulder-sliding activation,  $\mu = \mu_{ss}$ , going from the origin to Triple point T (segment marked just by  $\mu = \mu_{ss}$ , separating the region of purely-rotational modes, below and left from Triple point T), then constituting the main continental divide separating modes with rotation and purely-sliding mechanisms, along directrix TSJB, up to Border point B.
- The first upper then lower line specifically marked by inner-sliding activation,  $\mu = \mu_{is}$ , going from the origin and re-joining at Triple point T, then going towards infinity ( $\mu \rightarrow \infty$ ), as  $\eta \rightarrow 2(2\sqrt{3} - 3)$ , along the separating boundary of purely-rotational modes marked just by inner-sliding activation,  $\mu = \mu_{is}$  (above and right from Triple point T).

Further, two internal divides of the above fourth macro-region of mixed rotational-sliding modes arise, both again going to infinity ( $\mu \rightarrow \infty$ ) as  $\eta \rightarrow 2(2\sqrt{3} - 3)$ :

- Hinged at Shift point S, line  $\beta_r = \beta_s$ , marking the states with inner joint that plays as either rotational and/or sliding.
- Hinged at Junction point J, line  $\beta_r = 0$ , starting to mark the overturning states with no inner-hinge rotation, displaying inner sliding at finite  $\mu$ , with non-zero non-dimensional horizontal thrust  $h$ , and with no inner sliding (purely-overturning modes) at infinite  $\mu$ , with zero non-dimensional horizontal thrust  $h$ .

Moreover, two extreme boundaries should not be forgotten:

- Upper physical boundary  $\eta = 2$  ( $t = 2r$ ), right from Border point B, marking specific states with overturning-sliding at variable finite friction  $\mu$ , with  $\beta_r = 0$  and non-zero  $h$ , and left from Border point B, marking specific states with purely-sliding at variable finite friction  $\mu$ , with  $\beta_s = \sqrt{h(1-h)}$  and non-zero  $h$ .
- Far-East boundary segment at infinite friction,  $\mu \rightarrow \infty$ , for  $2(2\sqrt{3} - 3) \leq \eta \leq 2$ , marking purely-overturning states with  $\beta_r = 0$  and  $h = 0$ .

The various characteristic traits of the analytical maps are distinguished with ten colours (same for the following maps for the other characteristic solution variables), namely:

- the lower *ss* branch from the origin to T (black);
- the upper *is* branch from the origin to T (purple);
- the lower (*is*) branch from T to infinity (blue), prosecution of the above;
- the upper main divide from T to S (green);
- the upper main divide from S to J (darker green);
- the upper main divide from J to B (cyan);
- the above-described  $\beta_r = \beta_s$  locus from S to infinity (magenta);
- the above-described  $\beta_r = 0$  separation from J to infinity (darker magenta);
- the upper physical boundary at  $\eta = 2$  ( $t = 2r$ ), right from B to infinity (red);
- the upper physical boundary at  $\eta = 2$  ( $t = 2r$ ), left from B to zero (darker red).

### 2.2.3 $h$ - $\mu$ plot

Figure 5 depicts the regular map of non-dimensional horizontal thrust  $h = H/(\gamma t d r)$  as a function of friction coefficient  $\mu$ , with colour segments as above described. It shows:

- Basically, a monotonic decreasing trend of  $h$  at increasing friction coefficient  $\mu$  (and associated increase of half-opening angle  $\alpha$ , as reported below).
- This clearly shows that, at finite friction, the amount of friction coefficient at one sliding activation sets the value of non-dimensional horizontal thrust  $h$  within the masonry arch.
- The trend is first two-branched, up to Triple point T, among the lines involving only shoulder-sliding activation (*ss* branch), and the curve linked to inner-sliding activation (*is* branch); then, single-branched, still along relation  $h(\mu)$  for inner-sliding activation (see

Figure 4a in [46]), attached to  $\mu = \mu_{is}(h)$ , Eq. (12), which prosecutes and re-joins all segments endowed with  $\mu = \mu_{is}(h)$ , along directrix TSJB, and beyond, among overturning states with inner sliding, at increasing finite  $\mu$ , asymptotically going to  $h = 0$  as  $\mu \rightarrow \infty$ , for purely-overturning states.

- Thus, thereby, the region of mixed rotational-sliding modes is smashed down, along a single  $h(\mu)$  line after Triple point T, whereas, on the right and above of that, and of the preceding shoulder-sliding branch, purely-rotational states are recovered, at undefined friction coefficient  $\mu$ , while the inner pond of mixed sliding-rotational modes is contained among the two *ss* and *is* branches re-joining at Triple point T. Thus, two of the four macro-regions of the previous  $\eta$ - $\mu$  filled plot may herein be filled, for representation, but this is not done, for consistency with the forthcoming two-dimensional projection maps, where fillings will hardly or only partly be representable and decipherable, within them.
- Since all sliding states with inner sliding are re-joined along below line  $\mu = \mu_{is}(h)$ , thus including for purely-sliding states involving both shoulder- and inner-sliding activation, the latter states are again all represented by such a line, while the region of the plane below that represents  $h$ - $\mu$  instances that cannot be reached, as unfeasible arch states of the mechanical solution, at variable friction.

#### 2.2.4 $\hat{h}$ - $\mu$ plot

Figure 6 outlines the map of intrinsic non-dimensional horizontal thrust  $\hat{h} = H/(\gamma dr^2) = \eta h$  (truly representing intrinsic horizontal thrust  $H$  at given physical arch characteristics:  $\gamma; d, r$ ) as a function of friction coefficient  $\mu$ . It illustrates:

- Richer features, for the intrinsic horizontal thrust that the arch is truly able to transfer, at given physical arch features ( $\gamma; d, r$ ), with peculiar non-monotonic trends, extending those of the classical purely-rotational solution, somehow reproducing the, though-monotonic, trends apparent in the  $\eta$ - $\mu$  plane, again with a clear effect of finite friction coefficient  $\mu$  in ruling the horizontal thrust within the masonry arch, at a sliding activation.
- Again, on low levels of friction, up to Triple point T, two bell-shaped *ss* and *is* branches are distinguished, among which mixed sliding-rotational states are lying, with a fork of stationary points, at constant  $\hat{h}$ , extending the range of maximum  $\hat{h}$  for the purely-rotational modes at undefined friction coefficient  $\mu$ . Such stationary points are further analyzed and discussed in subsequent Section 3.
- After Triple point T, at increasing  $\mu$ , the trends earlier experienced for  $\eta$  somehow come back to appear, within  $\hat{h} = \eta h$ , with the various coloured branches that separate the sub-regions of the mixed rotational-sliding modes.
- Thereby, main divide TSJB rapidly steepens up (almost vertically) toward Border point B, which reaches a rather peculiar extremal peak condition, with kink, on the following physical limit branch with  $\eta = 2$ , thus with  $\hat{h} = 2h$ , and  $h$  seen from the previous  $h$ - $\mu$  plot (right from Border point B, red line), narrowing down, with the other common asymptotic trends with  $\hat{h}$  anyhow going to zero (as  $h$  is also doing), as  $\mu \rightarrow \infty$ .

- The extremal peak at Border point B reveals higher, than the local maxima at the stationary condition, at variable  $\mu$ , and shows a “snow quote”, like for mountain chains on different planes, of not much different friction and arch states leading to slightly higher horizontal thrust transfer (anyway for peculiar, unusual arches with  $\eta$  near 2, rather opened and with almost no intrados circle and underneath fornix to allow for underneath passage).
- Hereby, the area(s) that could be filled are those of the mixed rotational-sliding modes, lying among the coloured depicted trends asymptotically going down to  $\hat{h} = 0$  at  $\mu \rightarrow \infty$ . However, since purely-rotational states right from black *ss* branch up to Triple point T, and blue one after it, and mixed sliding-rotational states among *ss* and *is* branches are not easy to be shaded, fillings are neither reported within the figure.
- Similarly, purely-sliding states, at given  $h = h(\mu_{is})$  from  $\mu_{is}(h)$ , Eq. (12), set and bounded by friction at inner-sliding activation (see previous  $h$ - $\mu$  plot) and undefined supercritical  $\eta$  (see previous  $\eta$ - $\mu$  plots) can neither easily be represented, anyway for arches, at those values of  $\mu$  and relevant states that always lead to incipient collapse at any supercritical  $\eta$ , in the spirit of “Couplet-Heyman problem” least-thickness determination. Also, values of thrust  $\hat{h}$  higher than  $2h$ ,  $h = h(\mu_{is})$  from Eq. (12) at inner-sliding activation, cannot a priori be transferred, within the masonry arch, since  $\eta \leq 2$  (see further visible darker red raising line left from Border point B).

### 2.2.5 $\beta$ - $\mu$ plot

Figure 7 illustrates the map of inner-joint angular positions from the crown, mainly  $\beta_r$  for inner-rotational joints, and also  $\beta_s$  (lower curve) for inner-sliding joints, at variable friction coefficient  $\mu$ . It represents:

- As per the underlying purely-rotational component,  $\beta_r$  trends turn-out bell-shaped, going through (a locus of) stationary points of widest inner-hinge angular position, that can be displaced, a bit, by friction coefficient  $\mu$  (see analysis and discussion in subsequent Section 3).
- At the same time, the  $\beta_s$  trend for inner-sliding activation, implicitly described, by itself, by relation  $\mu = \mu_{is}(h)$ , Eq. (12), also is non-monotonic, with local maximum intrinsically recorded at  $\beta_s = \sqrt{h(1-h)} = 0.5 \simeq 28.65^\circ$ , for  $h = 0.5$  [42] (at a resulting specific value of  $\mu$ ,  $\mu = (\cos 0.5 - \sin 0.5)/(\cos 0.5 + \sin 0.5) = 0.2934079930260234$ ,  $\varphi \simeq 16.35^\circ$ , and of  $\alpha$ , at concomitant shoulder-sliding activation, with  $\alpha = 1.542786942738411 \simeq 88.40^\circ$ , thus for an almost complete semi-circular arch,  $\alpha \simeq 90^\circ$ , with wider inner-sliding joint angular position  $\beta_s \simeq 30^\circ$  at about 1/3 of half-opening, and incidentally inner-rotational joint angular position  $\beta_r \simeq 60^\circ$  at about 2/3 of half-opening).
- Again, *ss* and *is* two-branched trends “containing” inner pond mixed sliding-rotational modes, with variable inner  $\beta_r$ , at changing  $\mu$ , depart from the origin and re-join at Triple point T.
- After that, branches with  $\mu = \mu_{is}$  only (blue), and with  $\mu = \mu_{ss}$  (green and darker green), bifurcate, both going down to zero, the former slowly, with asymptotic trend, as  $\mu \rightarrow \infty$ , the latter sharply, almost precipitating down to Junction point J at  $\beta_r = 0$ .

- After Junction point J,  $\beta_r$  keeps set to zero, until Border point B (cyan), and beyond, at physical limit  $\eta = 2$  (red), and along superimposed (invisible) darker-magenta line at  $\beta_r = 0$ .
- Notice that, by the adopted superposition representation of curves for  $\beta_r$  and  $\beta_s$ , they truly turn out to cross at Shift point S, where condition  $\beta_r = \beta_s$  is first met, and then followed along the magenta line superimposed to function  $\mu_{is}(h)$  describing inner-sliding activation (see Figure 4b in [46]), at increasing  $\mu$  right from S. This line separates mixed rotational-sliding states with  $\beta_r > \beta_s$  and with  $\beta_r < \beta_s$ , as per the  $\eta$ - $\mu$  plot, which are the only  $\beta_r$  states that could easily be shaded as in the  $\eta$ - $\mu$  plot.
- Besides, local maxima also result absolute maxima, for  $\beta_r$  and  $\beta_s$ . Thus, inner-joint angular positions that would be wider than those recorded ones are physically unreachable for the masonry arch.

### 2.2.6 $\alpha$ - $\mu$ plot

Figure 8 finally draws down the locus of masonry arch states in the underlying plane of inherent physical variables, namely half-opening angle  $\alpha$  (only variable that was present for the classical purely-rotational collapse analysis, at undefined  $\mu$ ), and friction coefficient  $\mu$  (variable that is present for the purely-sliding collapse analysis, at undefined  $\eta$ ). It reveals:

- Basically, an overall monotonic increasing/decreasing trend of  $\alpha$  on  $\mu$ , as for a cursor on given arch states within the governing  $\alpha$ - $\mu$  plane.
- The forks among trends, with specific asymptotic specificities as  $\mu \rightarrow \infty$ , are rather narrow, again really reducing to zero at watershed landmark Triple point T. Asymptotic trends toward purely-overturning modes at unbounded friction  $\mu \rightarrow \infty$  are obtained for curves departing from T, S and J, going to  $\alpha_l = 2.590843443008955 \simeq 148.44^\circ$  ( $A_l = \sqrt{3} - 1$ ) at  $\eta_l = 2(2\sqrt{3} - 3) \simeq 0.93$ , and for, rather flat, (red) limit curve from Border point B, at  $\eta = 2$ , with  $\alpha \rightarrow \alpha_L = 2.648388899151005 \simeq 151.74^\circ$  ( $A_L = 2/3$ ), which sets the overall Limit of feasible  $\alpha$  values for the arch.
- Stationary paths, for both static  $\hat{h}$  and kinematical  $\beta_r$  variables, are dashed, first, on the right, for purely-rotational modes, at supercritical, undefined  $\mu$  and constant  $\alpha$ , then, between two-branched ss and is curves, for mixed sliding-rotational modes, with some opening, of the fork of stationary values, at variable  $\mu$  (and slightly-decreasing  $\alpha$ ). These loci can much be appreciated in the zoom further depicted in Fig. 18, as described in subsequent Section 3.
- While arch states right/below the lower envelope of the  $\alpha$ - $\mu$  plot represent purely-rotational modes at undefined friction, arch states beyond the upper envelope of the  $\alpha$ - $\mu$  diagram result physically unfeasible. Thus, a masonry arch with given half-opening angle  $\alpha$  needs a friction coefficient  $\mu$  larger than a certain amount (read from the upper  $\alpha$ - $\mu$  envelope), to be potentially built (since then the whole also depends on the available inherent thickness-to-radius ratio  $\eta$ ). Moreover, at increasing  $\alpha$ , a further robust friction is needed, for the physical arch state, to keep really feasible.

### 2.2.7 Three-dimensional plots

Eventually, to better appreciate, qualitatively, the intricacy of the feasible and collapse masonry arch states, complete analytical three-dimensional representations in each characteristic mechanical variable  $\eta$ ,  $h$ ,  $\hat{h}$ ,  $\beta_{r,s}$ , as linked to inherent physical parameter state  $\mu\text{-}\alpha$ , can be traced, by surface plots, as reported in Figs. 9-12, showing the surfaces of incipient collapse states (and folding lines within them) that characterize the failure conditions of the masonry arch. The earlier depicted much quantitatively readable two-dimensional maps then become projection manifestations of such more qualitative, though truly illustrative, three-dimensional representations. A brief description, of the three-dimensional representations follows below.

[Figures 9-12.](#)

The 3D representation in Fig. 9 depicts the surface of the collapse states of the masonry arch in the space of mechanical variables  $\eta$  and  $\mu\text{-}\alpha$ . Namely, it inflates both the  $\alpha$  dimension, over the 2D projection  $\eta\text{-}\mu$  plots in Figs. 3-4, and the  $\eta$  dimension, over the 2D projection  $\alpha\text{-}\mu$  map in Fig. 8. Similarly, the folding 3D lines, at the sub-surface intersections, extrude the 2D lines that are visible in the projection maps, in the  $\alpha$  direction, for the  $\eta\text{-}\mu$  plot, and in the  $\eta$  direction, for the  $\alpha\text{-}\mu$  plot.

The four stated main collapse modes, namely purely-rotational, mixed sliding-rotational, mixed rotational-sliding (this with continuously occurring variants linked to the positioning of  $\beta_r \geq 0$ , with respect to  $\beta_s$ , and with further underlying purely-overturning limits as  $\mu \rightarrow \infty$ ) and purely-sliding are represented by the main coloured folds of the collapse surface. The cylindricities on  $\mu$ , for purely-rotational modes, and on  $\eta$ , for purely-sliding modes, are clearly visible. The growing trend of  $\alpha$ , on  $\mu$  and  $\eta$ , can be appreciated, with asymptotic saturation tendencies as  $\mu \rightarrow \infty$ , towards the  $\alpha_l$  and  $\alpha_L$  limits for purely-overturning modes at infinite friction and zero thrust. Globally, the growing trend is shown, monotonically, on all three variables  $\eta$ ;  $\mu$ ,  $\alpha$ , showing the linking state, of increasing  $\eta$ , at widening  $\mu\text{-}\alpha$  physical state.

This 3D representation, although much qualitative, than more quantitative, readable 2D representations, actually represents a “summa”, on the whole analytical investigation on the least-thickness determination, in the presence of finite friction, representing the envelope of the various collapse states.

Similarly, further Figs. 10-12 complement the above “summa”, by extruding the  $\alpha$  dimension, over the  $h\text{-}\mu$ ,  $\hat{h}\text{-}\mu$ ,  $\beta_{r,s}\text{-}\mu$  projection plots, or the competent  $h$ ,  $\hat{h}$ ,  $\beta_{r,s}$  dimension, over the underlying  $\alpha\text{-}\mu$  physical state projection plot, whereby still monotonic trends are recorded for  $h$  in Fig. 10, while generally folding trends are depicted for  $\hat{h}$  and  $\beta_{r,s}$  in Figs. 11-12, displaying stationary points and loci, for peculiar system states. They help to explain and visualize the quantitative information of the underlying 2D representations, which generally annihilate the folding superpositions in space, and thus do not easily allow for the representation of the corresponding fillings, within the projection planes (unless for the source  $\eta\text{-}\mu$  2D filled plot reported in Fig. 3).

Then, such final iconic 3D representations complement, and complete, the earlier 2D projection plots, in showing the intricacies, and characteristic features, of such an ethereal, on paper, mechanical system, which is truly enriched, in physical manifestations, in adding the dimension parameter of variable friction, within the classical least-thickness “Couplet-Heyman optimisation problem”, by coming then to possibly release the hypothesis of no sliding failure.

## 2.3 Illustration of sample “safe” vs. “collapse” arch states

The current section is now further framed, in view of additionally illustrating the meaning, and possible practical value, of the present mechanical analysis, and derived analytical solution, in terms of shifting from a reference “safe” state, to a “collapse” state, of the masonry arch, and identifying the type of such a collapse state, as revealed in Section 2.2, by varying the three main underlying parameters of the symmetric circular masonry arch, i.e. thickness-to-radius ratio  $\eta$ , friction coefficient  $\mu$  (friction angle  $\varphi$ ) and half-opening angle  $\alpha$ . This shall be useful to identify the collapse state that may be expected, in order to prevent it, with potential meaning that may later be extrapolated to other arch morphologies and configurations.

To moreover illustrate the significance and use of the two-dimensional  $(\eta, \mu)$  arch state map (at implicitly variable  $\alpha$ ) in Fig. 3, and of the three-dimensional  $(\eta; \mu, \alpha)$  representation of limit collapse (surface envelope) and safe self-standing arch states (inner volume) in Fig. 9, a couple of meaningful specific instances are selected, to display how, from a specific  $(\eta; \mu, \alpha)$  safe state of the arch, within the volume inside the collapse surface, a limit collapse state of the arch, on the wrapping surface, may be reached, for instance by straight paths at one variable and two constant arch characteristics, among  $\eta$ ,  $\mu$  and  $\alpha$ .

### 2.3.1 Representation by a numerical CP/MP formulation

Before doing that, toward achieving in the sequel a complete representation of the various masonry arch states and collapse modes, a dedicated original “ $\varphi$ - $\lambda$  numerical Complementarity Problem/Mathematical Programming (CP/MP) formulation” and home-made implementation (within MatLab) can be adopted, as in companion works [46, 47], to illustrate and validate the outcomes of the analytical solution for the various arch states, herein again for the true Milankovitch-like uniform self-weight distribution (Fig. 1), which can conveniently be flagged on, within the numerical procedure, as analytically detailed in Section 2.1.

The numerical CP/MP formulation has extensively been introduced in [43], and later updated in [44], references to which the interested reader may be referred to, for the various technical details. As a main general concept, and as typically outlined in the Theory of Plasticity, of Solids and Structures, and in Limit Analysis, masonry arch states can be handled by setting a Complementarity Problem, among strength conditions within static internal variables  $\varphi$  and collapse kinematic variables at rotating/sliding joints  $\dot{\lambda}$ . This may further be brought down to a Mathematical Programming (minimization) problem, under linear constraints, herein with apparent arch collapse onset that may numerically come out in the order of  $10^{-16}$ , for targeted objective function  $-\varphi^T \dot{\lambda}$ , in the quest of a true numerical zero for the sought minimum extremal condition:

$$\text{CP: } \varphi \leq \mathbf{0}, \quad \dot{\lambda} \geq \mathbf{0}, \quad \varphi^T \dot{\lambda} = 0 \quad (13)$$

$\Downarrow$

$$\text{MP: } \min \left\{ -\varphi^T \dot{\lambda} \mid \text{lin. constr.} \right\} = 0 \quad (14)$$

Such a “ $\varphi$ - $\lambda$  formulation” turns out particularly feasible, in the present setting of tracing masonry arch mechanisms, to locate and depict the collapse modes that are reached in the least-thickness condition, at given geometrical morphology and variable inherent friction among the theoretical blocks of the arch, coming from the characteristic features that are “exactly” calculated by the analytical solution, as described in Sections 2.1-2.2.

The numerical CP/MP procedure allows to represent, all together, the following peculiar masonry arch features, for the various sample arch cases that may be selected, toward verification and illustration purposes:

- geometrical properties of the masonry arch in the reference configuration (black);
- all-internal “*line of thrust*” (red) and “*line of friction*” (blue);
- (symmetrically-set) associated collapse mode, possibly including rotation/sliding (green).

Herein, notice that the “*line of thrust*” is classically taken as the locus of pressure points, of non-dimensional eccentricity  $\hat{e} = [M/N]/[t/2] = e/[t/2]$ , i.e. moment over axial compression force ratio within the arch, normalized to be  $\pm 1$  at a rotational joint activation [40], and the “*line of friction*” is originally meant as the locus of shear over normal force ratio, normalized as  $\hat{e}_s = [T/N]/\mu = e_s/[t/2]$  to be  $\pm 1$  at a sliding joint activation [43]. Then, when such lines come to touch the intrados or extrados of the masonry arch, failure joints are thereby activated, within the arch, to possibly deliver a collapse mechanism as coherently described by compatible kinematic variables  $\dot{\lambda}$  complementary to underlying conformal static variables  $\varphi$ , as per Eq. (13).

### 2.3.2 Selected instances

Now, referring to the upgraded analytical 2D map in Fig. 13 and 3D carpet plot in Fig. 14, the following two sample reference arch instances with rounded values of couple  $(\eta, \mu)$  are herein considered, for practical illustration purposes:

- $(\eta = 0.5, \mu = 1.0 [\varphi = 45^\circ])$ , leading to reach, as a mixed mode, a Sliding-Rotational mode, for  $\alpha$  near  $130^\circ$ , in the inner pond region below Triple point T (see resulting arch illustrations in Fig. 15 and characteristic data in Table 3);
- $(\eta = 0.8, \mu = 1.8 [\varphi \simeq 61^\circ])$ , leading to reach, as a mixed mode, a Rotational-Sliding mode, for  $\alpha$  near  $145^\circ$ , in the upper basin region above Triple point T (see resulting arch illustrations in Fig. 16 and characteristic data in Table 4).

More in details, Fig. 13 represents the two-dimensional view in the  $(\eta, \mu)$  plane of Fig. 3, with the considered instances, and scoring of the three points that show the three collapse modes that can be reached, for each of the two assumed reference  $(\eta, \mu)$  states. Specifically:

- For the given  $(\eta, \mu)$  state, either a mixed SR or RS collapse state is located, for peculiar values of half-opening angle  $\alpha$ , to be associated to such states.
- Instead, at given  $(\eta, \mu)$  state, a lower  $\alpha$  value, for instance for a sample (overcomplete) reference value of  $\alpha = 100^\circ$ , leads to a safe state of the masonry arch; namely, for that  $\alpha$  value, the selected  $(\eta, \mu)$  state is supercritical, and no collapse occurs, as Eq. (14) at zero value cannot be reached.

- Then, decreasing from that, in either  $\eta$  or  $\mu$ , for such sample reference value of  $\alpha = 100^\circ$ , a loosening self-standing capacity of the arch is obtained:
  - + the instances of Purely-Rotational collapse are reached by reducing  $\eta$ , at constant given  $\mu$ , leading to the critical least-thickness condition for Purely-Rotational collapse states (independently of supercritical  $\mu$ );
  - + the instances of Purely-Sliding collapse are reached by reducing  $\mu$ , at constant given  $\eta$ , leading to the critical friction condition for Purely-Sliding states (independently of supercritical  $\eta$ ).
- Three-lateral iso- $\alpha$  lines (with straight horizontal trait at constant  $\eta$  at any supercritical value of  $\mu$ , straight vertical trait at constant  $\mu$  at any supercritical value of  $\eta$ , and inner curvilinear trait at specifically variable  $\eta$  and  $\mu$ , within the inner pond region of mixed SR modes or the upper basin region of mixed RS modes, below or above Triple point T, among *is* and *ss* separating dorsals), for the reference value of  $\alpha = 100^\circ$ , and for the obtained critical values of  $\alpha \simeq 130^\circ$  and  $\alpha \simeq 145^\circ$ , are also depicted, to inspect the implicit role of  $\alpha$ , in the 2D  $(\eta, \mu)$  projection map.

This is further appreciated in the three-dimensional view reported in Fig. 14, which retakes the 3D  $(\eta; \mu, \alpha)$  carpet plot in Fig. 9 and newly highlights:

- the safe states of the arch for the two selected  $(\eta, \mu)$  values and the reference considered value of  $\alpha = 100^\circ$ , leading to two safe reference points positioned within the self-standing volume surrounded by the wrapping surface of the collapse states (wider blue and green embedded spherical dots);
- paths at constant  $(\alpha, \mu)$ , lowering  $\eta$ , until reaching the critical  $\eta$  for PR modes;
- paths at constant  $(\alpha, \eta)$ , lowering  $\mu$ , until reaching the critical  $\mu$  for PS modes;
- paths at constant  $(\eta, \mu)$ , raising  $\alpha$ , until reaching the critical  $\alpha$  for mixed SR vs. RS modes, depending on the set reference state value of  $(\eta, \mu)$ , below or above Triple point T.

Furthermore, thanks to the introduced CP/MP numerical formulation, the resulting arch states and collapse modes are illustrated in Figs. 15-16, where in each  $2 \times 2$  array figure the four shots show:

- (a) SAFE state, for the reference value of  $\alpha = 100^\circ$  and the given  $(\eta, \mu)$  state (herein, a possible configuration of line of pressure and of line of friction is drawn, for the continuous arch, safely included within it, minimizing objective function  $-\varphi^T \dot{\lambda}$ , though to a non-zero positive value, i.e. by excluding collapse);
- (b) mixed SR vs. RS collapse state, for that given  $(\eta, \mu)$  state, at the resulting critical  $\alpha$  value, around  $\alpha \simeq 130^\circ$  vs.  $\alpha \simeq 145^\circ$ ;
- (c) PS collapse state, for that given value of  $\eta$  and reference opening  $\alpha, \mu$  becoming critical at that  $\alpha$ , independently of supercritical  $\eta$ ;
- (d) PR collapse state, for that given value of  $\mu$  and reference opening  $\alpha, \eta$  becoming critical at that  $\alpha$ , independently of supercritical  $\mu$ .

In further comparing, mutually, the appearances in the instances depicted in the  $2 \times 2$  frames in Figs. 15-16, each by each, (a) to (d), notice that:

- (a) for the two selected reference states of  $(\eta, \mu)$ , namely  $(\eta = 0.5, \mu = 1.0)$  in Fig. 15(a) and  $(\eta = 0.8, \mu = 1.8)$  in Fig. 16(a), which are SAFE at  $\alpha = 100^\circ$ , the arch is thicker, and with higher friction (much in Fig. 16(a)), then what would be required for collapse, for  $\alpha = 100^\circ$ ;
- (b) for the mixed modes at the two given states of  $(\eta, \mu)$ , mixed SR vs. RS collapse modes are recorded in Fig. 15(b) vs. Fig. 16(b), respectively for  $\alpha \simeq 130^\circ$  and  $\alpha \simeq 145^\circ$ , thus with higher values, in Fig. 16(b), for all three  $(\eta; \mu, \alpha)$  arch governing parameters, showing the hierarchy between SR and RS collapse modes;
- (c) for the PS modes in Figs. 15(c) and 16(c), at same  $\mu = 0.42127$  and  $\alpha = 100^\circ$ , there is no apparent diversity in the collapse manifestation, if not for the different value of  $\eta$ ,  $\eta = 0.5$  in Fig. 15(c) vs.  $\eta = 0.8$  in Fig. 16(c), showing that, despite the increasing thickness, the arch is anyway at PS collapse, at that  $(\mu, \alpha)$  state, for any supercritical value of  $\eta$ .
- (d) for the PR modes in Figs. 15(d) and 16(d), at same  $\eta = 0.16074$  and  $\alpha = 100^\circ$ , there is no apparent diversity in the collapse manifestation, if not for the (internal invisible) different value of  $\mu$ ,  $\mu = 1.0$  in Fig. 15(d) vs.  $\mu = 1.8$  in Fig. 16(d), showing that, despite the increasing inherent friction, the arch is anyway at PR collapse, at that  $(\eta, \alpha)$  state, for any supercritical value of  $\mu$ . Shots are practically the same, if not for a little variation in the reported line of friction, due to the different values of  $\mu$ , lower in Fig. 15(d), thus therein with slightly higher friction eccentricity  $e_s = [T/N]/\mu \cdot [t/2]$ , with respect to Fig. 16(d), which can much be appreciated toward the shoulders.

Recall that all characteristic data, for the selected instances, are gathered in Tables 3-4, as obtained, “exactly”, from the field equations directly annotated within the  $(\eta, \mu)$  filled plot in Fig. 3 (practically, data are therein reported with just up to 5 significative digits).

Figure 13 and Figure 14.

Table 3 and Figure 15.

Table 4 and Figure 16.

Finally, to complete the picture, Fig. 17 further displays the SR modes that can be observed, for the chosen reference value of half-opening angle  $\alpha = 100^\circ$ , respectively at the lower shoulder sliding (*ss*) interface with the concomitant PR mode (already visible, as a mechanism, in either Figs. 15(d) or 16(d)), and the upper inner sliding (*is*) interface with the concomitant PS mode (already visible, as a mechanism, though for higher  $\eta$ , in either Figs. 15(c) or 16(c)), bounding the inner pond region of mixed SR modes below Triple point T (Fig. 13):

- Among such boundary states, different SR modes may be displayed, for  $\alpha = 100^\circ$ , within the inner pond region, along the non-linear segment of the three-lateral iso- $\alpha$  line already mentioned in the discussion of Fig. 13, showing that, at constant half-opening angle  $\alpha$ , the transition from PR to PS collapse modes, through mixed SR modes, requires, at a

reducing friction coefficient  $\mu$ , an increase of thickness-to-radius ratio  $\eta$  (meanwhile inner-hinge angular position from the crown  $\beta_r$  is also increasing);

- Like that, one sees also how the chosen reference safe arch states for  $\alpha = 100^\circ$  in Figs. 15(a) and 16(a) may also directly degenerate to mixed SR modes, at that  $\alpha$  value, at decreasing both  $\eta$  and  $\mu$ , to peculiar values, thus showing all collapse modes that can be experienced for that  $\alpha$  value, i.e. PR, SR and PS;
- Obviously, as a closing practical remark, referring to the arch state in the low part of Fig. 17, on the lower *ss* boundary, for  $\alpha = 100^\circ$ , it is meant that arches with  $\alpha = 100^\circ$ , and supercritical  $\eta > 0.16074$ ,  $\mu > 0.51170$  ( $\varphi > 27.10^\circ$ ) are anyway safe, corresponding to points that are nevertheless represented within a North-West planar quadrant centred on that *ss* point in the  $(\eta, \mu)$  2D map in Fig. 13 and lying within the volume wrapped by the collapse surface depicted in Fig. 14, on a section plane at constant  $\alpha = 100^\circ$ .

Figure 17.

Then, the achieved mechanical representation is a full analytical one, while selected instances can numerically be evaluated, in the end, by the necessary numerical solutions of the underlying transcendental equations. Like that, it may further be operated, for the various  $(\eta; \mu, \alpha)$  arch states, including also in the RS region that moreover specializes in sub-regions (Section 2.2) and also leading to collapse modes with Overturning components ( $\beta_r = 0$ ) at raising friction.

### 2.3.3 Resuming considerations

The analysis reported in present Section 2.3, based on analytical achievements, and autonomous numerical validations, shall further clear the mechanical role of the achieved results, in terms of separating safe states from collapse instances of (symmetric circular continuous) masonry arches, at variable inherent friction.

Eventually, the topic of the present methodological research may assist Mechanics experts who are also interested in the practical analysis of masonry arches and shall provide a guideline path towards solving real-world engineering problems, as typically by established or novel numerical techniques, based on the achievements of underlying fundamental analytical solutions.

Indeed, the role of analytical solutions shall always be taken as superior, to that of numerical realizations, which generally come up to arise once analytical treatments are not possible, or when real specificities and peculiar morphologies must necessarily be addressed. The present considered setting, of symmetric circular continuous masonry arches, allows for a complete (wholly novel) analytical treatment, in the realm of finite friction, corroborated by numerical verifications, and then the relevant outcomes shall constitute a basic reference, even for other problems, and also in case of practical ones, that may need for appropriate numerical descriptions, for instance for discrete arches (made of blocks), unsymmetrical configurations, different loading setups, and so on.

The delivered information, on least-thickness evaluation, and characteristic amount of inherent friction, at variable arch opening, to draw collapse features, shall always provide a general instruction, for the (numerical) structural analysis of specific arch geometries, for instance in order to set appropriate pre-dimensioning in terms of arch thickness and seeking the amount of friction that shall be warranted, within the masonry structure, for the arch to withstand.

### 3 Extremal conditions

The analysis on the local stationary conditions on  $\hat{h}$  (maximum intrinsic non-dimensional horizontal thrust  $\hat{h} = H/(\gamma dr^2)$ , thus maximum horizontal thrust  $H$ , at given external arch characteristics  $\gamma; d, r$  that can be transferred within the circular masonry arch) and on  $\beta = \beta_r$  (widest inner-hinge angular position from the crown) starts from the purely-rotational solution, at infinite or finite undefined supercritical friction coefficient  $\mu$ .

Having in mind top plot  $\hat{h}(\beta)$  reported in Fig. 2, given that  $\hat{h}(\beta) = \eta(\beta)h(\beta)$ , meant as a function of  $\beta = \beta_r$ , from the explicit representation of the **purely-rotational solution**, in terms of function  $\hat{h}_M(\beta)$ , Eq. (9), or in terms of functions  $\eta_M(\beta), h_M(\beta)$  [47], one has, by the chain rule of differentiation, or alternatively through the implicit use of source 3rd-order polynomial equation  $pol_{\hat{h}}^M = 0$  in Eq. (7) [45]:

- The **horizontal tangency stationary condition on  $\hat{h}$**  (on first branch  $\hat{h}_M^- = \eta_M^- h_M^+$  of the purely-rotational solution) as:

$$\left\{ \begin{array}{l} \hat{h} = \hat{h}_M(\beta) = \eta_M(\beta) h_M(\beta) \\ \frac{\partial \hat{h}}{\partial \beta} = \frac{\partial \eta}{\partial \beta} h + \eta \frac{\partial h}{\partial \beta} = 0 \end{array} \right. \Leftrightarrow \left\{ \begin{array}{l} pol_{\hat{h}}^M(\beta, \hat{h}) = a \hat{h}^3 + b \hat{h}^2 + c \hat{h} + d = 0 \\ \frac{\partial pol_{\hat{h}}}{\partial \beta} = a' \hat{h}^3 + b' \hat{h}^2 + c' \hat{h} + d' = 0 \end{array} \right. \quad (15)$$

where, from above Eq. (7), polynomial coefficients  $a, b, c, d$  (and associated ' derivatives with respect to  $\beta$ ) are functions of  $\beta$ :

$$\left\{ \begin{array}{l} a = 2S^3, \\ b = -3S(g-f)(f+g+2S), \\ c = 6(g-f)^2(f+2S), \\ d = -8(g-f)^3 \end{array} \right. \quad (16)$$

leading to an implicit transcendental equation in  $\beta$ :

$$\begin{aligned} & (ad' - a'd)^3 + \\ & (bd' - b'd)^2(ab' - a'b) + (ac' - a'c)^2(cd' - c'd) - (ad' - a'd)^2(bc' - b'c) - \\ & (ab' - a'b)(cd' - c'd)((bc' - b'c) + 3(ad' - a'd)) = 0 \end{aligned} \quad (17)$$

and eventually to:

$$\beta_{r,s\hat{h}}^M = 1.115492876804752 \simeq 63.91^\circ \Rightarrow \hat{h}_{s\hat{h}}^M = 0.1123019151906599 \quad (18)$$

- The **vertical tangency stationary condition on  $\beta$**  (on either thereby re-joining branch of the  $\hat{h}_M(\beta)$  solution) as:

$$\left\{ \begin{array}{l} \hat{h} = \hat{h}_M(\beta) = \eta_M(\beta) h_M(\beta) \\ \frac{\partial \beta}{\partial \hat{h}} = \left( \frac{\partial \hat{h}}{\partial \beta} \right)^{-1} = \left( \frac{\partial \eta}{\partial \beta} h + \eta \frac{\partial h}{\partial \beta} \right)^{-1} = 0 \end{array} \right. \Leftrightarrow \left\{ \begin{array}{l} pol_{\hat{h}}^M(\beta, \hat{h}) = a \hat{h}^3 + b \hat{h}^2 + c \hat{h} + d = 0 \\ \frac{\partial pol_{\hat{h}}}{\partial \hat{h}} = 3a \hat{h}^2 + 2b \hat{h} + c = 0 \end{array} \right. \quad (19)$$

leading to an implicit transcendental equation in  $\beta$ , linked to the vanishing of the cubic

discriminant of  $\text{pol}_{\hat{h}}^M$ , Eq. (7), or of (the opposite of) the term under square root in  $SQRT$ , Eq. (10):

$$\Delta = c^2(b^2 - 4ac) - d(4b^3 + 27a^2d - 18abc) = -SQRT^2 = 0 \quad (20)$$

and eventually to:

$$\beta_{r,s\beta}^M = 1.119864231443752 \simeq 64.16^\circ \Rightarrow \hat{h}_{s\beta}^M = 0.1104057302144935 \quad (21)$$

The two obtained stationary states turn out rather near, to each other, with  $\beta_r$  around  $64^\circ$ , and  $\hat{h}$  at about 0.11, though keeping distinct.

Extending now such a purely-rotational stationary analysis to the domain of **finite-friction solutions**, the following derivation considerations are in order:

- Stationary points, of  $\hat{h}$  and  $\beta = \beta_r$ , from the purely-rotational solution, at constant  $\alpha$  and decreasing  $\mu$ , come to lie at the right *ss* interface from the origin to Triple point T of the inner pond of mixed sliding-rotational modes in the  $\eta$ - $\mu$  plots in Figs. 3-4.
- Thereby, and all within such an inner pond, up to the left *is* branch of further inner-sliding activation, the running governing equations are  $h = h_1(\beta, \eta) = h_e(\beta, \eta)$  (which by elimination of  $h$  render polynomial condition  $\text{pol}_\eta = 0$  [45–47], governing the  $\eta(\beta)$  solution), and  $\mu = \mu_{ss}(\alpha, h)$ , while in the left *is* frontier also condition  $\mu = \mu_{is}(h)$  applies.
- At given underlying  $\beta = \beta_r$ , both  $\eta$  and  $h$  are then set. In fact, from the  $h = h_1(\beta, \eta) = h_e(\beta, \eta)$  equations, one has  $\eta(\beta)$  and  $h(\beta)$ .
- Say that, if  $h = h_2(\alpha, \eta)$  is used,  $\alpha$  is associated to them through  $h_2$  (purely-rotational solution, South-East region of the  $\eta$ - $\mu$  plot), whereas if  $\mu = \mu_{ss}$  is used,  $\alpha$  is set through  $\mu_{ss}$  (inner pond of mixed sliding-rotational modes).
- Any  $\eta$  or  $h$  condition that is found on right *ss* or left *is* inner pond boundary extends as is to the other boundary, and to all points between them at constant  $\eta$  or  $h$ .
- At this stage, if this condition represents a stationary condition, e.g. of  $\hat{h}$  or of  $\beta$ , all points for the same underlying value of governing variable  $\beta = \beta_r$  result at the same quote.
- This creates a locus of maximum points, which are constant in  $\eta, h, \hat{h}$ , at variable  $\alpha$ , and  $\mu$ , so giving rise to a locus in the  $\alpha$ - $\mu$  plane, from  $\mu = \mu_{ss}$  up to  $\mu = \mu_{is}$ .
- In practice, stationary conditions (see specifically for the stationary condition on  $\beta_r$ , which is immaterial on the sliding equations) come only from equations  $h = h_1$  and  $h = h_e$ , from the side of the purely-rotational solution;  $\mu$  is brought in by either  $\mu_{ss}$ , on right *ss* inner pond border, or  $\mu_{is}$ , on left *is* inner pond border, as a mirroring effect, on  $\mu$ .
- Finally, concerning the stationarity on  $\beta_s = \sqrt{h(1-h)}$ , this is intrinsically obtained at inner-sliding activation, on left *is* branch of the inner pond region, for  $h = 0.5$  [42], and at a corresponding value of  $\mu = \mu_{is}(0.5)$ , and associated  $\alpha$ , through  $\mu = \mu_{ss}$ , while the value of  $\eta$  (and underlying  $\beta_r$ ) can be read, as above said, from equations  $h = h_1$ ,  $h = h_e$ , at that  $h = 0.5$ .

All this is manifested by the focused representation in Fig. 18 (and preceding two-dimensional projection plots), which shows the zoom of the  $\alpha$ - $\mu$  plot in Fig. 8 centred on the markings of the stationary states and associated loci, at variable  $\mu$  (and  $\alpha$ ), whereby peculiar stationary frontier points are scored, as also in the various representation maps, by (the same) specific markers. The characteristic data of such stationary points are reported in Tables 5-6.

Figure 18 indeed reports a zoom of the  $\alpha$ - $\mu$  plot in the zone where stationary points of  $\hat{h}$  and  $\beta_r$  appear, in the inner pond area of mixed sliding-rotational modes, below Triple point T (which actually also includes, a bit below the zoomed  $\alpha$  area, the marker corresponding to  $\beta_s^{max}$ , on the *is* branch reaching purely-sliding collapse at further inner-joint sliding activation).

Focusing on the rotational information, the following pertinent remarks apply, in the inspection of the zoomed  $\alpha$ - $\mu$  plot in Fig. 18:

- Coming from the right, at infinite or high supercritical friction, dotted paths at constant values  $\alpha_{sh}^M = 2.119284332007852 \simeq 121.43^\circ < \alpha_{s\beta}^M = 2.196404448812124 \simeq 125.84^\circ$  of the purely-rotational solution, marking respectively loci of same corresponding constant values of  $\hat{h}_{sh}^M = 0.1123019151906599$  and  $\beta_{s\beta}^M = 1.119864231443752 \simeq 64.16^\circ$ , reach the right *ss* branch below Triple point T, for shoulder-sliding activation.
- Then, they extend into the inner pond of mixed sliding-rotational modes, with a variation of  $\alpha$ , at variable  $\mu$ , with constant  $\hat{h}_{sh}$  and  $\beta_{s\beta}$ , meaning that loci of relative maximum points are created, at variable reducing friction (and concomitant  $\alpha$ ). This creates a little fork of values of  $\mu$  (and  $\alpha$ ) that can display the same stationary properties, thus with friction being able to spread a bit the range of maximum values coming from the purely-rotational solution, at further shoulder-sliding activation ruled by reducing friction.
- These loci of stationary points in the  $\alpha$ - $\mu$  plane stop once left *is* boundary of further inner-sliding activation is reached, leading to a purely-sliding interface.
- Obviously, on the loci of stationary points, the same relative quotes of  $\hat{h}$  and  $\beta_r$ , below at  $\hat{h}^{max}$ , above at  $\beta_r^{max}$ , are achieved for different  $\alpha$ - $\mu$  arch states.
- Such loci are monotonic, with decreasing  $\alpha$  at decreasing  $\mu$ , and  $\alpha$  for  $\hat{h}$  stationarity always lower than  $\alpha$  for  $\beta_r$  stationarity, meaning that the extremal properties for an arch can earlier be reached, at increasing  $\alpha$  (namely for lower  $\alpha$ ), if  $\mu$  is reduced. Thus, an arch with narrower opening may reach the same stationary values of the purely-rotational solution for a wider opening, if inherent friction is reduced. Conversely, if friction is increased, showing the structural effect of friction, in the self-bearing capacity of the masonry arch.
- Clearly, stationary loci are somehow “parallel” and do not intersect. Thus, there is no arch state that accumulates both  $\hat{h}$  and  $\beta_r$  stationarity, while such states are always separate.
- Also, at some  $\mu$  or  $\alpha$  value, between left/low limit of  $\beta_r^{max}$  locus and right/top limit of  $\hat{h}^{max}$  locus, there appear two (different)  $\alpha$  or  $\mu$  states having each a single stationary property. The horizontal  $\Delta\mu$  or vertical  $\Delta\alpha$  in such a range are almost constant, though differing a bit, along the loci. Therein, the vertical  $\Delta\alpha$  is lower (about one third) of the  $\Delta\alpha$  seen on the right for the purely-rotational solution. This shows the little spread that can be allowed, in considering finite friction, at constant  $\mu$  or  $\alpha$ , to display stationary points on  $\hat{h}$  and/or  $\beta_r$ .

- Finally, again, the point of  $\beta_s$  stationarity is made visible, in the various maps, with a specific marker, on left *is* branch of the inner pond of mixed sliding-rotational modes, with lower  $\alpha$  around 1.5 and lower  $\mu$  around 0.3 (see also characteristic values gathered in Tables 5-6).

Tables 5-6 resume the numerical data associated to the stationary points that are marked in the various analytical plots depicted in Figs. 3-18, respectively for  $\hat{h}$  and  $\beta_{r,s}$  stationarity.

Tables 5-6.

Figure 18.

### 3.1 Illustration of stationary arch states

Figures 19-23 finally report the arch morphologies, and relevant mechanical characteristics, recorded at the mentioned marked limits of the stationary points, computationally derived by the numerical “ $\varphi\text{-}\lambda$ ” CP/MP formulation [43, 44] referred to in Section 2.3, again reporting geometry in the least-thickness condition (black); lines of thrust (red) and of friction (blue); associated collapse mode (green).

Figures 19-23.

Specifically:

- Figure 19 shows the (slightly undercomplete) circular masonry arch with  $\alpha \simeq 88.40^\circ$  that displays the widest angular position from the crown of the inner-sliding joint, with  $\beta_s = \beta_s(h=0.5) = 0.5 \simeq 28.65^\circ$ , and  $\beta_r \simeq 59.85^\circ$ , at a (low) friction coefficient and angle of about  $\mu \simeq 0.2934$  and  $\varphi \simeq 16.35^\circ$ , displaying  $\eta \simeq 0.1876$  and  $\hat{h} \simeq 0.09381$  ( $h = 0.5$ ;  $\hat{h} = \eta/2$ ). As above commented, such a configuration is rather peculiar, since visually the arch looks almost complete ( $\alpha \simeq 90^\circ$ ), and inner failure joints appear at about each third ( $\beta_s \simeq 30^\circ$  and  $\beta_r \simeq 60^\circ$ ) of half-arch opening. Noticeably, a rather low friction is required, to attain such a configuration with widest inner sliding location, which may anyway result of a physical interest, for complete or about complete arches that may display a lowering friction, for various possible manifesting conditions. Still, the arch is able to transfer an intrinsic horizontal thrust that is not much lower than that that is going to be shown, next, for the configurations that display a maximum value of  $\hat{h}$ , and also than those that attain a maximum angular position of the inner rotational joint (see also positioning of the relevant markers, on *is* and *ss* branches, in the various two-dimensional projection maps in Figs. 3-18).
- The two collapse mechanisms that are concomitantly represented, in Fig. 19, in correspondence of that arising point of the *is* boundary of the inner pond, namely a sliding-rotational mode, with shoulder sliding and inner rotation, and a purely-sliding mode, with shoulder and inner-joint sliding, are depicted, while any linear combination of them may represent the possible collapse mode at that point (of a double collapse multiplicity, as discussed in the next section).

- Figures 20-21 depict the (overcomplete) arch configurations that, on the two *is* and *ss* extremes, respectively, produce the maximum intrinsic horizontal thrust within the masonry arch, at near  $\hat{h} \simeq 0.1123$ , with  $\beta_r \simeq 63.91^\circ$ , and  $\eta \simeq 0.3436$ . The left marker on the *is* branch is characterized by  $\alpha \simeq 108.46^\circ$ , once  $\mu \simeq 0.5374$  and  $\varphi \simeq 28.25^\circ$ , while  $\beta_s \simeq 26.88^\circ$ ; the right marker on the *ss* branch is characterized by  $\alpha \simeq 121.43^\circ$ , once  $\mu \simeq 0.8449$  and  $\varphi \simeq 40.19^\circ$ . The fork of half-arch openings and friction angles along the stationary locus of  $\hat{h}$ , across the *is* and *ss* branches (see zoom in Fig. 18) then spreads over about the angular variations of  $\Delta\alpha \simeq 12.97^\circ \simeq 13^\circ$  and  $\Delta\varphi \simeq 11.94^\circ \simeq 12^\circ$ . Such angle ranges turn out rather similar, and quite contained, though extending a bit the role of the classical purely-rotational solution, at infinite or supercritical friction, in estimating the maximum intrinsic horizontal thrust. As per the preceding figure, the left point on the *is* branch displays the sliding-rotational and purely-sliding mechanisms, with given  $\beta_s \simeq 27^\circ$  (Fig. 20), while the right point on the *ss* branch illustrates the sliding-rotational and purely-rotational mechanisms, with no inner sliding joint (Fig. 21), which may again linearly be combined at that point.
- Figures 22-23 report the (further overcomplete) arch configurations that, on the two *is* and *ss* branches, respectively, produce the widest angular position of the inner-rotational joint, at near  $\beta_r \simeq 64.16^\circ$ , with  $\hat{h} \simeq 0.1104$ , and  $\eta \simeq 0.3976$ . The left marker on the *is* branch is characterized by  $\alpha \simeq 114.64^\circ$ , once  $\mu \simeq 0.6380$  and  $\varphi \simeq 32.54^\circ$ , while thereby  $\beta_s \simeq 25.66^\circ$ ; the right marker on the *ss* branch is characterized by  $\alpha \simeq 125.84^\circ$ , once  $\mu \simeq 0.9342$  and  $\varphi \simeq 43.05^\circ$ . The fork of half-arch openings and friction angles along the stationary locus of  $\beta_r$ , across the *is* and *ss* branches (see zoom plot in Fig. 18) then spreads over angular variations of about  $\Delta\alpha \simeq 11.20^\circ$  and  $\Delta\varphi \simeq 10.51^\circ$ , say around  $11^\circ$  for both angle ranges.
- Notice that, for both stationary  $\hat{h}^{\max}$  (Figs. 20-21) and  $\beta_r^{\max}$  (Figs. 22-23),  $\hat{h}$  results around 0.11,  $\beta_r$  around  $64^\circ$  and  $\beta_s$  around  $26^\circ$ . Moreover, jumping from  $\hat{h}^{\max}$  to  $\beta_r^{\max}$ , along the *is* branch, one has the angular variations of  $\Delta\alpha^{is} \simeq 6.18^\circ$ ,  $\Delta\varphi^{is} \simeq 4.29^\circ$  and, along the *ss* branch, of  $\Delta\alpha^{ss} \simeq 4.41^\circ$ ,  $\Delta\varphi^{ss} \simeq 2.86^\circ$ , so that, indeed, the various marked stationary points turn out quite near, to each other, in the projection map in Fig. 8, and relevant zoom in Fig. 18 (and also in the other two-dimensional projection maps), meaning that, on the two sliding activation branches, *is* and *ss*, the  $\alpha$ - $\mu$  states result very close, to each other, in achieving  $\hat{h}^{\max}$  and  $\beta_r^{\max}$ .

## 4 Collapse mode multiplicity

The appearance of a landmark, watershed point in the  $\eta\text{-}\mu$  plane (named “Triple point T”), where all four main regions of the collapse states, namely purely-rotational, mixed sliding-rotational, mixed rotational-sliding and purely-sliding, touch together, on such a peculiar conjunction point (Figs. 3-4), raises the question of the kinematical-mathematical multiplicity, among the collapse modes, that is truly present at that point. In other words, while thereby four physical modes are concomitantly present, so the physical multiplicity is four, one wonders if a linear dependence of the underlying collapse mechanisms may subsist, so that the point should not constitute a “quadruple” point (i.e. should constitute a less than “quadruple” point), in terms of kinematical-mathematical multiplicity.

For instance, intuitively, the mixed rotational-sliding mode, which is the only one that displays three active joints, rotational at the shoulder, rotational at an inner rotational joint and sliding at a (different) inner sliding joint, may possibly be conceived as a linear combination of the other three mechanisms, each activating only two failure joints. So, in looking at the filled  $\eta\text{-}\mu$  plot in Fig. 3, one may think that re-joining, at point T, South-East region of purely-rotational modes, North-West region of purely-sliding modes, and inner pond region of mixed sliding-rotational modes among them, left from T, this shall make a region of mixed rotational-sliding modes to arise, right from T and still in between the two purely-rotational and purely-sliding regions below and above.

Then, one may be led to name such a point as Triple point (T). Despite, the same reasoning may be expressed with any three of the four regions pinning at point T, to define, by any (triple) linear combination, the collapse modes of the other one. Thus, the conjecture may be that the kinematical-mathematical multiplicity, of such a peculiar direct-connection point, shall be  $m = 3$ .

This calls for a quick mechanical investigation, from the side of pure kinematics (thus independently from equilibrium and limit conditions earlier analyzed, in particular linked to finite-friction coefficient  $\mu$  and relevant effects), and underlying mathematics (linear algebra), for a general (symmetric) arch state, based on the basic collapse modes that have been discovered, from the previous analytical analysis.

The kinematical characteristics of the four basic collapse modes, with connected maps of horizontal and vertical displacements, are analytically depicted in Figs. 24-27 (thereby with reference to the geometrical features indeed displayed at Triple point T, see also Table 1, although the analysis is herein made general, in terms of the involved underlying parametric geometrical variables of the circular arch, namely for generic  $\eta, \alpha, \beta_r, \beta_s$ ).

Figures 24-27.

### 4.1 Kinematical description

Toward the kinematical description, of the generic collapse mechanism, based on the four underlying physical modes that have analytically been discovered, one may conceive a linear transformation mapping, from the degrees of freedom (lagrangian coordinates) that may be chosen to represent the four recorded collapse modes, and the displacement variables that may adequately describe the generic (symmetric) collapse mechanism that may form within the (symmetric) circular masonry arch.

To achieve that, lagrangian coordinates are selected, indicating the (clockwise) rotation of the shoulder rotational joint, for the Purely-Rotational mode (PR),  $\psi_{PR}$ , and for the mixed Rotational-Sliding mode (RS),  $\psi_{SR}$ , and the (centrifugal) sliding displacement of the shoulder sliding joint, for the mixed Sliding-Rotational mode (SR),  $s_{SR}$ , and for the Purely-Sliding mode (PS),  $s_{PS}$ . To make mutually uniform, rotations and displacements, to same (e.g. displacement) dimensions, rotations are multiplied by a geometrical length parameter, herein taken by radius  $r$  of the circular arch, as coming from the displacement maps. These form  $4 \times 1$  lagrangian coordinate (column) vector  $\mathbf{q}$  associated to the basic four underlying symmetric collapse modes (superscript  $T$  meaning transpose):

$$\mathbf{q}^T = \{r \psi_{PR}, s_{SR}, r \psi_{RS}, s_{PS}\} \quad (22)$$

Conversely, to reconstruct the general (symmetric) collapse mode of the circular arch, from the movements of the blocks, among arising failure joints, for instance by assembling it from the underneath, bearing shoulder, joint displacements are selected, indicating the (clockwise) rotation at the shoulder rotational joint, at  $\beta = \alpha$ ,  $\psi_s$ , and the (centrifugal) sliding displacement at the shoulder sliding joint (referring to the block resting above the shoulder joint), still at  $\beta = \alpha$ ,  $s_s$ , and the (counterclockwise) out-opening rotation of the inner rotational joint at  $\beta = \beta_r$ ,  $\psi_i$ , and the (centripetal) sliding displacement at the inner sliding joint, at  $\beta = \beta_s$  (again referring to the block that lays above the inner sliding joint),  $s_i$ . With rotations again assimilated to displacements, through multiplication by  $r$ , these kinematical variables form  $4 \times 1$  joint displacement (column) vector  $\mathbf{u}$  of the generic symmetric collapse mode:

$$\mathbf{u}^T = \{r \psi_s, s_s, r \psi_i, s_i\} \quad (23)$$

Notice that this is a reduced set of (four) variables that allows to reconstruct the (symmetric) movement, of the half arch, with two blocks piling from the shoulder, while the movement at the crown symmetry section or of a third keystone block comes as a consequence, thus can be avoided, to be represented, within the kinematical mapping, to work with both  $4 \times 1$  kinematical vectors, and then obtain a corresponding square  $4 \times 4$  kinematical transformation matrix, as follows.

Indeed, after the selections above, the following linear transformation kinematical mapping may be outlined, from vector  $\mathbf{q}$  to vector  $\mathbf{u}$ , through  $4 \times 4$  compatibility matrix  $\mathbf{C}$ , which may readily be compiled by columns, as attached to the selected entries in lagrangian vector  $\mathbf{q}$ :

$$\mathbf{u} = \begin{Bmatrix} r \psi_s \\ s_s \\ r \psi_i \\ s_i \end{Bmatrix} = \begin{bmatrix} 1 & 0 & 1 & 0 \\ 0 & 1 & 0 & 1 \\ C_{31} & C_{32} & 1 & 0 \\ 0 & 0 & C_{43} & C_{44} \end{bmatrix} \cdot \begin{Bmatrix} r \psi_{PR} \\ s_{SR} \\ r \psi_{RS} \\ s_{PS} \end{Bmatrix} = \mathbf{C} \cdot \mathbf{q} \quad (24)$$

where the non-binary matrix coefficients (i.e. those different from 0 and 1, the latter being easily apparent), namely  $C_{31}$ ,  $C_{32}$  and  $C_{43}$ ,  $C_{44}$ , concerning information at the inner rotational and sliding failure joints, which are functions of the free geometrical variables of the circular arch (i.e.  $\eta$ ,  $\alpha$ ,  $\beta_r$ ,  $\beta_s$ ), can kinematically be derived as:

$$\begin{cases} C_{31} = \frac{(2+\eta)(1-\cos\alpha)}{2+\eta-(2-\eta)\cos\beta_r} \\ C_{32} = \frac{2\sin\alpha}{2+\eta-(2-\eta)\cos\beta_r} \\ C_{43} = -\frac{(2+\eta)\cos\alpha-(2-\eta)\cos\beta_r}{2\sin\beta_s} \\ C_{44} = \frac{\sin\alpha}{\sin\beta_s} \end{cases} \quad (25)$$

In fact:

- from the map of horizontal displacements of the Purely-Rotational mode in Fig. 24 ( $\psi_l = \psi_{PR}$  rotation of lower block;  $\psi_u$  rotation of upper block;  $\psi_i = \psi_{lu} = \psi_l + \psi_u$  relative rotation among lower and upper block):

$$\psi_u \cdot r \left[ \left(1 + \frac{\eta}{2}\right) - \left(1 - \frac{\eta}{2}\right) \cos\beta_r \right] = \psi_l \cdot r \left[ -\left(1 + \frac{\eta}{2}\right) \cos\alpha + \left(1 - \frac{\eta}{2}\right) \cos\beta_r \right] \quad (26)$$

and

$$\psi_{lu} \cdot r \left[ \left(1 + \frac{\eta}{2}\right) - \left(1 - \frac{\eta}{2}\right) \cos\beta_r \right] = \psi_l \cdot r \left(1 + \frac{\eta}{2}\right) (1 - \cos\alpha) \quad (27)$$

then

$$r \psi_i = \frac{(2+\eta)(1-\cos\alpha)}{2+\eta-(2-\eta)\cos\beta_r} r \psi_{PR} = C_{31} r \psi_{PR} \quad (28)$$

- from the map of horizontal displacements of the mixed Sliding-Rotational mode in Fig. 25:

$$\psi_i \cdot r \left[ \left(1 + \frac{\eta}{2}\right) - \left(1 - \frac{\eta}{2}\right) \cos\beta_r \right] = s_{SR} \sin\alpha \quad (29)$$

then

$$r \psi_i = \frac{2\sin\alpha}{2+\eta-(2-\eta)\cos\beta_r} s_{SR} = C_{32} s_{SR} \quad (30)$$

Incidentally, the following relations among  $C_{31}$  and  $C_{32}$  may be recorded:

$$\frac{C_{31}}{(2+\eta)(1-\cos\alpha)} = \frac{C_{32}}{2\sin\alpha} \Rightarrow \frac{C_{31}}{C_{32}} = \frac{(2+\eta)(1-\cos\alpha)}{2\sin\alpha} \quad (31)$$

- from the map of horizontal displacements of the mixed Rotational-Sliding mode in Fig. 26:

$$\psi_{RS} \cdot r \left[ -\left(1 + \frac{\eta}{2}\right) \cos\alpha + \left(1 - \frac{\eta}{2}\right) \cos\beta_r \right] = s_i \sin\beta_s \quad (32)$$

then

$$s_i = -\frac{(2+\eta)\cos\alpha-(2-\eta)\cos\beta_r}{2\sin\beta_s} r \psi_{RS} = C_{43} r \psi_{RS} \quad (33)$$

- from the (map of) horizontal displacements of the Purely-Sliding mode in Fig. 27:

$$u = s_{PS} \sin\alpha = s_i \sin\beta_s \quad (34)$$

then

$$s_i = \frac{\sin\alpha}{\sin\beta_s} s_{PS} = C_{44} s_{PS} \quad (35)$$

Incidentally, the following relations among  $C_{43}$  and  $C_{44}$  may be recorded:

$$-\frac{2C_{43}}{(2+\eta)\cos\alpha-(2-\eta)\cos\beta_r} = \frac{C_{44}}{\sin\alpha} \Rightarrow \frac{C_{43}}{C_{44}} = -\frac{(2+\eta)\cos\alpha-(2-\eta)\cos\beta_r}{2\sin\alpha} \quad (36)$$

Now, the determinant of compatibility matrix  $\mathbf{C}$  can readily be calculated, and checked to identically vanish, given the expressions of the non-binary kinematical coefficients reported in Eqs. (25):

$$\begin{aligned} \det \mathbf{C} &= \begin{vmatrix} 1 & 0 & 1 \\ C_{32} & 1 & 0 \\ 0 & C_{43} & C_{44} \end{vmatrix} + \begin{vmatrix} 0 & 1 & 1 \\ C_{31} & C_{32} & 0 \\ 0 & 0 & C_{44} \end{vmatrix} \\ &= \begin{vmatrix} 1 & 0 \\ C_{43} & C_{44} \end{vmatrix} + \begin{vmatrix} C_{32} & 1 \\ 0 & C_{43} \end{vmatrix} - C_{31}C_{44} \\ &= C_{44} + C_{32}C_{43} - C_{31}C_{44} \\ &= (1 - C_{31})C_{44} + C_{32}C_{43} \\ &\equiv 0 \end{aligned} \quad (37)$$

thus, with

$$\frac{C_{31}-1}{C_{32}} = \frac{C_{43}}{C_{44}} = -\frac{(2+\eta)\cos\alpha-(2-\eta)\cos\beta_r}{2\sin\alpha} \quad (38)$$

being above coefficient ratios eventually independent from  $\beta_s$  (i.e. of inner sliding joint angular position).

Thus, compatibility matrix  $\mathbf{C}$  turns out singular, and there subsists a linear dependency among PR, SR, RS and PS collapse mechanisms, and an underlying rank deficiency of matrix  $\mathbf{C}$ . Moreover, it can be checked that

$$m = \text{rank } \mathbf{C} = 3 \quad (39)$$

so that there appears one linear dependency among the four basic collapse modes and one rank deficiency of kinematical transformation matrix  $\mathbf{C}$ .

Furthermore, the following self-coherent statements may be extracted, from the algebraic properties of compatibility matrix  $\mathbf{C}$ :

- By eliminating any column from matrix  $\mathbf{C}$ , meaning one of the four basic mechanisms,  $m = \text{rank } \mathbf{C}_3 = 3$ , so that the other three modes are anyway linearly independent, and mathematical multiplicity is 3 (specifically at Triple point T, where all four main collapse domains physically touch, and all four basic collapse modes are mechanically present).
- By eliminating any two columns from matrix  $\mathbf{C}$ , meaning two of the four basic mechanisms,  $m = \text{rank } \mathbf{C}_2 = 2$ , so that the other two modes are anyway linearly independent (as obvious), and mathematical multiplicity is 2 (double points at the interfaces of the physical collapse domains).
- By eliminating any three columns from matrix  $\mathbf{C}$ , meaning three of the four basic mechanisms,  $m = \text{rank } \mathbf{C}_1 = 1$ , so that the other mode is anyway linearly independent (as obvious), and mathematical multiplicity is 1 (single points belonging to the various physical collapse domains).

Finally, the system eigensolution, i.e. the single basis vector of the null space of singular compatibility matrix  $\mathbf{C}$ , namely the eigenvector associated to its zero eigenvalue, may readily be obtained from homogeneous system  $\mathbf{C} \cdot \mathbf{q} = \mathbf{0}$  attached to Eq. (24) as:

$$\begin{cases} r\psi_{PR} + r\psi_{RS} = 0 \\ s_{SR} + s_{PS} = 0 \\ C_{31}r\psi_{PR} + C_{32}s_{SR} + r\psi_{RS} = 0 \\ C_{43}r\psi_{RS} + C_{44}s_{PS} = 0 \end{cases} \quad (40)$$

leading, for instance, by taking 1st, 2nd and 4th lines, and pivoting on  $r\psi_{PR}$ :

$$\begin{cases} r\psi_{RS} = -r\psi_{PR} \\ s_{SR} = -s_{PS} = -\frac{C_{43}}{C_{44}}r\psi_{PR} \\ s_{PS} = -\frac{C_{43}}{C_{44}}r\psi_{RS} = \frac{C_{43}}{C_{44}}r\psi_{PR} \end{cases} \quad (41)$$

and then

$$\mathbf{q}_0^T = r\psi_{PR} \left\{ 1, -\frac{C_{43}}{C_{44}}, -1, \frac{C_{43}}{C_{44}} \right\} \quad (42)$$

with  $C_{43}/C_{44}$  ratio given in Eqs. (36), (38), independently from  $\beta_s$ . This expresses the kinematic link among the four basic mechanisms (for any arch state, and holding, in particular, with statical and limit admissibility constraints, as also linked to finite-friction coefficient  $\mu$ , at Triple point T), for instance as a function of purely-rotational mode amplitude, for the other three mode amplitudes.

Specifically, at watershed Triple point T (superscript  $T$ ), where geometrical data have been found as (Table 1):

$$\begin{cases} \eta^T = 0.6183182410743234 \simeq 0.6183 \\ \alpha^T = 2.430069103769349 \simeq 2.430 \\ \beta_r^T = 1.042556808593599 \simeq 1.043 \\ \beta_s^T = 0.3187321853045027 \simeq 0.3187 \end{cases} \quad (43)$$

the following characteristic kinematical coefficient values and coefficient ratios are recorded:

$$\begin{cases} C_{31}^T = 2.394126742272506 \simeq 2.394 \\ C_{32}^T = 0.6795125638228773 \simeq 0.6795 \\ C_{43}^T = 4.275261961259677 \simeq 4.275 \\ C_{44}^T = 2.083809260824103 \simeq 2.084 \end{cases} \quad (44)$$

$$\begin{cases} \frac{C_{31}^T}{C_{32}^T} = 3.523300185655673 \simeq 3.523 \\ \frac{C_{43}^T}{C_{44}^T} = 2.051657050208568 \simeq 2.052 \end{cases} \quad (45)$$

and then

$$\mathbf{q}_0^{T^T} \simeq r\psi_{PR} \{ 1, -2.052, -1, 2.052 \} \quad (46)$$

## 5 Conclusions

This paper has constituted a further addendum to a comprehensive analytical analysis on the role of finite friction in the statics of masonry arches, with reference to the classical least-thickness optimization “Couplet-Heyman problem” for symmetric circular continuous masonry arches under uniform self-weight, as first developed in source work [46] and then in compendium paper [47].

It has derived new specific characteristic features, namely:

- (a) The complete analytical two- and three-dimensional maps of the underlying mechanical solution variables, and attached limit collapse states, at variable governing parameters, of half-arch opening and friction coefficient.
- (b) The stationary (maximum) conditions of intrinsic non-dimensional horizontal thrust and widest inner-joint (rotational and sliding) angular positions, in the presence of finite, variable friction.
- (c) The physical/mathematical multiplicity of the underlying collapse mechanisms, in revealing the possible failure modes involving sliding, at releasing the hypothesis of high-enough or infinite friction.

The delivered analytical analysis physically reveals that:

- A limited amount of friction may lead to earlier achieve critical self-standing conditions, at lowering opening angle of the arch, meaning that mechanical features of an arch for a higher friction coefficient with a specific opening angle may already be reached by an arch with lower friction coefficient at a smaller opening angle. Then, macroscopically, the track of feasible states in terms of opening angle and friction coefficient is basically monotonically increasing/decreasing along a macro line. This shall say that, overall, an arch with a wider opening shall require higher friction, to withstand under self-weight.
- Accordingly, the least thickness-to-radius ratio registers a decrease and the inherent horizontal non-dimensional horizontal thrust records an increase, at decreasing friction coefficient.
- On the other hand, the intrinsic non-dimensional horizontal thrust that the arch is able to transfer, at given arch characteristics (specific weight, out-of-plane depth and radius), confirms non-monotonic, in the presence of finite friction. Thereby, stationarity and extremal (maximum) conditions are a bit moved, and spread over loci, by the amount of inherent friction, and the associated range of opening angles is widened, in showing a maximum horizontal thrust transfer.
- Similarly, the rotational/sliding inner-joint angular positions are non-monotonically conditioned by finite friction, and stationarity conditions for inner rotational joints are widened, as above, while the extremal condition for an inner sliding joint is reached just for a specific arch opening and friction state. Also, opening angles for inner rotational joints are first wider, than for sliding joints, at lower friction, but then come to the opposite, at increasing friction, while the angular inner-hinge position pulls back toward the crown, at increasing friction coefficient and opening angle, leading to overturning modes.

The investigation looks quite instructive, because it shows how the amount of inherent friction may limit the self-supporting capacity of masonry arches. Hereby, this is revealed, analytically, for the conveniently tractable geometry of the circular arch, within a symmetric setting. Additional extensive general and specific considerations, on the outcomes of the present analysis, and their framing, within the existing literature, are delivered in source work [46] and companion addendum [47], including for the potential issue of non-uniqueness, on the least-thickness evaluation, in the presence of non-normality of the flow-rule, as linked to the account of finite friction, which is herein un-recorded (see specifically discussion in [46], and also general framing just appeared in this same Journal in [33]), within the present setting of symmetric circular masonry arches under uniform self-weight.

Further endeavours may concern implications for non-symmetric circular arches or for arches with different geometries, or external conditions, likely then by recurring to numerical treatments, whenever the explicit analytical handling may become unfeasible. However, the present methodological handling allows to unveil crucial characteristic features, for a global understanding of the mechanical behaviour of such peculiar self-supporting curvilinear structures, specifically for the structural role that shall be played by the inherent friction.

## Acknowledgments

This work has been developed at the University of Bergamo, School of Engineering (Dalmine). The support by ministerial (MUR) funding “Fondi di Ricerca d’Ateneo ex 60%” at the University of Bergamo is gratefully acknowledged.

## Compliance with Ethical Standards

The authors declare that they have no conflict of interest.

## References

- [1] Milankovitch, M. (1907). Theorie der Druckkurven, Zeitschrift für Mathematik und Physik, 55, pp. 1-27.
- [2] Foce, F. (2007). Milankovitch's Theorie der Druckkurven: Good mechanics for masonry architecture, *Nexus Network Journal*, 9(2), pp. 185-210. DOI: 10.1007/s00004-007-0039-9.
- [3] Heyman, J. (1969). The safety of masonry arches, *International Journal of Mechanical Sciences*, 11(4), pp. 363-385. DOI: 10.1016/0020-7403(69)90070-8.
- [4] Heyman, J. (2009). La coupe des pierres, In: Proceedings of the 3rd International Congress on Construction History, Brandenburg University of Technology, Cottbus, Germany, 20–24 May 2009, 2, pp. 807–812.
- [5] Kooharian, A. (1952). Limit analysis of voussoir (segmental) and concrete arches, *Journal Proceedings of the American Concrete Institute*, 49(12), pp. 317-328. DOI: 10.14359/11822.
- [6] Livesley, R.K. (1978). Limit analysis of structures formed from rigid blocks, *International Journal for Numerical and Analytical Methods in Engineering*, 12(12), pp. 1853-1871. DOI: 10.1002/nme.1620121207.
- [7] Livesley, R.K. (1992). A computational model for the limit analysis of three-dimensional masonry structures, *Meccanica*, 27(3), pp. 161-172. DOI: 10.1007/BF00430042.
- [8] Como, M. (1992). Equilibrium and collapse of masonry bodies, *Meccanica*, 27(3), pp. 185-194. DOI: 10.1007/BF00430044.
- [9] Boothby, T.E., Brown C.B. (1992). Stability of masonry piers and arches, *Journal of Engineering Mechanics*, ASCE, 118(2), pp. 367–383. DOI: 10.1061/(ASCE)0733-9399(1992)118:2(367).
- [10] Boothby, T.E. (1996). Analytical approach to collapse mechanisms of circular masonry arch. Discussion on the paper by Blasi and Foraboschi (1994), with Closure by P. Foraboschi and C. Blasi, *Journal of Structural Engineering*, ASCE, 122(8), pp. 978-980. DOI: 10.1061/(ASCE)0733-9445(1996)122:8(978).
- [11] Blasi, C., Foraboschi, P. (1994). Analytical approach to collapse mechanisms of circular masonry arch, *Journal of Structural Engineering*, ASCE, 120(8), pp. 2288-2309. DOI: 10.1061/(ASCE)0733-9445(1994)120:8(2288).
- [12] Lucchesi, M., Padovani, C., Pasquinelli, G., Zani, N. (1997). On the collapse of masonry arches, *Meccanica*, 32(4), pp. 327-346. DOI: 10.1023/A:1004275223879.
- [13] Ochsendorf, J.A. (2006). The masonry arch on spreading supports, *The Structural Engineer*, 84(2), pp. 29-36.
- [14] Romano, A., Ochsendorf, J.A. (2009). The mechanics of Gothic masonry arches, *International Journal of Architectural Heritage*, 4(1), pp. 59–82. DOI: 10.1080/15583050902914660.
- [15] Block, P., DeJong, M., Ochsendorf, J. (2006). As hangs the flexible line: equilibrium of masonry arches, *Nexus Network Journal*, 8(2), pp. 13-24. DOI: 10.1007/s00004-006-0015-9.

- [16] Alexakis, H., Makris, N. (2015). Limit equilibrium analysis of masonry arches, *Archive of Applied Mechanics*, 85(9-10), pp. 1363-1381. DOI: 10.1007/s00419-014-0963-6.
- [17] Nikolić, D. (2017). Thrust line analysis and the minimum thickness of pointed masonry arches, *Acta Mechanica*, 228(6), pp. 2219-2236. DOI: 10.1007/s00707-017-1823-6.
- [18] Gáspár, O., Sipos, A.A., Sajtos, I. (2018). Effect of stereotomy on the lower bound value of minimum thickness of semi-circular masonry arches, *International Journal of Architectural Heritage*, 12(6), pp. 899-921. DOI: 10.1080/15583058.2017.1422572.
- [19] Gáspár, O., Sajtos, I., Sipos, A.A. (2022). Multi-hinge failure mechanisms of masonry arches subject to self-weight as derived from minimum thickness analysis, *International Journal of Architectural Heritage*, 17(12), pp. 1921-1949. DOI: 10.1080/15583058.2022.2084702.
- [20] Nodargi, N.A., Bisegna, P. (2020). Thrust line analysis revisited and applied to optimization of masonry arches, *International Journal of Mechanical Sciences*, 179(1 August 2020), 105690179, pp. 1-13. DOI: 10.1016/j.ijmecsci.2020.105690.
- [21] Drucker, D.C. (1954). Coulomb friction, plasticity, and limit loads, *Journal of Applied Mechanics*, 21(1), pp. 71-74. DOI: 10.1115/1.4010821.
- [22] Boothby, T.E. (1994). Stability of masonry piers and arches including sliding, *Journal of Engineering Mechanics*, ASCE, 120(2), pp. 304-319. DOI: 10.1061/(ASCE)0733-9399(1994)120:2(304).
- [23] Sinopoli, A., Corradi, M., Foce, F. (1997). Modern formulation for preelastic theories on masonry arches, *Journal of Engineering Mechanics*, ASCE, 123(3), pp. 204-213. DOI: 10.1061/(ASCE)0733-9399(1997)123:3(204).
- [24] Sinopoli, A., Aita, D., Foce, F. (2007). Further remarks on the collapse mode of masonry arches with Coulomb friction, *Proceedings of 5th International Conference on Arch Bridges (ARCH'07)*, Funchal, Madeira, Portugal, September 12-14, 2007, P.B. Lourenço, D.B. Oliveira, A. Portela (Eds.), Multicomp, Lda Publishers, Madeira, pp. 649-657.
- [25] Baggio, C., Trovalusci, P. (2000). Collapse behaviour of three-dimensional brick-block systems using non-linear programming, *Structural Engineering and Mechanics*, 10(2), pp. 181-195. DOI: 10.12989/sem.2000.10.2.181.
- [26] Rios, A.J., Nela, B., Pingaro, M., Reccia, E., Trovalusci, P. (2025). Parametric analysis of masonry arches following a limit analysis approach: Influence of joint friction, pier texture, and arch shallowness, *Mathematics and Mechanics of Solids*, OnlineFirst 11 July 2023, 30(1), pp. 137-165. DOI: 10.1177/10812865231175385.
- [27] Casapulla, C., Lauro, F. (2000). A simple computation tool for the limit-state analysis of masonry arches, *Proceedings of 5th International Congress on Restoration of Architectural Heritage*, Università di Firenze, 17-24 September 2000, CDROM Proc., pp. 2056-2064.
- [28] Gilbert, M., Casapulla, C., Ahmed, H.M. (2006). Limit analysis of masonry block structures with non-associative frictional joints using linear programming, *Computers and Structures*, 84(13-14), pp. 873-887. DOI: 10.1016/j.compstruc.2006.02.005.

- [29] Smars, P. (2010). Kinematic stability of masonry arches, *Advanced Materials Research*, 133-134, pp. 429-434. DOI: 10.4028/www.scientific.net/AMR.133-134.429.
- [30] D'Ayala, D., Tomasoni, E. (2011). Three-dimensional analysis of masonry vaults using limit state analysis with finite friction, *International Journal of Architectural Heritage*, 5(2), pp. 140-171. DOI: 10.1080/15583050903367595.
- [31] Trentadue, F., Quaranta, G. (2013). Limit analysis of frictional block assemblies by means of fictitious associative-type contact interface laws, *International Journal of Mechanical Sciences*, 70(May 2013), pp. 140-145. DOI: 10.1016/j.ijmecsci.2013.02.012.
- [32] Trentadue, F., De Tommasi, D., Marasciuolo, N., Vitucci, G. (2024). Thrust in a symmetric masonry arch with frictional joints on spreading supports, *Acta Mechanica*, 235(2), pp. 659-670. DOI: 10.1007/s00707-023-03759-0.
- [33] Trentadue, F., De Tommasi, D., Marasciuolo, N. (2025). A new approach to the limit analysis of masonry structures as assemblies of rigid-plastic blocks with frictional sliding contacts, *Structures*, 76(June 2025), 108895, pp. 1-7. DOI: 10.1016/j.istruc.2025.108895.
- [34] Bagi, K. (2014). When Heyman's Safe Theorem of rigid block systems fails: Non-Heymanian collapse modes of masonry structures, *International Journal of Solids and Structures*, 51(14), pp. 2696-2705. DOI: 10.1016/j.ijsolstr.2014.03.041.
- [35] Aita, D., Barsotti, R., Bennati, S. (2019). Looking at the collapse modes of circular and pointed masonry arches through the lens of Durand-Claye's stability area method, *Archive of Applied Mechanics*, 89(8), pp. 1537-1554. DOI: 10.1007/s00419-019-01526-z.
- [36] Aita, D., Barsotti, R., Bennati, S. (2021). Arch-piers systems subjected to vertical loads: a comprehensive review of rotational, sliding and mixed collapse modes, *Archive of Applied Mechanics*, 91(1), pp. 241-256. DOI: 10.1007/s00419-020-01766-4.
- [37] Aita, D., Bruggi, M., Garavaglia, E. (2024). Collapse analysis of masonry arches and domes considering finite friction and uncertainties in compressive strength, *Engineering Failure Analysis*, 163(Part A, September 2024), 108462, pp. 1-20. DOI: 10.1016/j.engfailanal.2024.108462.
- [38] Gáspár, O., Sajtos, I., Sipos, A.A. (2021). Friction as a geometric constraint on stereotomy in the minimum thickness analysis of circular and elliptical masonry arches, *International Journal of Solids and Structures*, 225(15 August 2021), 111056, pp. 1-18. DOI: 10.1016/j.ijsolstr.2021.111056.
- [39] Hua, Y., Milani, G. (2022). Rigid Block Limit Analysis of Masonry Arches with Associated and Non-associated Slides, in: G. Milani and V. Sarhosis (Eds.), *From Corbel Arches to Double Curvature Vaults*, Springer Nature Switzerland AG, pp. 169-203. DOI: 10.1007/978-3-031-12873-8\_7.
- [40] Coccochetti, G., Colasante, G., Rizzi, E. (2011). On the analysis of minimum thickness in circular masonry arches. Part I: State of the art and Heyman's solution. Part II: Present CCR solution. Part III: Milankovitch-type solution, *Applied Mechanics Reviews*, ASME, September 01, 2011, 64(5), Paper 050802 (Oct. 01, 2012), pp. 1-27. DOI: 10.1115/1.4007417.

- [41] Rizzi, E., Rusconi, F., Cocchetti, G. (2014). Analytical and numerical DDA analysis on the collapse mode of circular masonry arches, *Engineering Structures*, 60(February 2014), pp. 241-257. DOI: 10.1016/j.engstruct.2013.12.023.
- [42] Cocchetti, G., Rizzi, E. (2020). Analytical and numerical analysis on the collapse modes of least-thickness circular masonry arches at decreasing friction, *Frattura ed Integrità Strutturale - Fracture and Structural Integrity*, Special Issue on: Fracture and Damage Detection in Masonry Structures, 14(51), pp. 356-375, available Open Access at <https://www.fracturae.com/index.php/fis/article/view/2554>. DOI: 10.3221/IGF-ESIS.51.26.
- [43] Cocchetti, G., Rizzi, E. (2020). Non-linear programming numerical formulation to acquire limit self-standing conditions of circular masonry arches accounting for limited friction, *International Journal of Masonry Research and Innovation*, Special Issue on: 10IMC Masonry Research in the Third Millennium From Theory to Practical Applications, 5(4), pp. 569-617. DOI: 10.1504/IJMRI.2020.111806.
- [44] Cocchetti, G., Rizzi, E. (2020). Static upper/lower thrust and kinematic work balance stationarity for least-thickness circular masonry arch optimization, *Journal of Optimization Theory and Applications*, Special Issue on: Computational Optimization for Structural Engineering and Applications, 187(3), pp. 707-757, available Open Access at <https://link.springer.com/article/10.1007/s10957-020-01772-0>. DOI: 10.1007/s10957-020-01772-0.
- [45] Cocchetti, G., Rizzi, E. (2021). Least-thickness symmetric circular masonry arch of maximum horizontal thrust, *Archive of Applied Mechanics*, 91(6), pp. 2617-2639, available Open Access at <https://link.springer.com/article/10.1007/s00419-021-01909-1>. DOI: 10.1007/s00419-021-01909-1.
- [46] Cocchetti, G., Rizzi, E. (2024). Finite-friction least-thickness self-standing domains of symmetric circular masonry arches, *Structures*, Special Issue on Shells and Spatial Structures: Conceptual Design, Construction and Maintenance, Accepted 19 June 2024, Published online 8 July 2024, 66(August 2024), Paper 106800, pp. 1-20, available Open Access at <https://www.sciencedirect.com/science/article/pii/S2352012424009524>. DOI: 10.1016/j.istruc.2024.106800.
- [47] Cocchetti, G., Rizzi, E. (2025). Finite-friction least-thickness self-standing domains of symmetric circular masonry arches. Part II: Milankovitch-like self-weight distribution, *Structures*, ISTRUC\_108780, Accepted 25 March 2025, Published online 15 April 2025, 76(June 2025), Paper 108780, pp. 1-20, available Open Access at <https://www.sciencedirect.com/science/article/pii/S2352012425005946>. DOI: 10.1016/j.istruc.2025.108780.

## Tables and Figures

|                  | Triple point T               | Shift point S                | Junction point J             | Border point B               |
|------------------|------------------------------|------------------------------|------------------------------|------------------------------|
| $\mu$            | 1.277021363435198            | 1.537913842804308            | 1.546270800988722            | 1.853774888450581            |
| $\varphi$        | 51.94°                       | 56.97°                       | 57.11°                       | 61.66°                       |
| $\alpha$         | 2.430069103769349<br>139.23° | 2.531269027051532<br>145.03° | 2.534077907926731<br>145.19° | 2.623074865083552<br>150.29° |
| $A$              | 0.9029452397179642           | 0.7973524943847578           | 0.7943269204166809           | 0.6957132834961226           |
| $\eta$           | 0.6183182410743234           | 0.8734660698200911           | 0.8872221963291937           | 2                            |
| $h$              | 0.1147600824797408           | 0.08555323265580011          | 0.08479836323759743          | 0.06248908922171235          |
| $\hat{h}=\eta h$ | 0.07095825234441760          | 0.07472784588826560          | 0.07523499007678195          | 0.1249781784434247           |
| $\beta_r$        | 1.042556808593599<br>59.73°  | 0.2797031945436853<br>16.03° | 0<br>0°                      | 0<br>0°                      |
| $\beta_s$        | 0.3187321853045027<br>18.26° | 0.2797031945436853<br>16.03° | 0.2785814079040845<br>15.96° | 0.2420417380328302<br>13.87° |

Table 1: Characteristic data of marked landmark points.

|                             | low asymptote limit                      | top asymptote Limit          |
|-----------------------------|--|------------------------------|
| $\alpha$                    | 2.590843443008955<br>148.44°             | 2.648388899151005<br>151.74° |
| $A = \alpha \cot(\alpha/2)$ | $\sqrt{3} - 1$<br>0.7320508075688773     | 2/3<br>0.6                   |
| $\eta$                      | $2(2\sqrt{3} - 3)$<br>0.9282032302755092 | 2                            |

Table 2: Characteristic data of limit points for purely-overturning modes at  $\mu \rightarrow \infty$  ( $\varphi = 90^\circ$ ), with  $h = \hat{h} = 0$ ,  $\beta_r = 0$  and undefined  $\beta_s$ .

| arch state | $\eta$  | $\mu$   | $\varphi = \text{atan } \mu$ | $\alpha$ | $\beta_r$ | $\beta_s$ |
|------------|---------|---------|------------------------------|----------|-----------|-----------|
| SAFE       | 0.5     | 1.0     | 45°                          | 100°     | -         | -         |
| SR         | 0.5     | 1.0     | 45°                          | 130.09°  | 63.27°    | -         |
| PS         | 0.5     | 0.42127 | 22.84°                       | 100°     | -         | 28.04°    |
| PR         | 0.16074 | 1.0     | 45°                          | 100°     | 58.43°    | -         |

Table 3: Characteristic data of arch instances with reference state  $\eta = 0.5$ ,  $\mu = 1.0$  ( $\varphi = 45^\circ$ ) leading to mixed SR collapse for  $\alpha \simeq 130^\circ$ . Analytical maps in Figs. 13-14; arch illustrations in Fig. 15.

| arch state | $\eta$  | $\mu$   | $\varphi = \text{atan } \mu$ | $\alpha$ | $\beta_r$ | $\beta_s$ |
|------------|---------|---------|------------------------------|----------|-----------|-----------|
| SAFE       | 0.8     | 1.8     | $\simeq 61^\circ$            | 100°     | -         | -         |
| RS         | 0.8     | 1.8     | $\simeq 61^\circ$            | 144.74°  | 41.21°    | 14.20°    |
| PS         | 0.8     | 0.42127 | 22.84°                       | 100°     | -         | 28.04°    |
| PR         | 0.16074 | 1.8     | $\simeq 61^\circ$            | 100°     | 58.43°    | -         |

Table 4: Characteristic data of arch instances with reference state  $\eta = 0.8$ ,  $\mu = 1.8$  ( $\varphi \simeq 61^\circ$ ) leading to mixed RS collapse for  $\alpha \simeq 145^\circ$ . Analytical maps in Figs. 13-14; arch illustrations in Fig. 16.

|                  | max $\hat{h}$ (is)           | max $\hat{h}$ (ss)           |
|------------------|------------------------------|------------------------------|
| $\mu$            | 0.5374169122654898           | 0.8448805850502447           |
| $\varphi$        | 28.25°                       | 40.19°                       |
| $\alpha$         | 1.892939344622703<br>108.46° | 2.119284332007852<br>121.43° |
| $A$              | 1.363789142268194            | 1.188653541064082            |
| $\eta$           | 0.3435759819418909           |                              |
| $h$              | 0.3268619493013732           |                              |
| $\hat{h}=\eta h$ | 0.1123019151906599           |                              |
| $\beta_r$        | 1.115492876804752<br>63.91°  |                              |
| $\beta_s$        | 0.4690663230293556<br>26.88° | -                            |

Table 5: Characteristic data of marked  $\hat{h}$  stationary points.

|                  | max $\beta_s$ (is)   | max $\beta_r$ (is)           | max $\beta_r$ (ss)           |
|------------------|--|------------------------------|------------------------------|
| $\mu$            | $\frac{\cos 0.5 - \sin 0.5}{\cos 0.5 + \sin 0.5} = 0.2934079930260234$ | 0.6379887277366990           | 0.9341739608482718           |
| $\varphi$        | 16.35°   | 32.54°                       | 43.05°                       |
| $\alpha$         | 1.542786942738411<br>88.40°  | 2.000761612520613<br>114.64° | 2.196404448812124<br>125.84° |
| $A$              | 1.586616134532187  | 1.283598498669179            | 1.122875901494054            |
| $\eta$           | 0.1876217060660825   | 0.3975610062458916           |                              |
| $h$              | 0.5  | 0.2777076435564899           |                              |
| $\hat{h}=\eta h$ | 0.09381085303304123  | 0.1104057302144935           |                              |
| $\beta_r$        | 1.044555710615084<br>59.85°  | 1.119864231443752<br>64.16°  |                              |
| $\beta_s$        | 0.5<br>28.65°  | 0.4478684050776427<br>25.66° | -                            |

Table 6: Characteristic data of marked  $\beta_{s,r}$  stationary points.

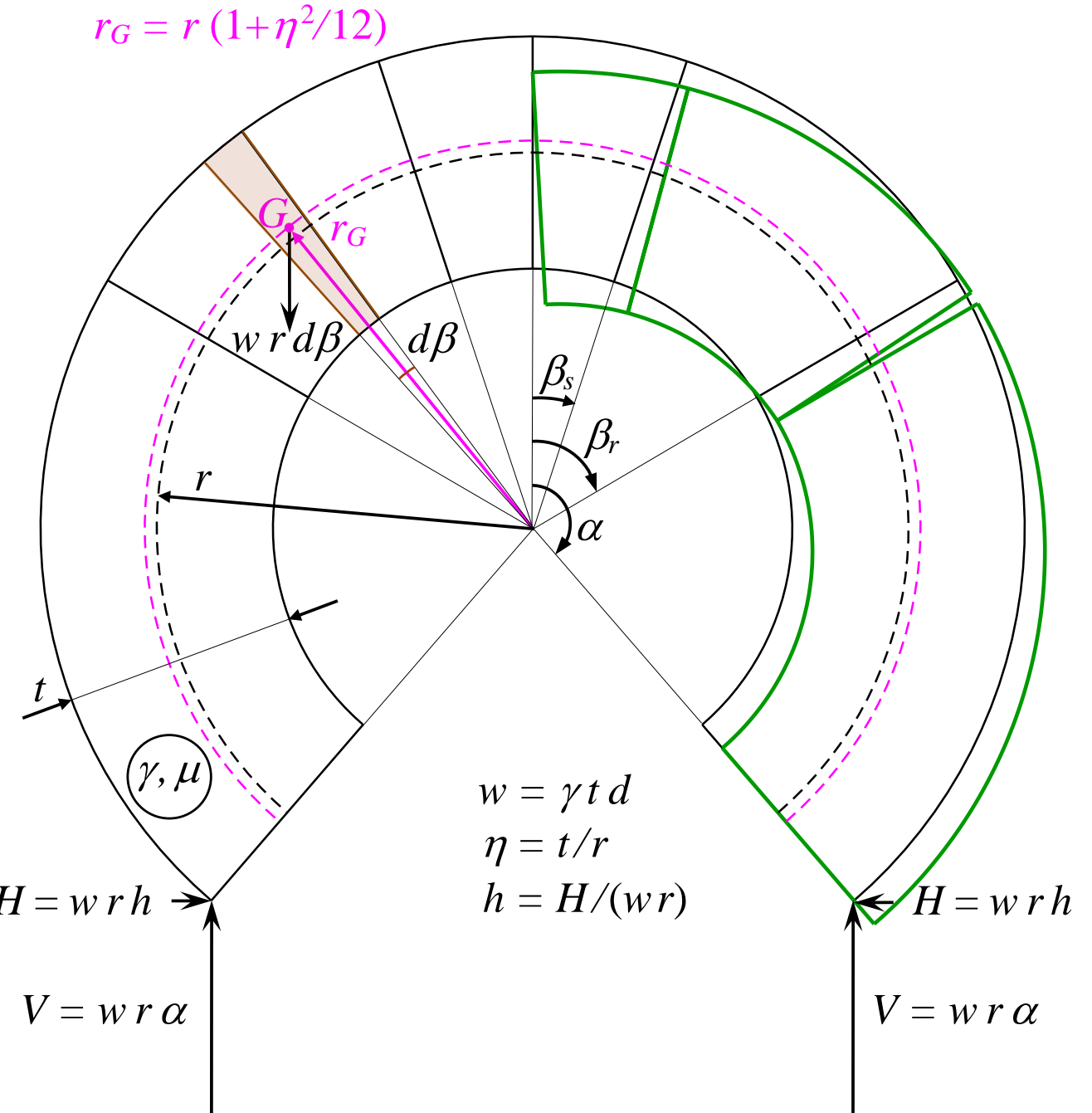


Figure 1: Analytical sketch of a self-standing symmetric circular continuous masonry arch with inner radius  $r$ , thickness  $t$  (thickness-to-radius ratio  $\eta = t/r$ ), out-of-plane depth  $d$ , uniform specific weights per unit volume  $\gamma$  and per unit length of geometrical centreline of the arch  $w = \gamma t d$ , and inherent friction coefficient  $\mu$ , with indication of the various characteristic variables (horizontal shoulder reaction  $H$  opposite of horizontal thrust  $H$ , and non-dimensional horizontal thrust  $h = H/(wr)$ , vertical shoulder reaction  $V$  opposite of half-arch weight  $W = wr\alpha$ ; half-angle of embrace  $\alpha$ , sliding  $\beta_s$  and rotational  $\beta_r$  angular inner-joint positions from the crown). The plot specifically refers to the arch features for the overcomplete case of landmark “Triple point T”, displaying concomitant multiple (four) underlying collapse modes: Purely-Rotational, Purely-Sliding, mixed Rotational-Sliding, mixed Sliding-Rotational. The mixed Sliding-Rotational mechanism (of the half-arch) is selectively represented on the right. On the left, an infinitesimal arch element with real centroid  $G$ , for true Milankovitch-like uniform self-weight distribution at radial distance  $r_G = r(1 + \eta^2/12)$ , versus classical approximate Heyman-like uniform self-weight distribution at radial distance  $r$ , is depicted.

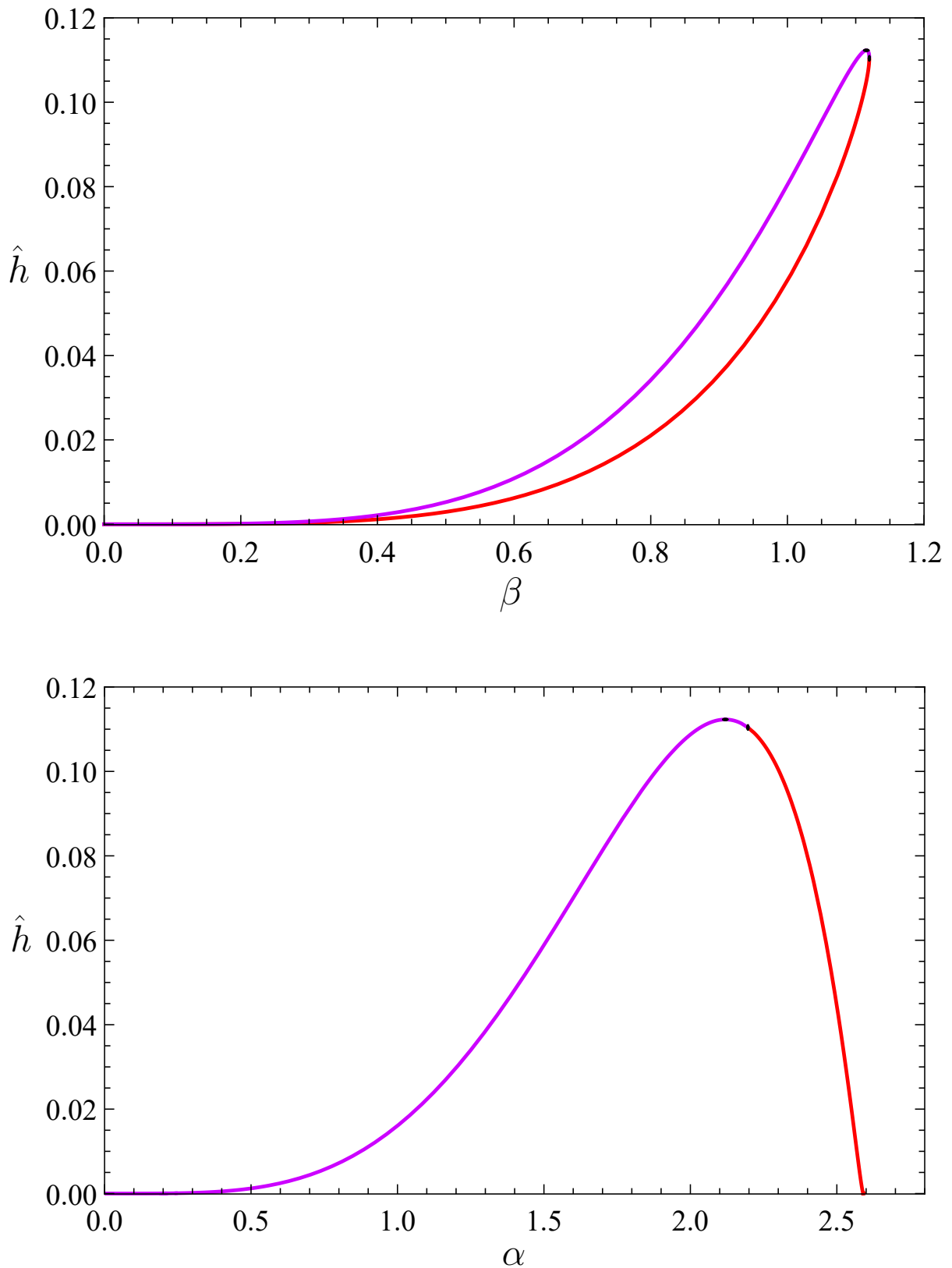


Figure 2: Purely-rotational trends  $\hat{h} = \eta h$  of  $\beta = \beta_r$  and of  $\alpha$ .

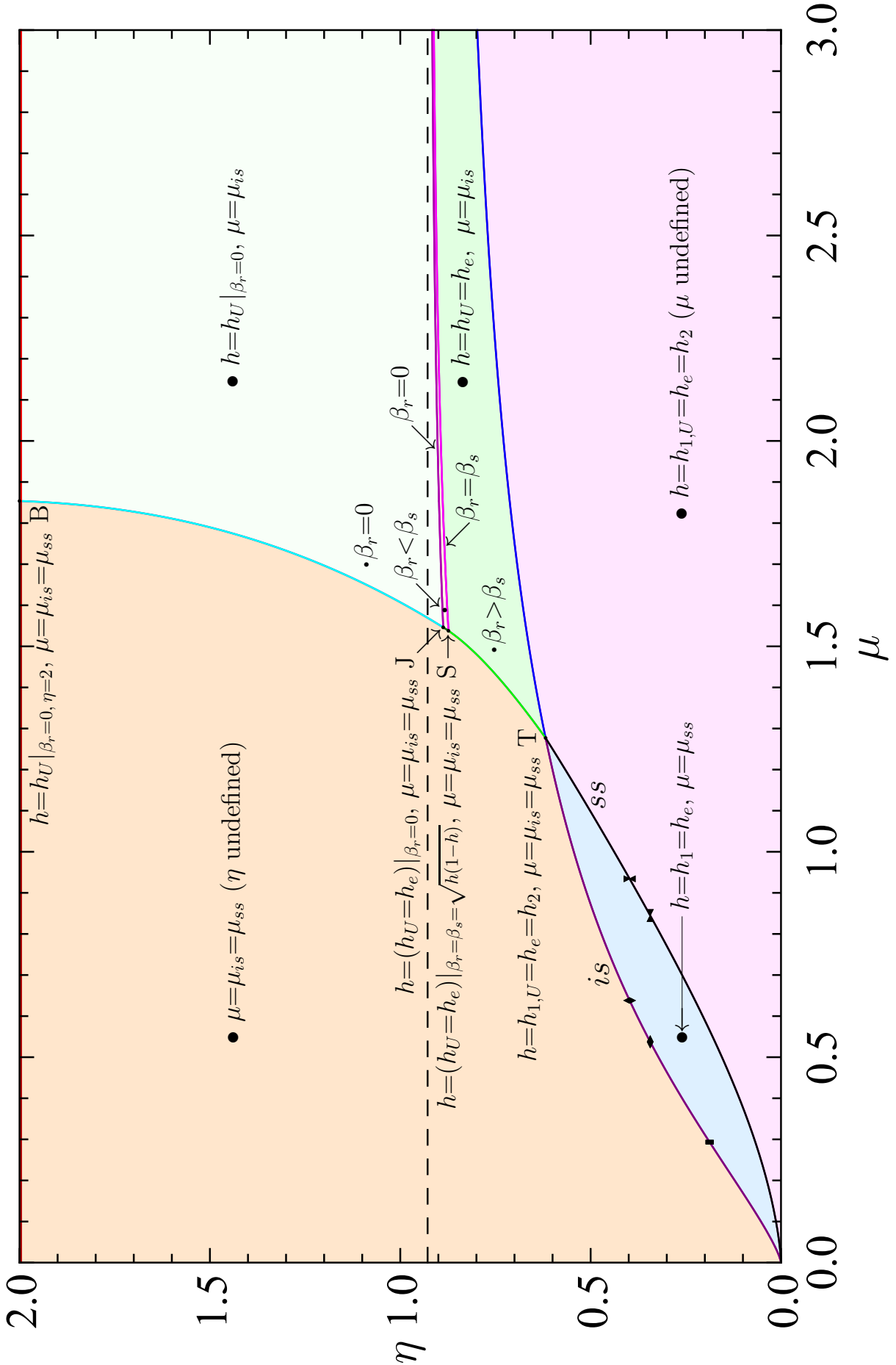


Figure 3: Analytical  $\eta$ - $\mu$  domain map of self-standing and collapse states.

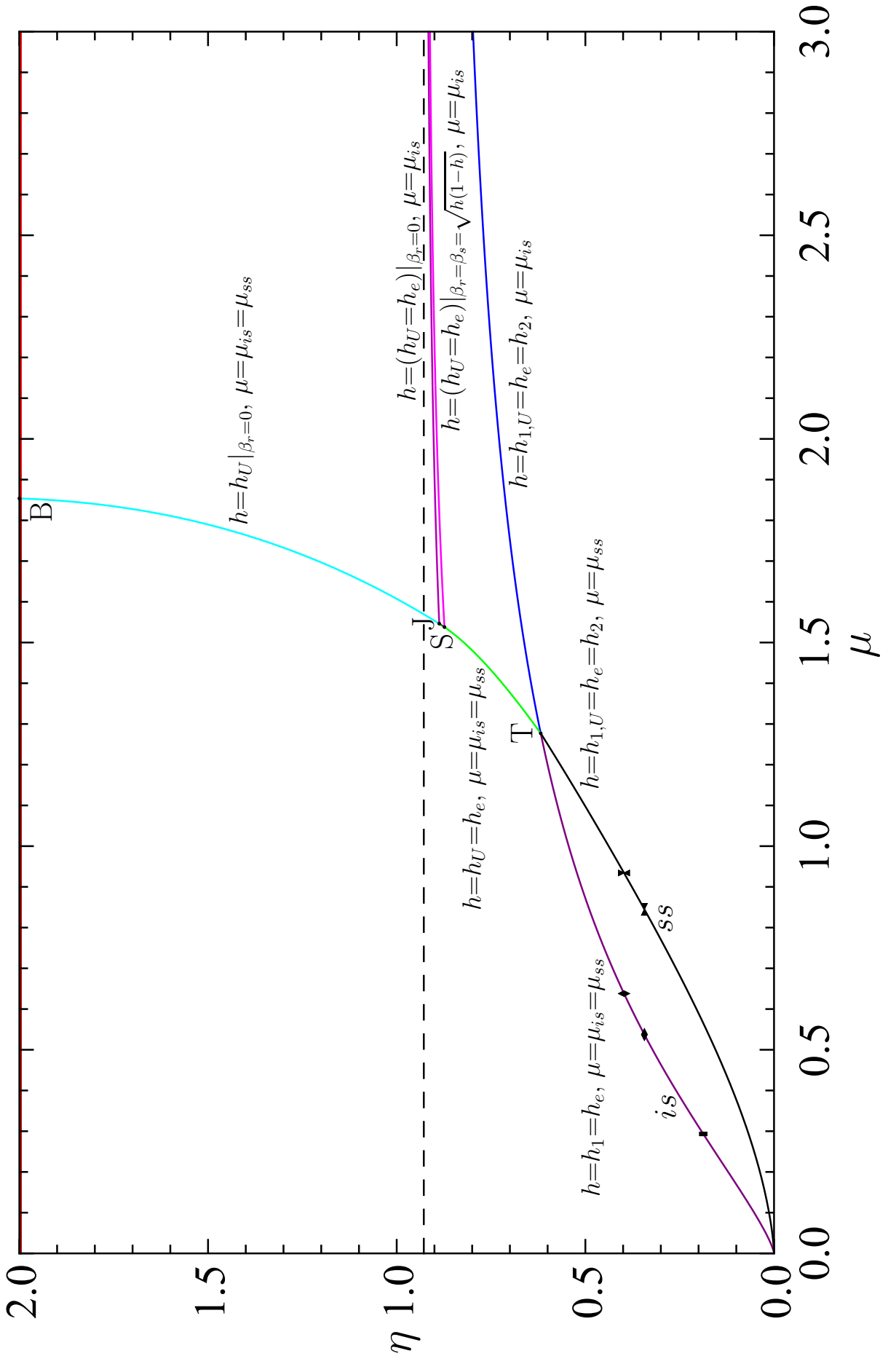


Figure 4: Analytical  $\eta$ - $\mu$  boundary map of self-standing and collapse states.

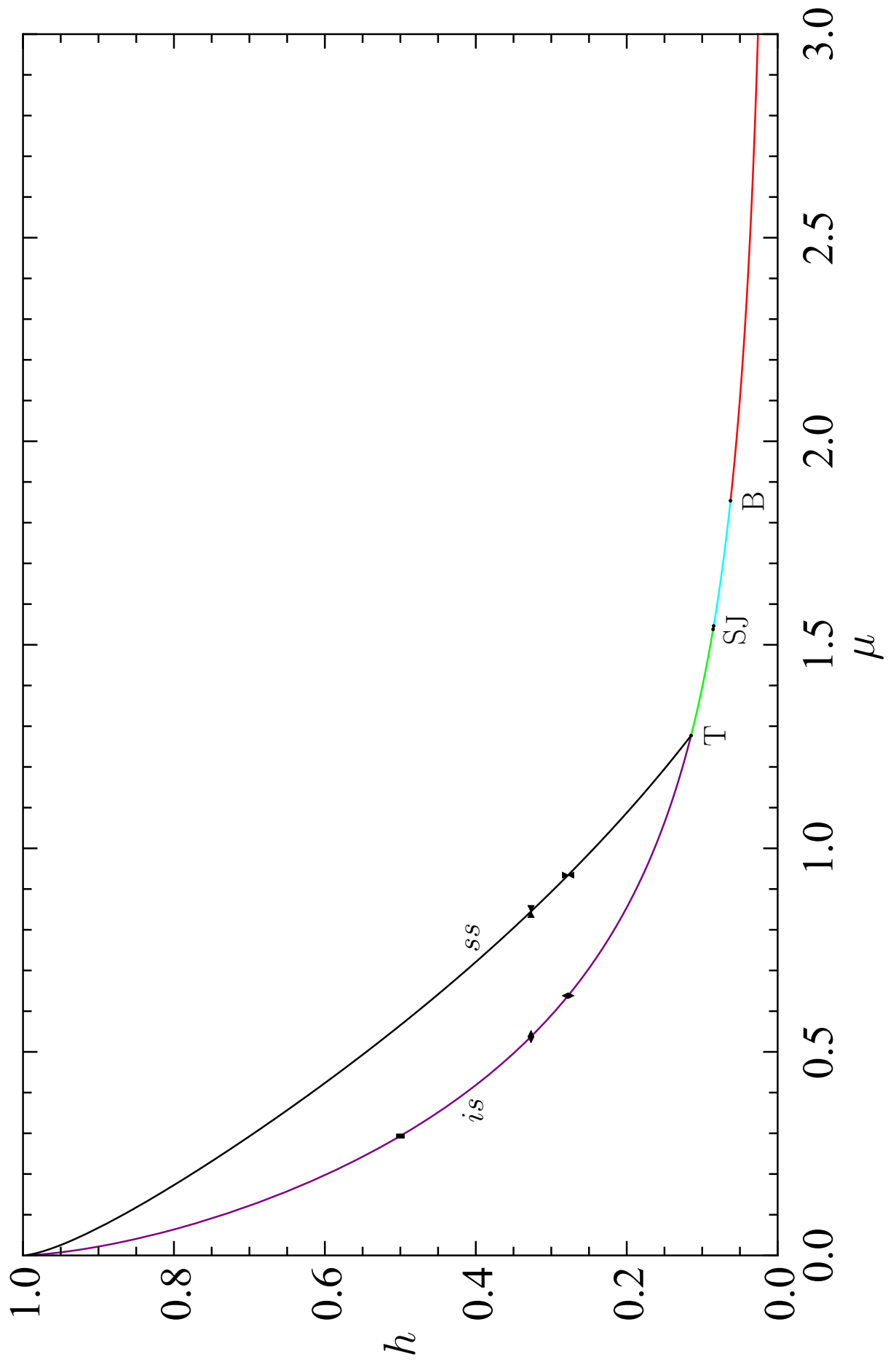


Figure 5: Analytical  $h$ - $\mu$  map of self-standing and collapse states.

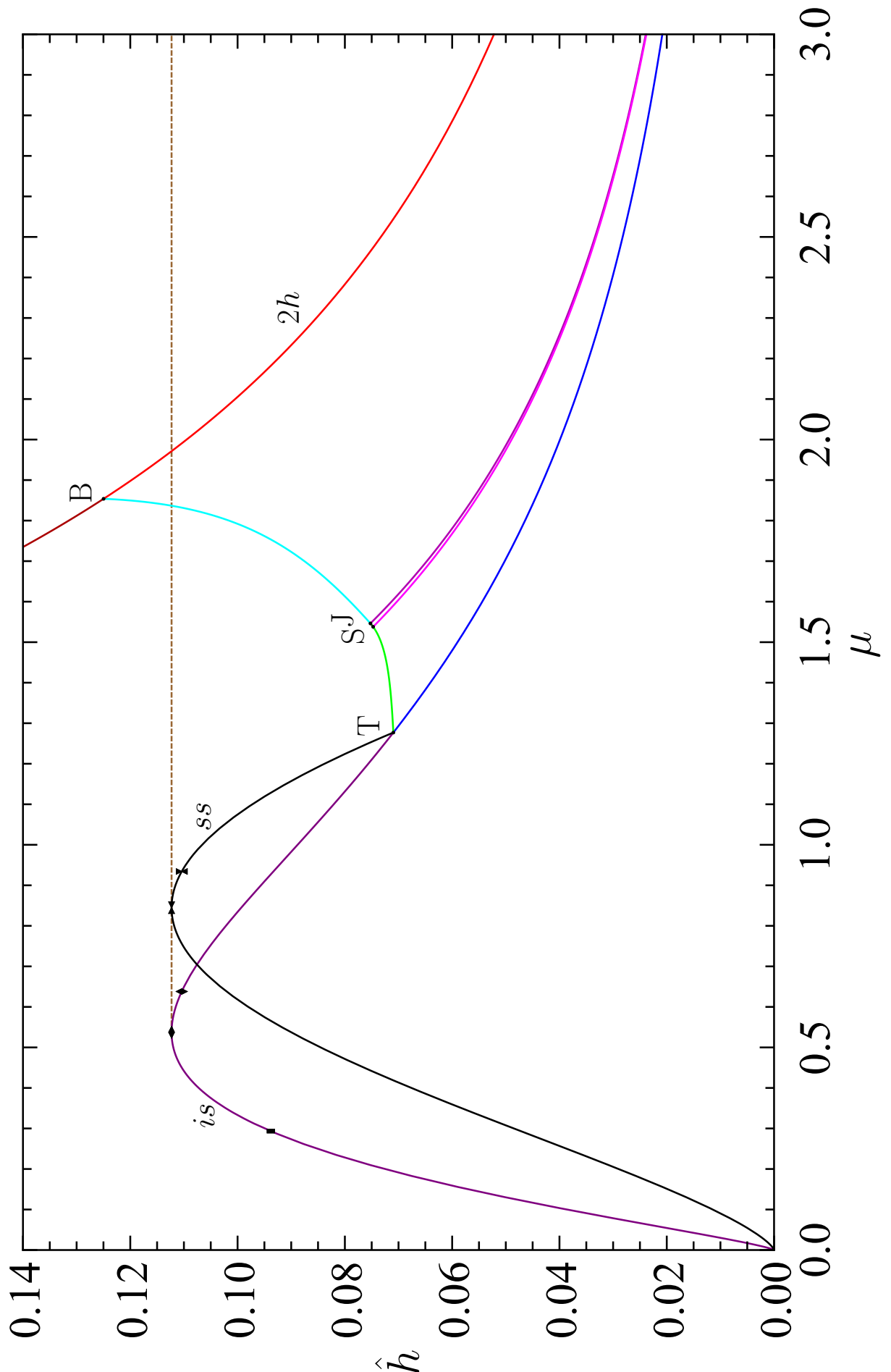


Figure 6: Analytical  $\hat{h}$ - $\mu$  map of self-standing and collapse states.

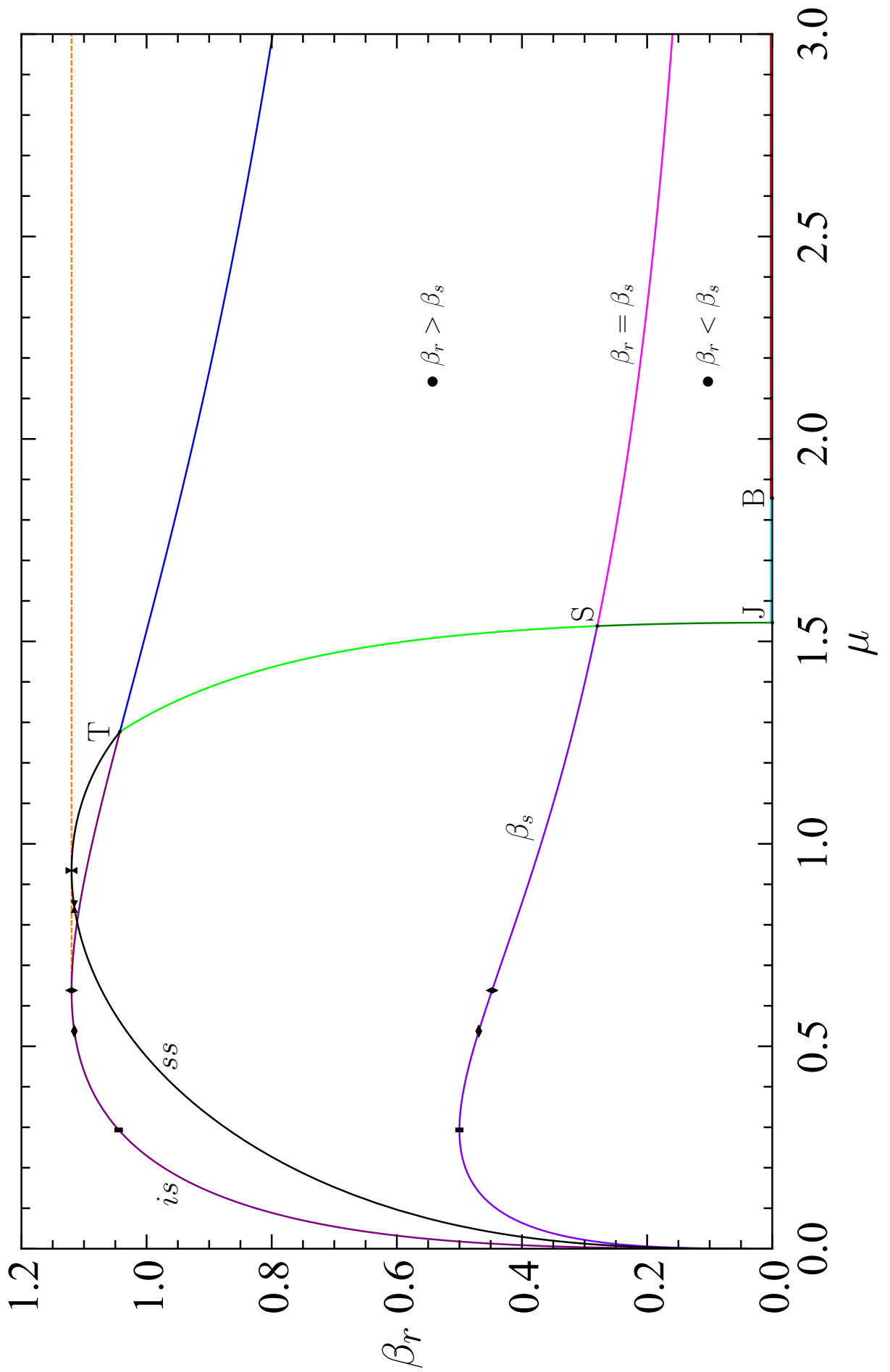


Figure 7: Analytical  $\beta$ - $\mu$  map of self-standing and collapse states.

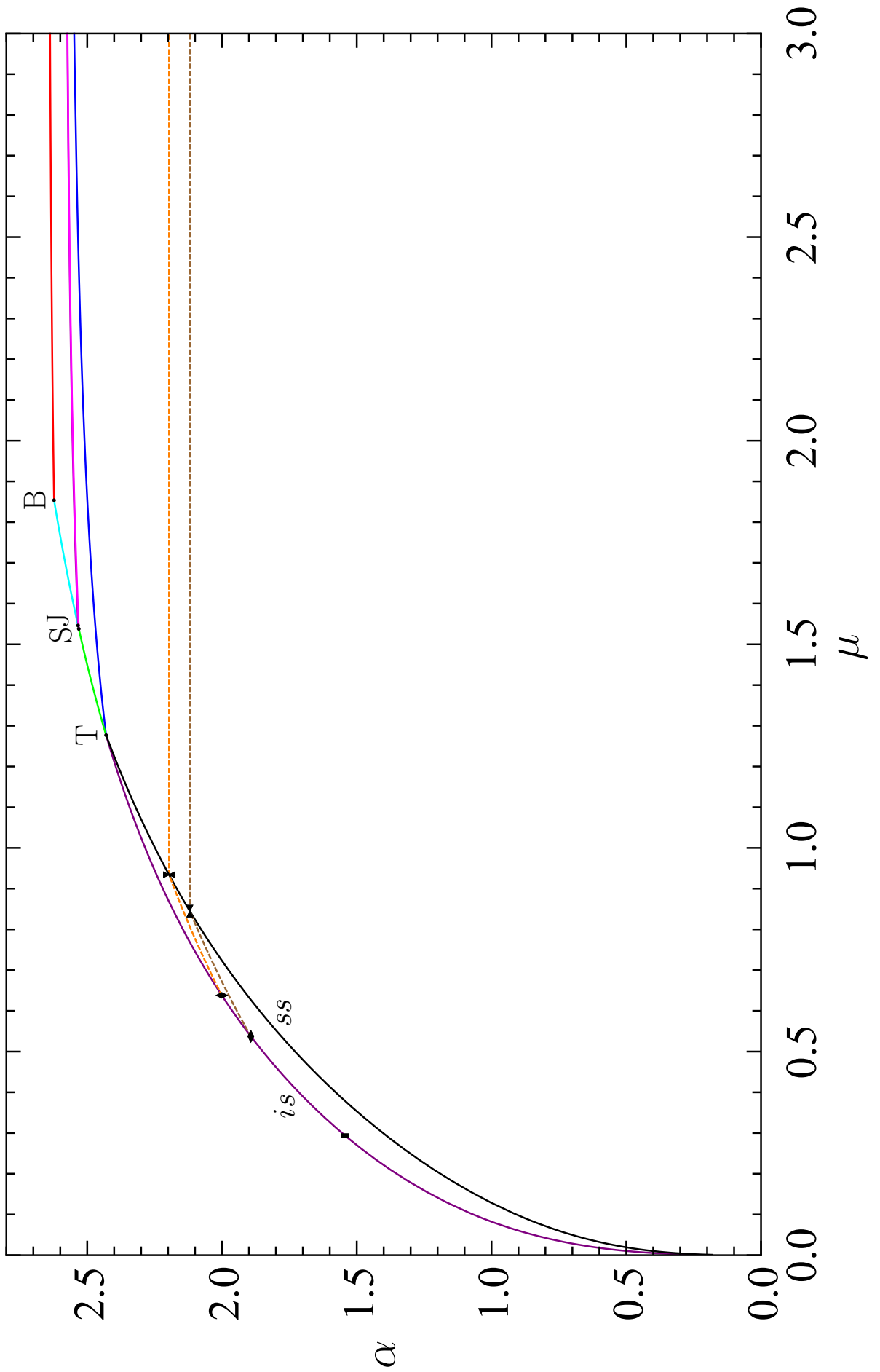


Figure 8: Analytical  $\alpha$ - $\mu$  map of self-standing and collapse states.

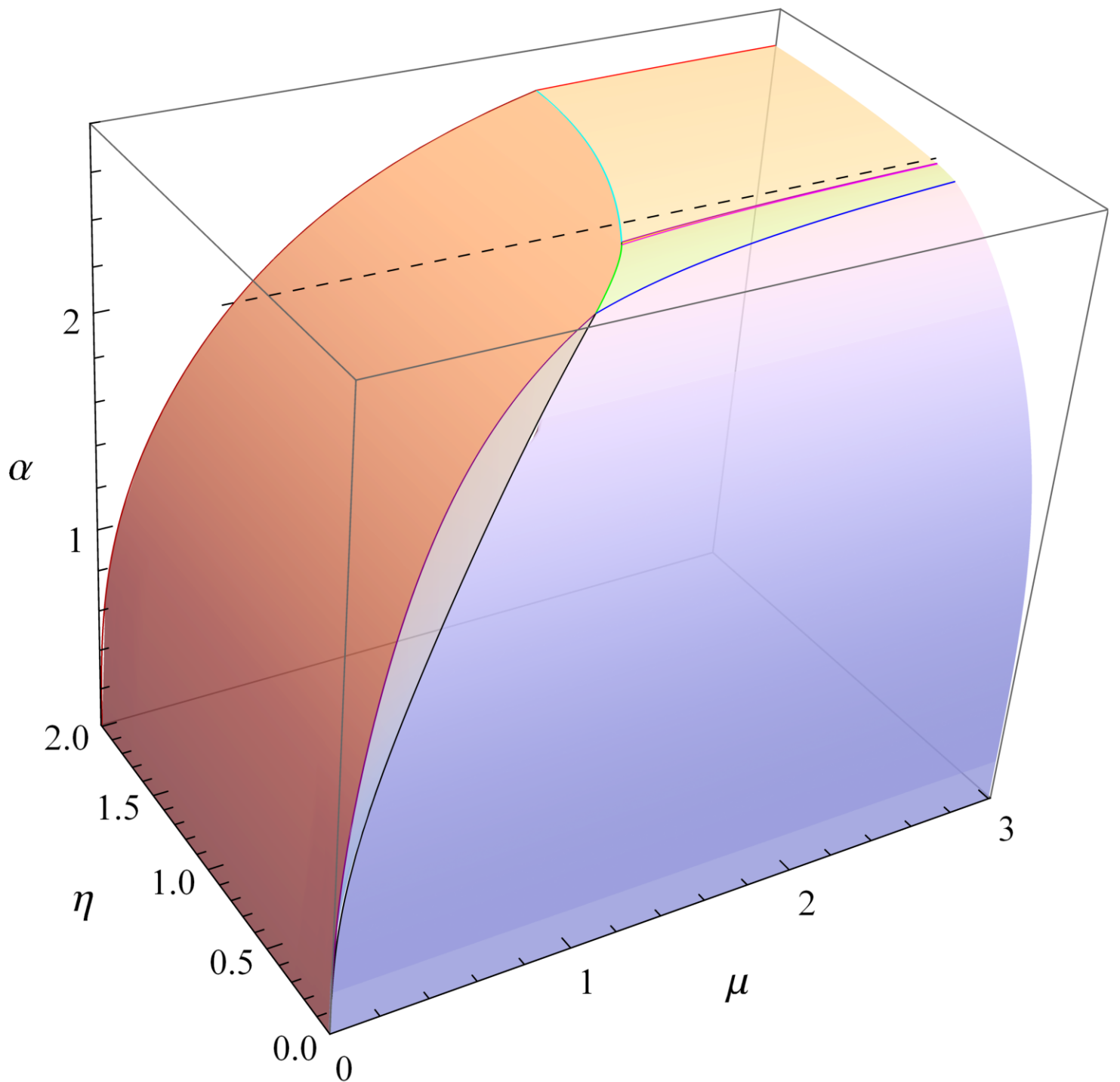


Figure 9: Three-dimensional surface representation of  $\eta; \mu, \alpha$  collapse states.

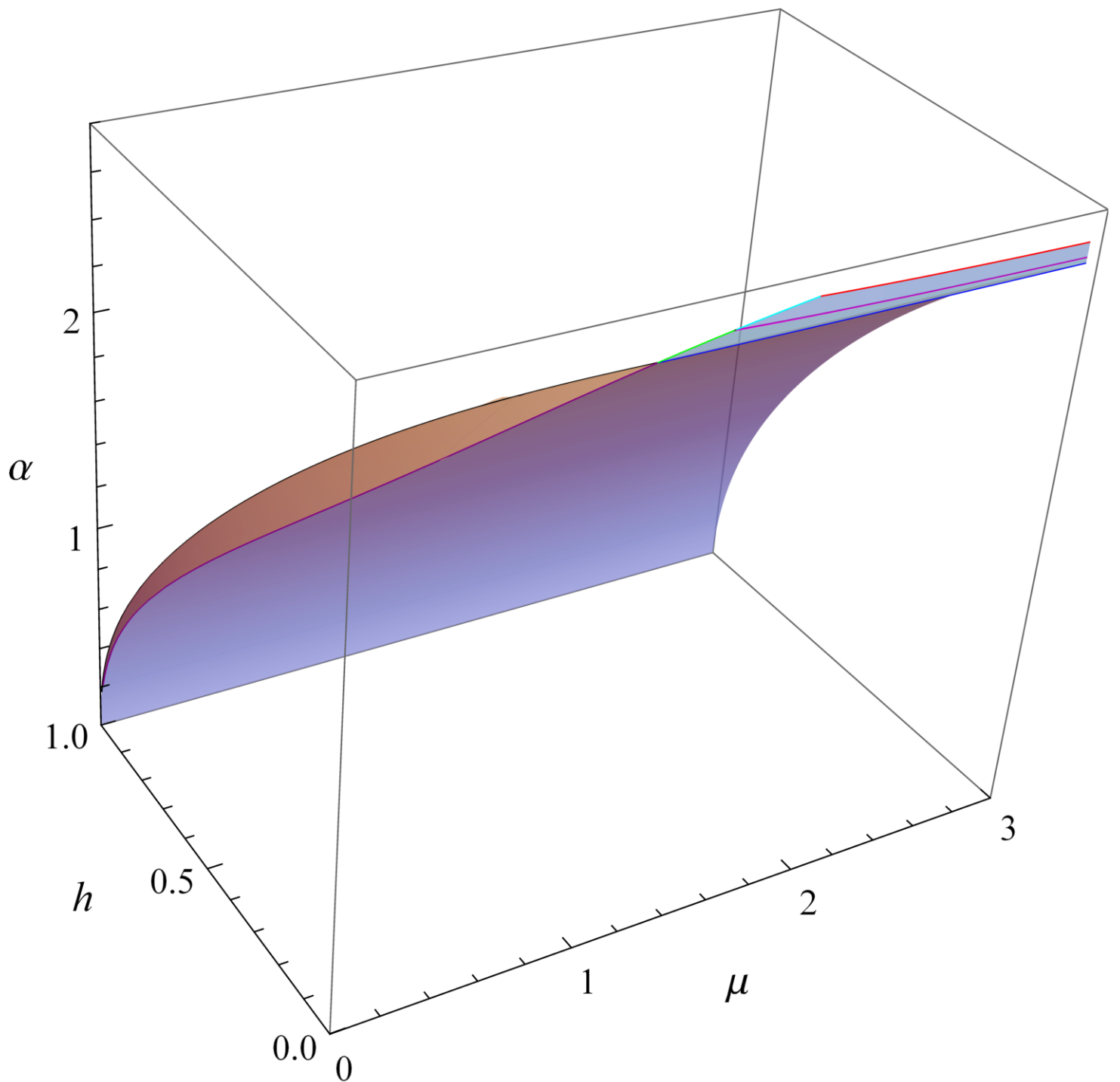


Figure 10: Three-dimensional surface representation of  $h; \mu, \alpha$  collapse states.

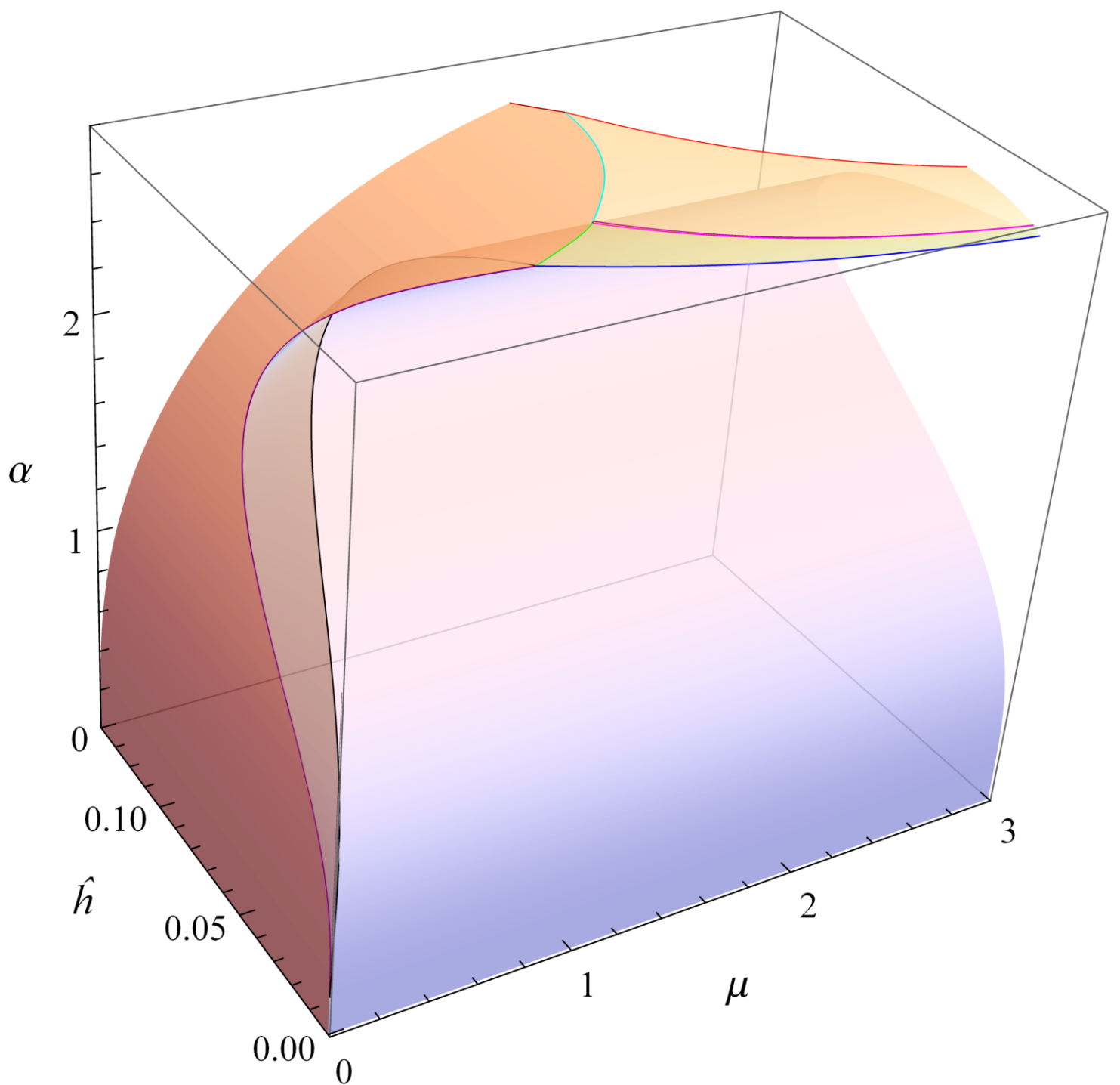


Figure 11: Three-dimensional surface representation of  $\hat{h}; \mu, \alpha$  collapse states.

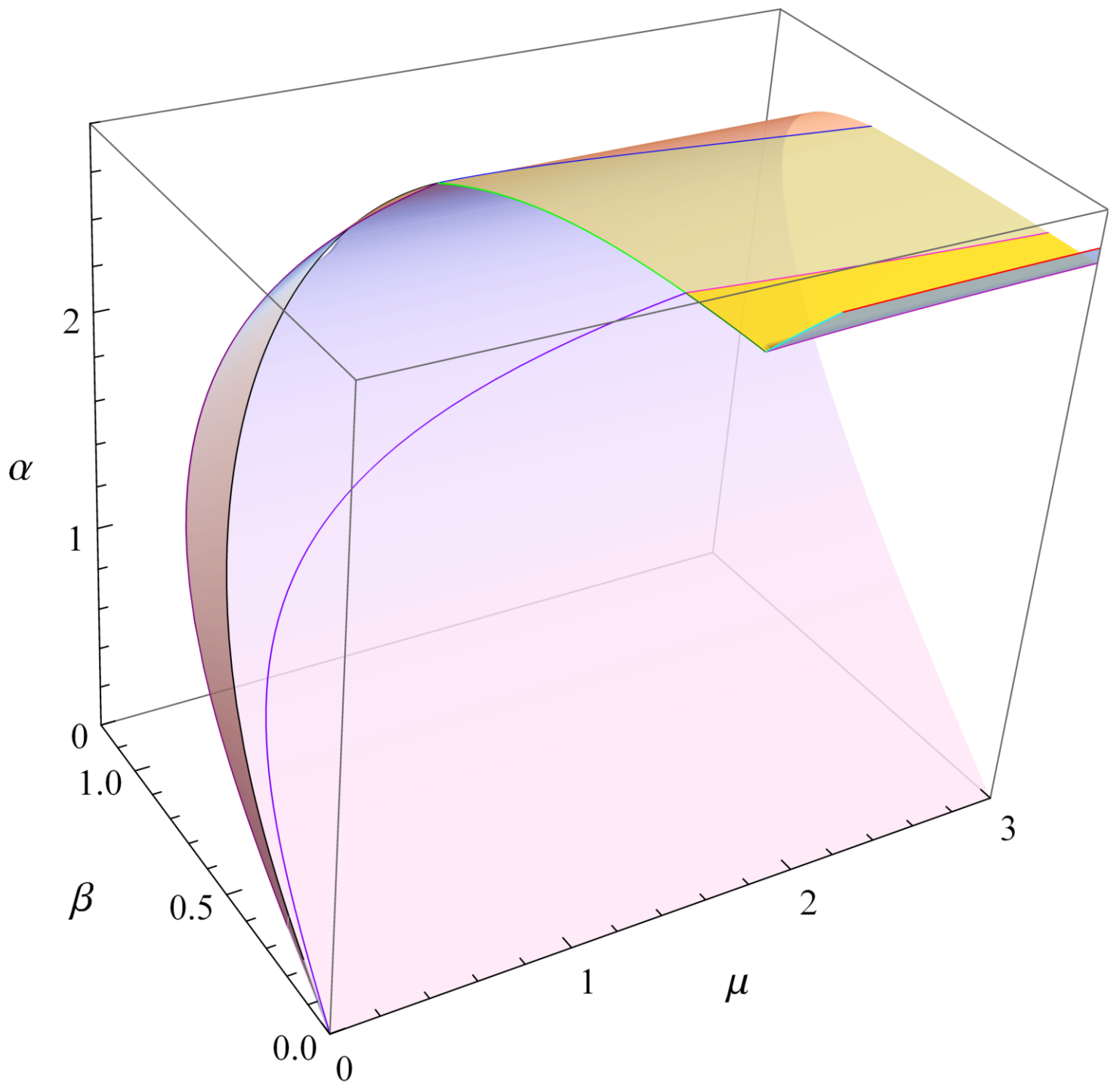


Figure 12: Three-dimensional surface representation of  $\beta_{r,s}; \mu, \alpha$  collapse states.

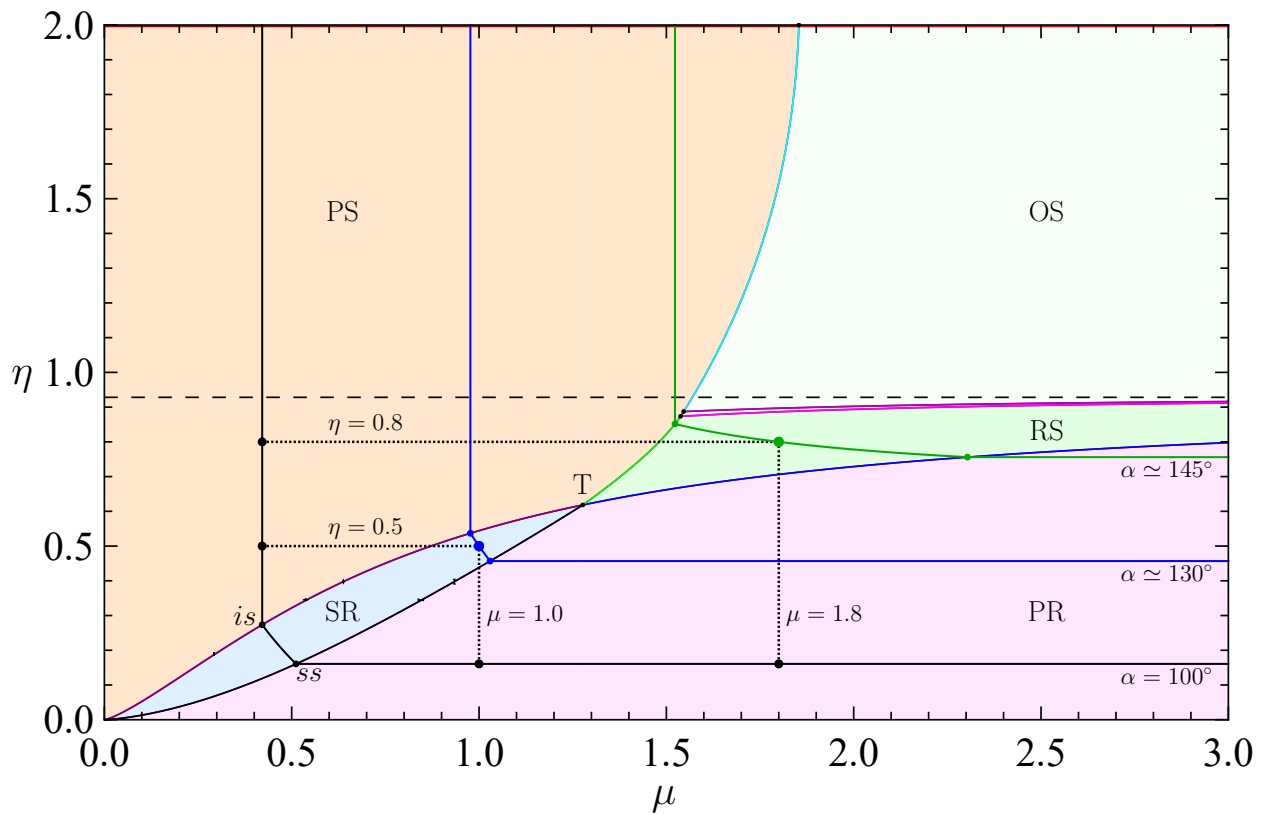


Figure 13: Particular arch instances in the  $(\eta, \mu)$  2D map. Characteristic values in Tables 3-4.

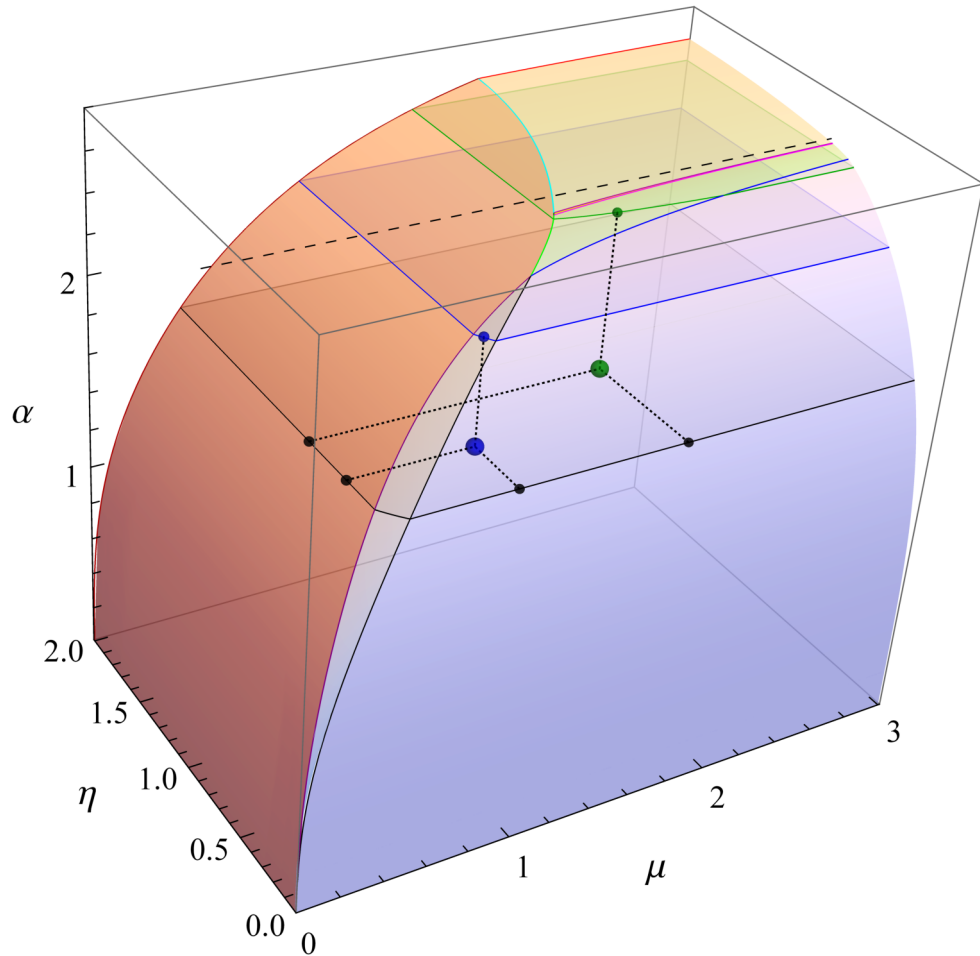
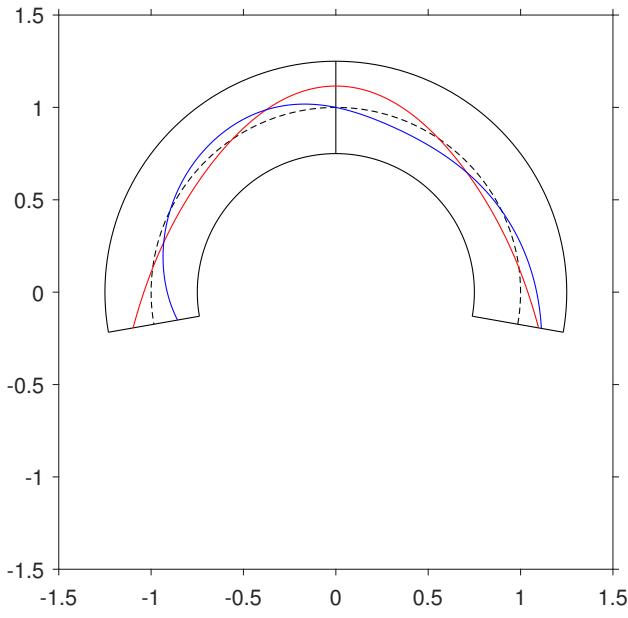
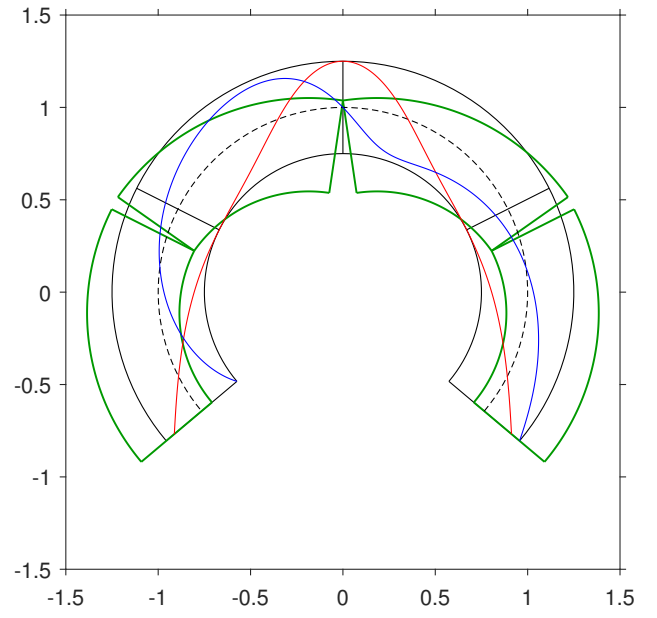


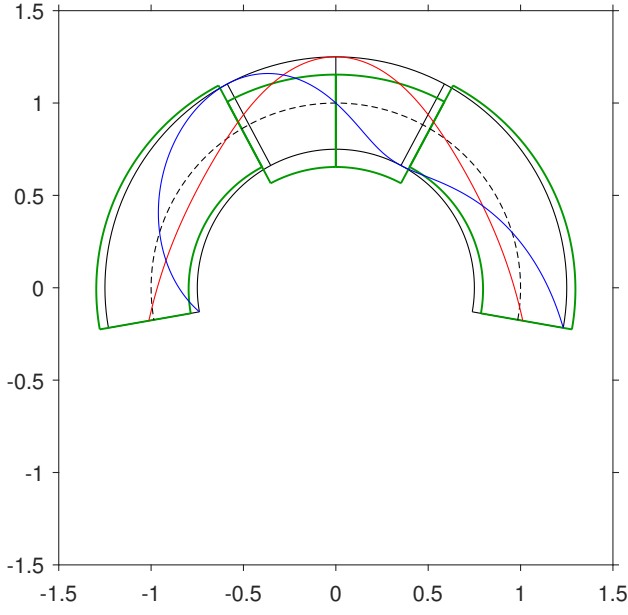
Figure 14: Particular arch instances in the  $(\eta, \mu, \alpha)$  3D map. Characteristic values in Tables 3-4.



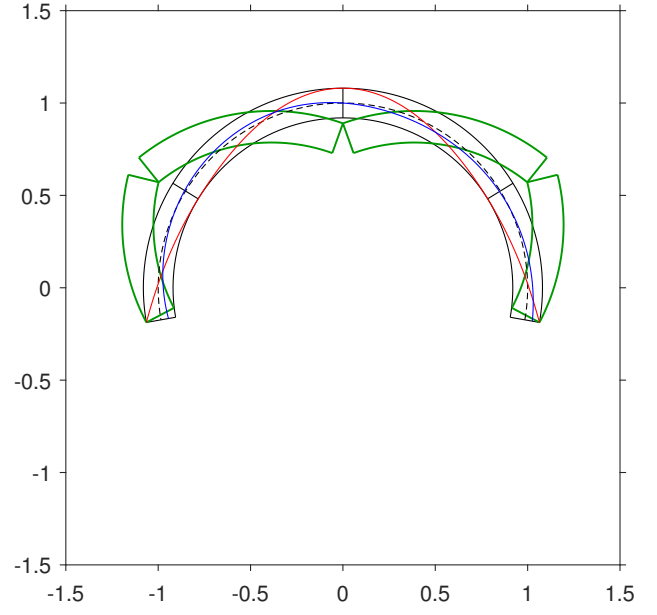
(a)



(b)

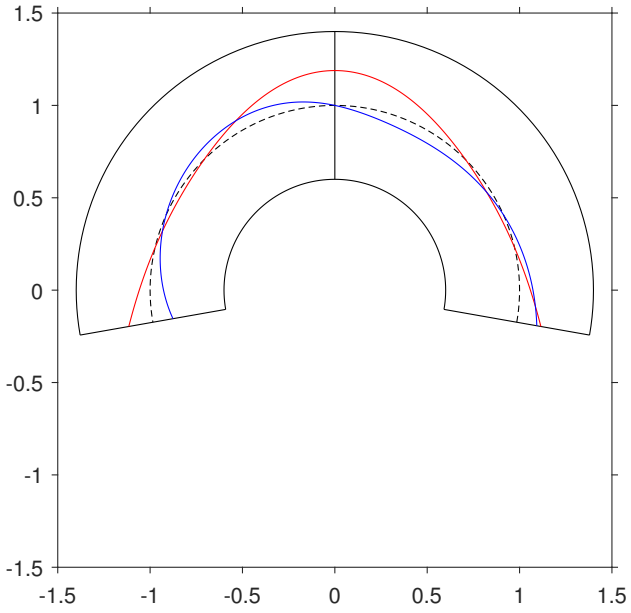


(c)

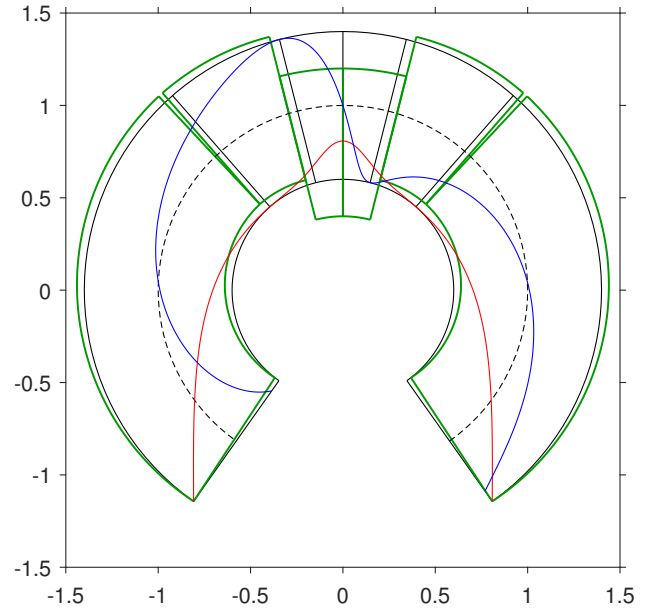


(d)

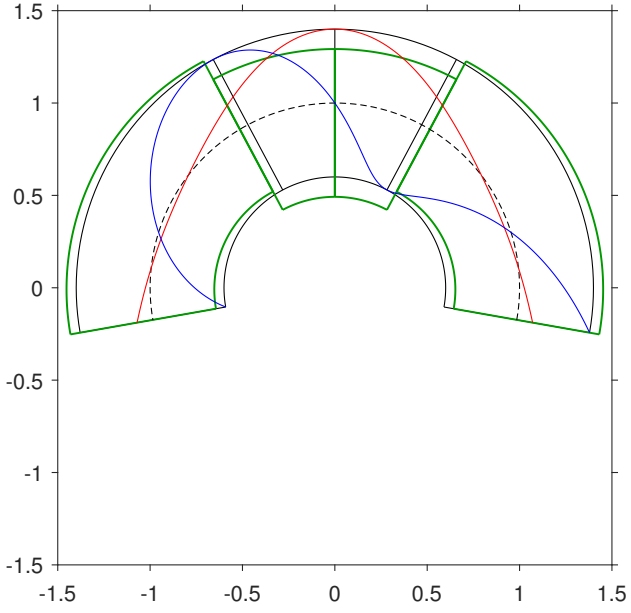
Figure 15: Arch reference configuration, with [line of thrust](#) and [line of friction](#), and possible [collapse mechanism](#). Reference state with  $\eta = 0.5$ ,  $\mu = 1.0$  ( $\varphi = 45^\circ$ ): (a) safe for  $\alpha = 100^\circ$ ; (b) mixed SR collapse for  $\alpha \approx 130^\circ$ ; (c) PS collapse with  $\eta = 0.5$ ,  $\mu = 0.42127$  and (d) PR collapse with  $\eta = 0.16074$ ,  $\mu = 1.0$  for  $\alpha = 100^\circ$ . Characteristic values in Table 3.



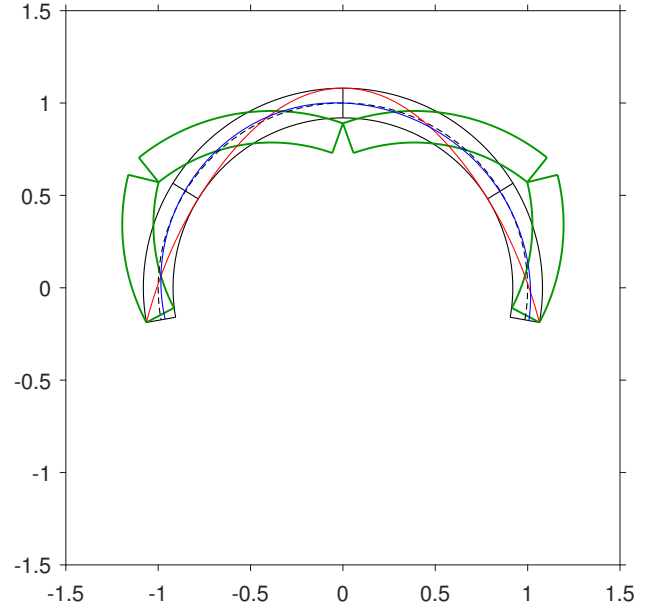
(a)



(b)



(c)



(d)

Figure 16: Arch reference configuration, with [line of thrust](#) and [line of friction](#), and possible [collapse mechanism](#). Reference state with  $\eta = 0.8$ ,  $\mu = 1.8$  ( $\varphi \approx 61^\circ$ ): (a) safe for  $\alpha = 100^\circ$ ; (b) mixed RS collapse for  $\alpha \approx 145^\circ$ ; (c) PS collapse with  $\eta = 0.8$ ,  $\mu = 0.42127$  and (d) PR collapse with  $\eta = 0.16074$ ,  $\mu = 1.8$  for  $\alpha = 100^\circ$ . Characteristic values in Table 4.

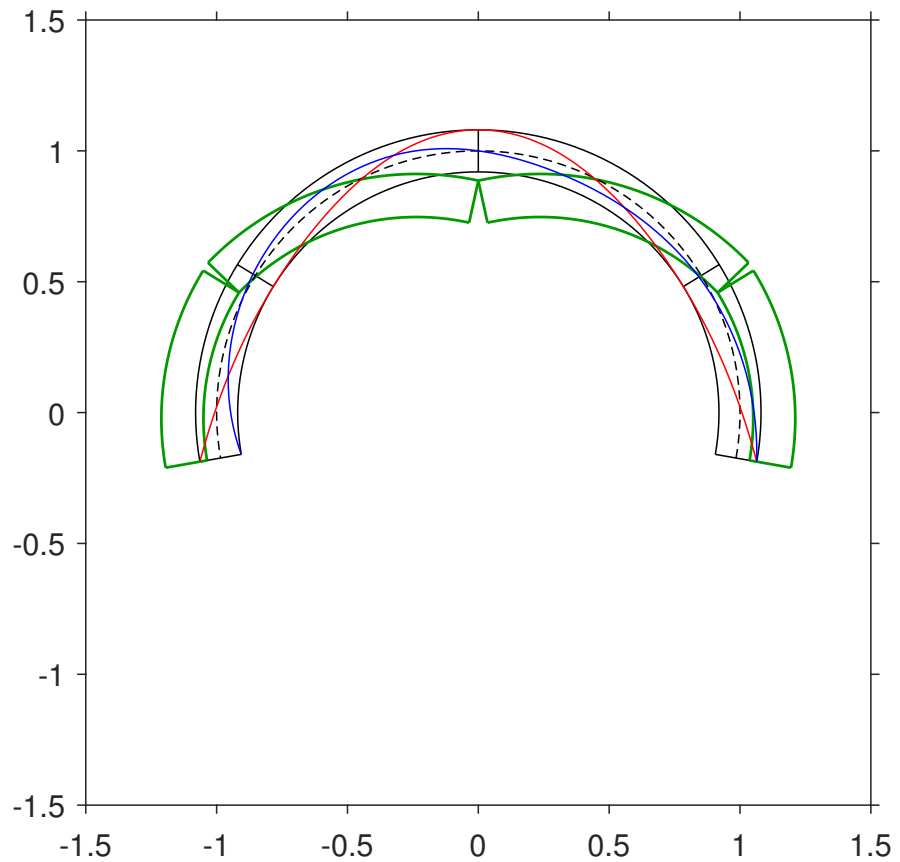
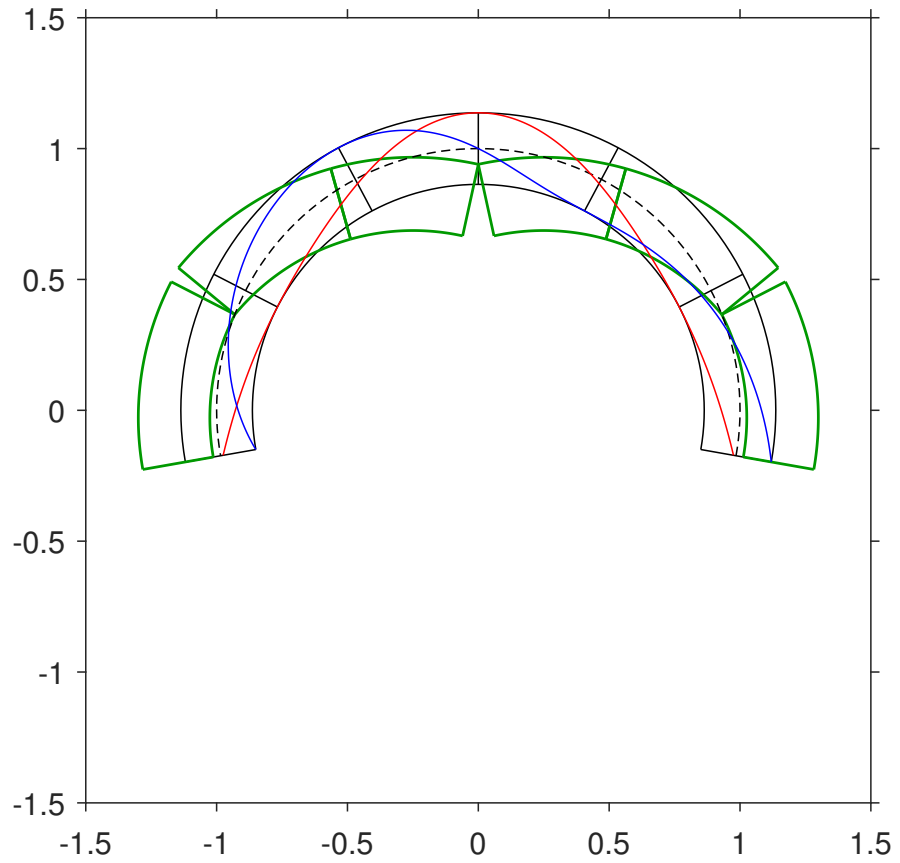


Figure 17: Least-thickness collapse mechanism, with line of thrust and line of friction at  $\alpha = 100^\circ$  for limiting mixed SR modes on inner/shoulder sliding activation boundaries with:  $\eta = 0.2734059247599199$ ,  $\mu = 0.4212673993052823$  ( $\varphi = 22.84^\circ$ ),  $\beta_r = 62.79^\circ$ ,  $\beta_s = 28.04^\circ$  (top);  $\eta = 0.1607356499776525$ ,  $\mu = 0.5117048672706682$  ( $\varphi = 27.10^\circ$ ),  $\beta_r = 58.43^\circ$  (low).

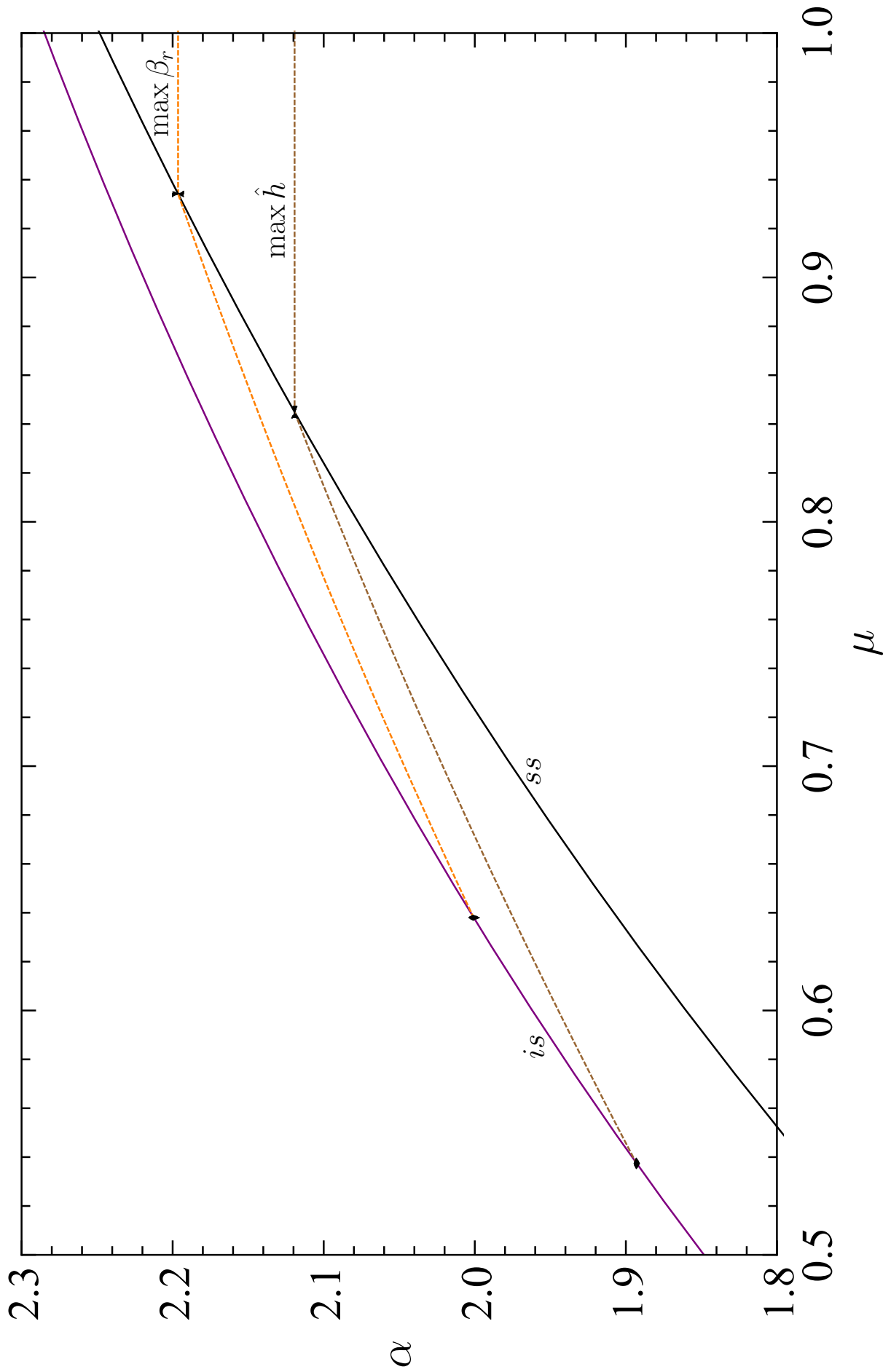


Figure 18: Zoom of analytical  $\alpha$ - $\mu$  map on  $\beta_r$  and  $\hat{h}$  stationary points.

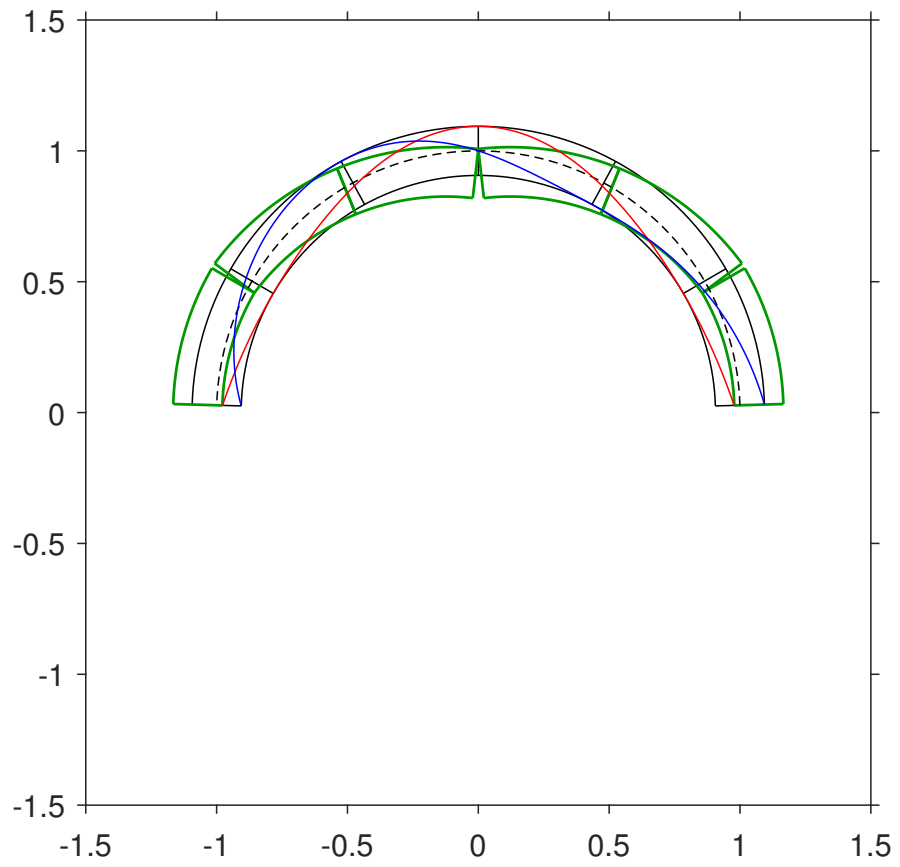
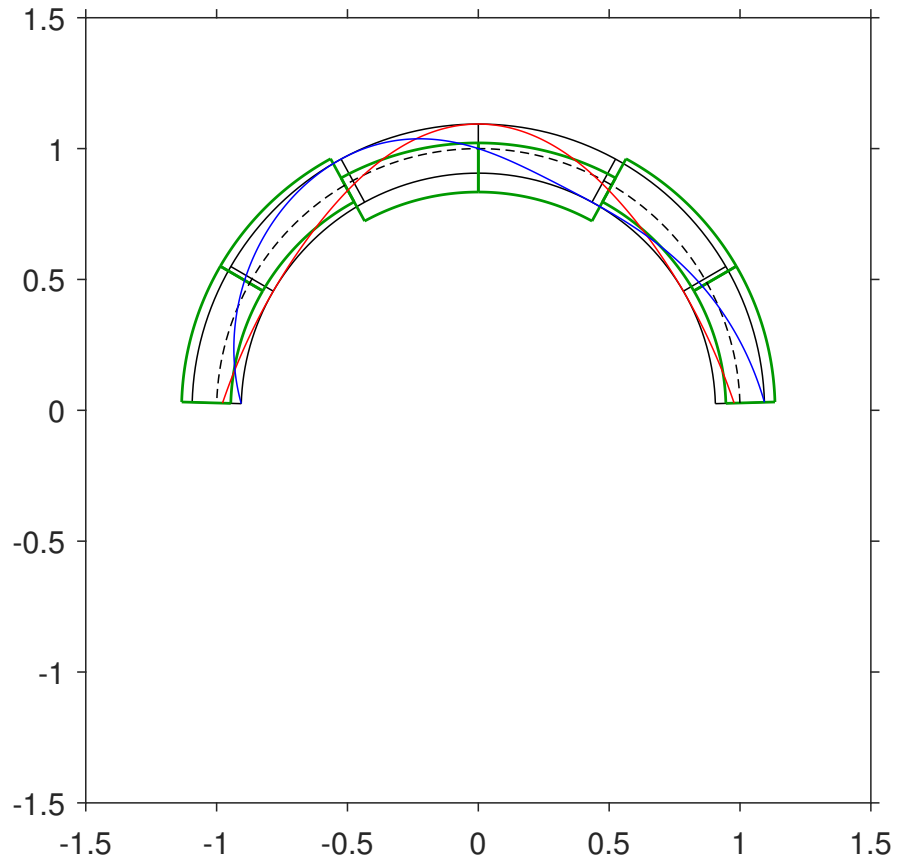


Figure 19: Least-thickness collapse mechanism, with line of thrust and line of friction at max  $\beta_s$  (is) with  $\mu = 0.2934079930260234$  ( $\varphi \simeq 16.35^\circ$ ),  $\alpha = 1.542786942738411 \simeq 88.40^\circ$ ,  $\beta_r = 1.044555710615084 \simeq 59.85^\circ$ ,  $\beta_s = 1/2 = 0.5 \simeq 28.65^\circ$ ,  $\eta = 0.1876217060660825$ ,  $\hat{h} = 0.09381085303304123$ : purely-sliding (top); sliding-rotational (low).

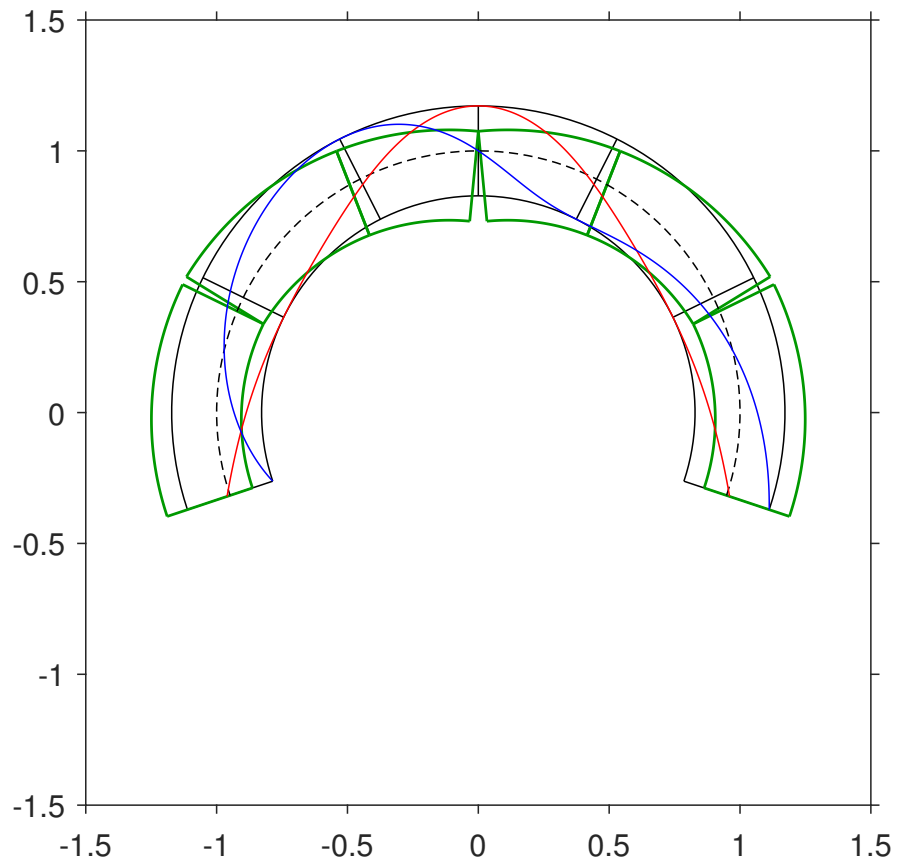
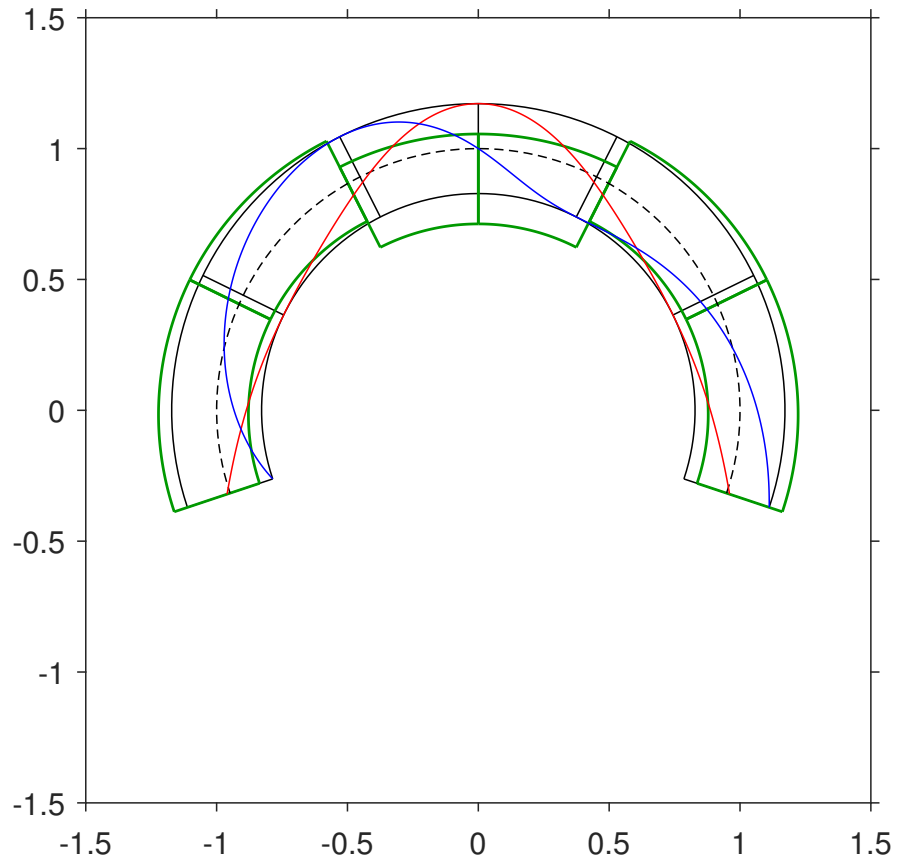


Figure 20: Least-thickness collapse mechanism, with line of thrust and line of friction at max  $\hat{h}$  ( $is$ ) with  $\mu = 0.5374169122654898$  ( $\varphi \simeq 28.25^\circ$ ),  $\alpha = 1.892939344622703 \simeq 108.46^\circ$ ,  $\beta_r = 1.115492876804752 \simeq 63.91^\circ$ ,  $\beta_s = 0.4690663230293556 \simeq 26.88^\circ$ ,  $\eta = 0.3435759819418909$ ,  $\hat{h} = 0.1123019151906599$ : purely-sliding (top); sliding-rotational (low).

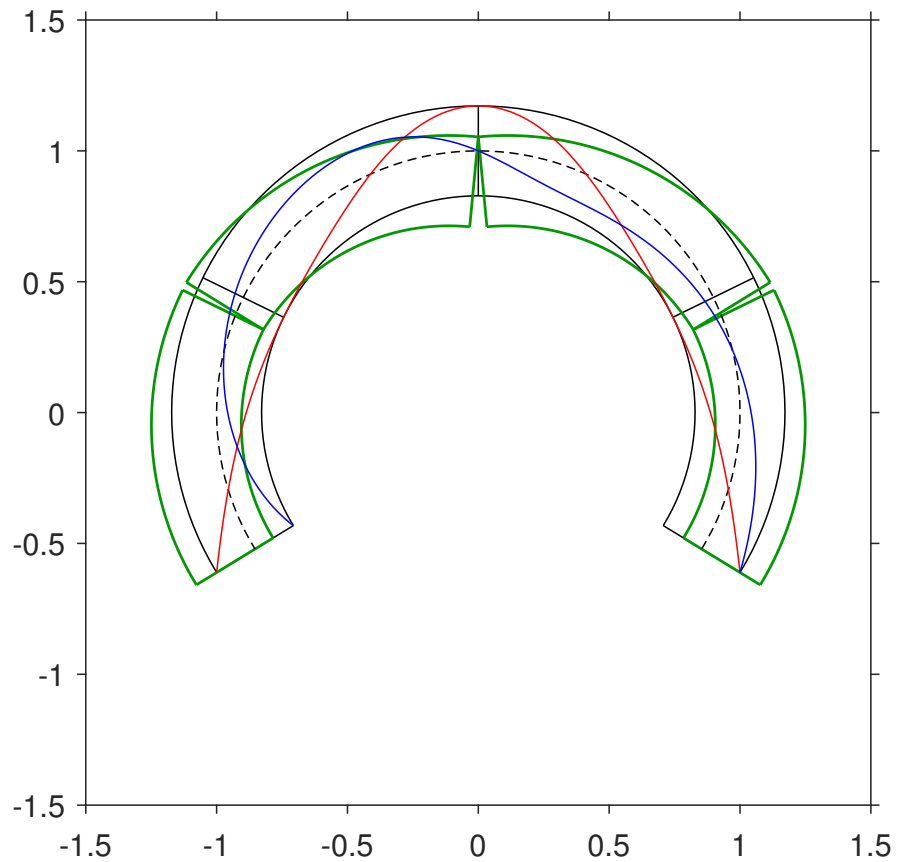
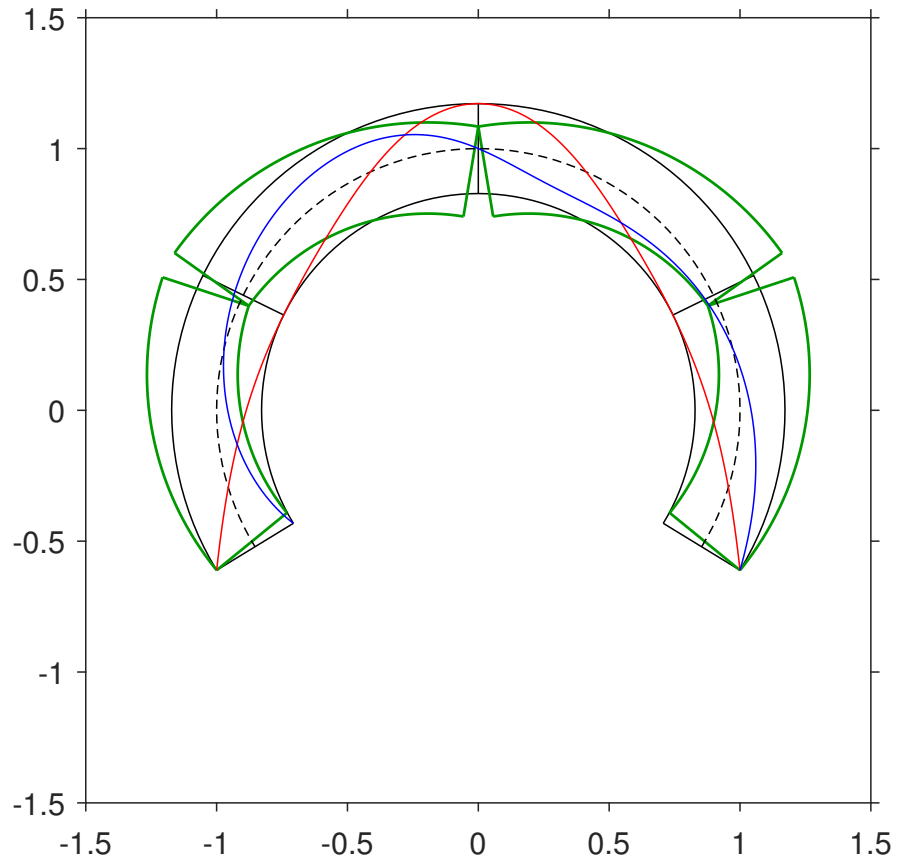


Figure 21: Least-thickness collapse mechanism, with line of thrust and line of friction at max  $\hat{h}$  ( $ss$ ) with  $\mu = 0.8448805850502447$  ( $\varphi \simeq 40.19^\circ$ ),  $\alpha = 2.119284332007852 \simeq 121.43^\circ$ ,  $\beta_r = 1.115492876804752 \simeq 63.91^\circ$ ,  $\eta = 0.3435759819418909$ ,  $\hat{h} = 0.1123019151906599$ : purely-rotational (top); sliding-rotational (low).

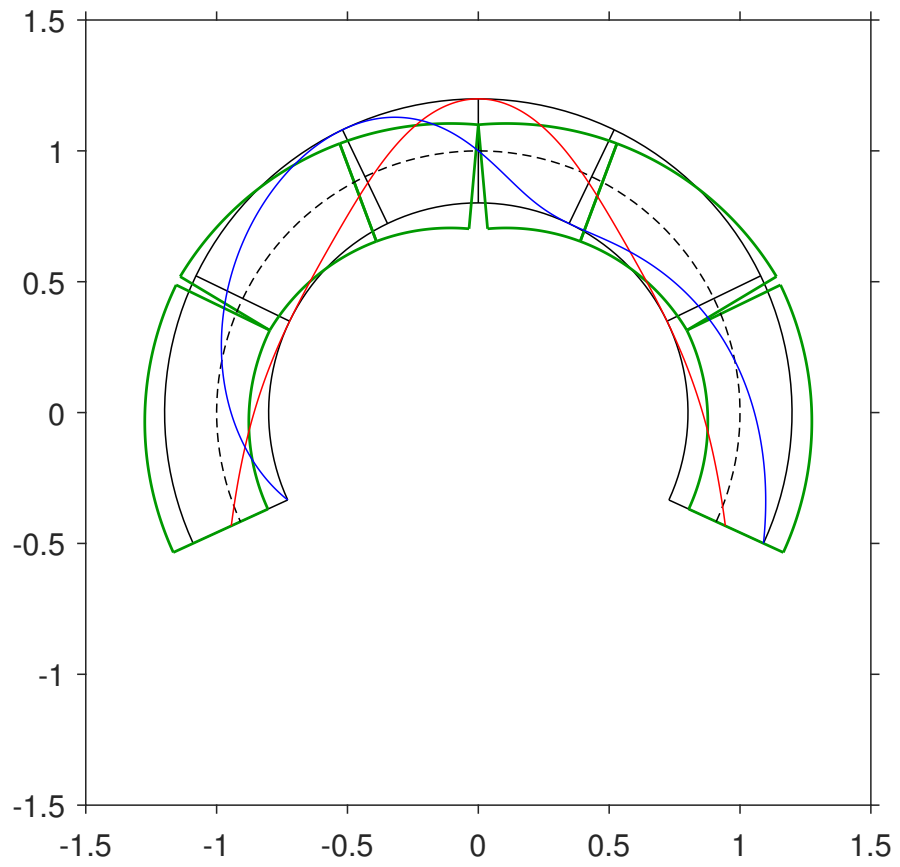
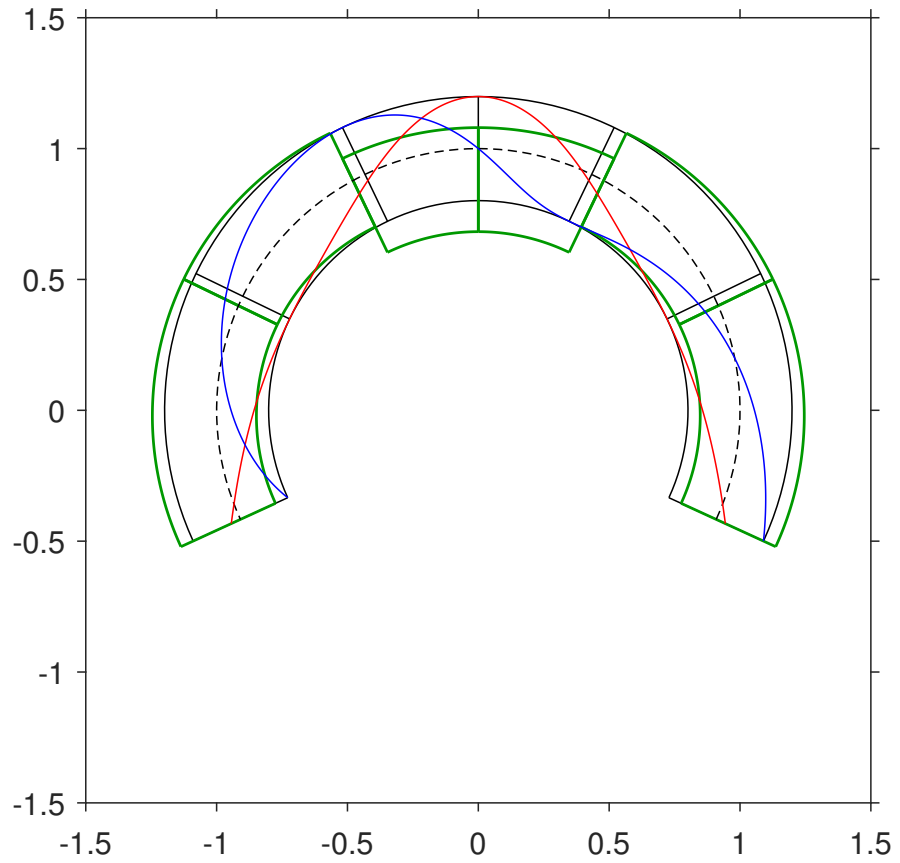


Figure 22: Least-thickness collapse mechanism, with line of thrust and line of friction at max  $\beta_r$  (*is*) with  $\mu = 0.6379887277366990$  ( $\varphi \simeq 32.54^\circ$ ),  $\alpha = 2.000761612520613 \simeq 114.64^\circ$ ,  $\beta_r = 1.119864231443752 \simeq 64.16^\circ$ ,  $\beta_s = 0.4478684050776427 \simeq 25.66^\circ$ ,  $\eta = 0.3975610062458916$ ,  $\hat{h} = 0.1104057302144935$ : purely-sliding (top); sliding-rotational (low).

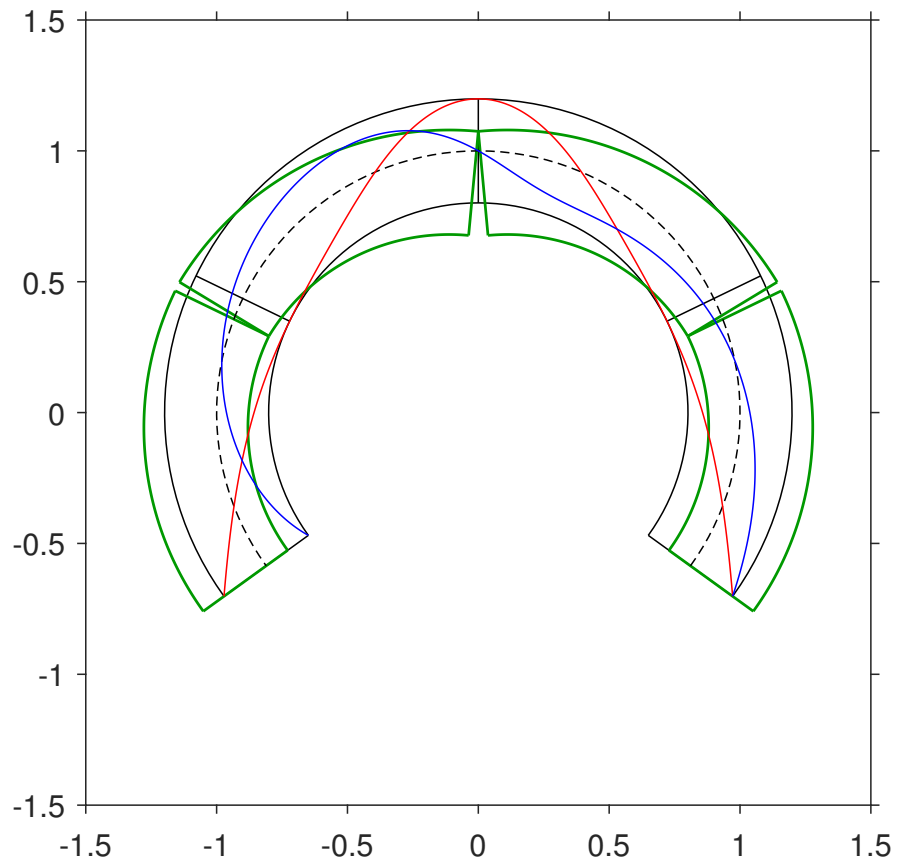
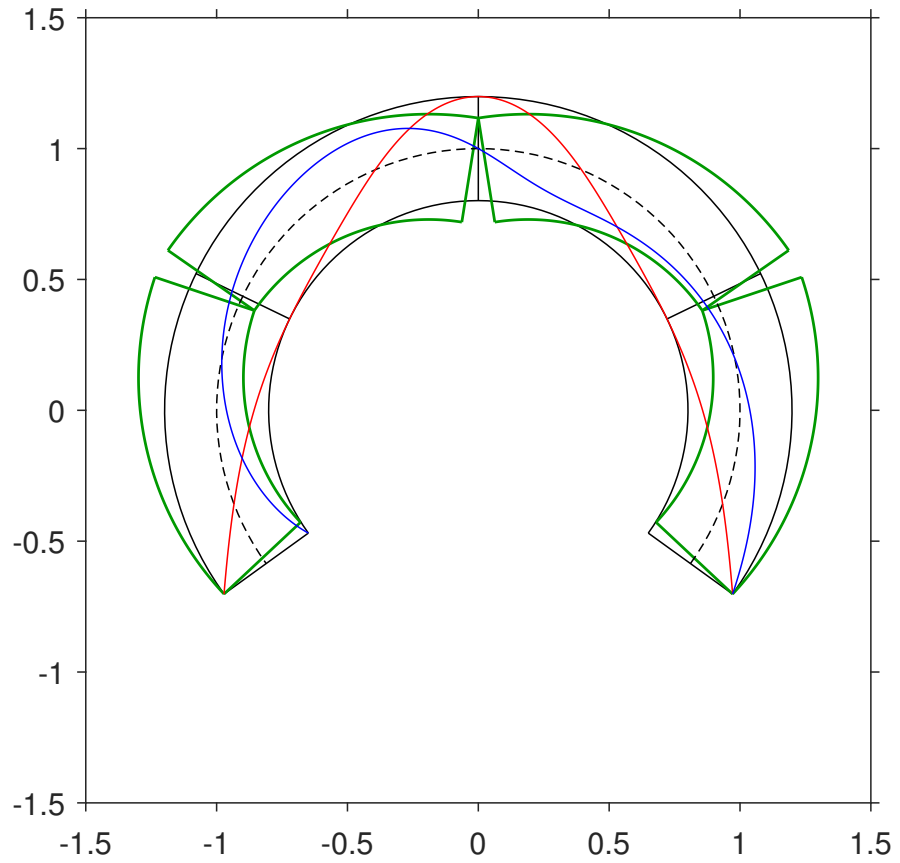


Figure 23: Least-thickness collapse mechanism, with line of thrust and line of friction at max  $\beta_r$  ( $ss$ ) with  $\mu = 0.9341739608482718$  ( $\varphi \simeq 43.05^\circ$ ),  $\alpha = 2.196404448812124 \simeq 125.84^\circ$ ,  $\beta_r = 1.119864231443752 \simeq 64.16^\circ$ ,  $\eta = 0.3975610062458916$ ,  $\hat{h} = 0.1104057302144935$ : purely-rotational (top); sliding-rotational (low).

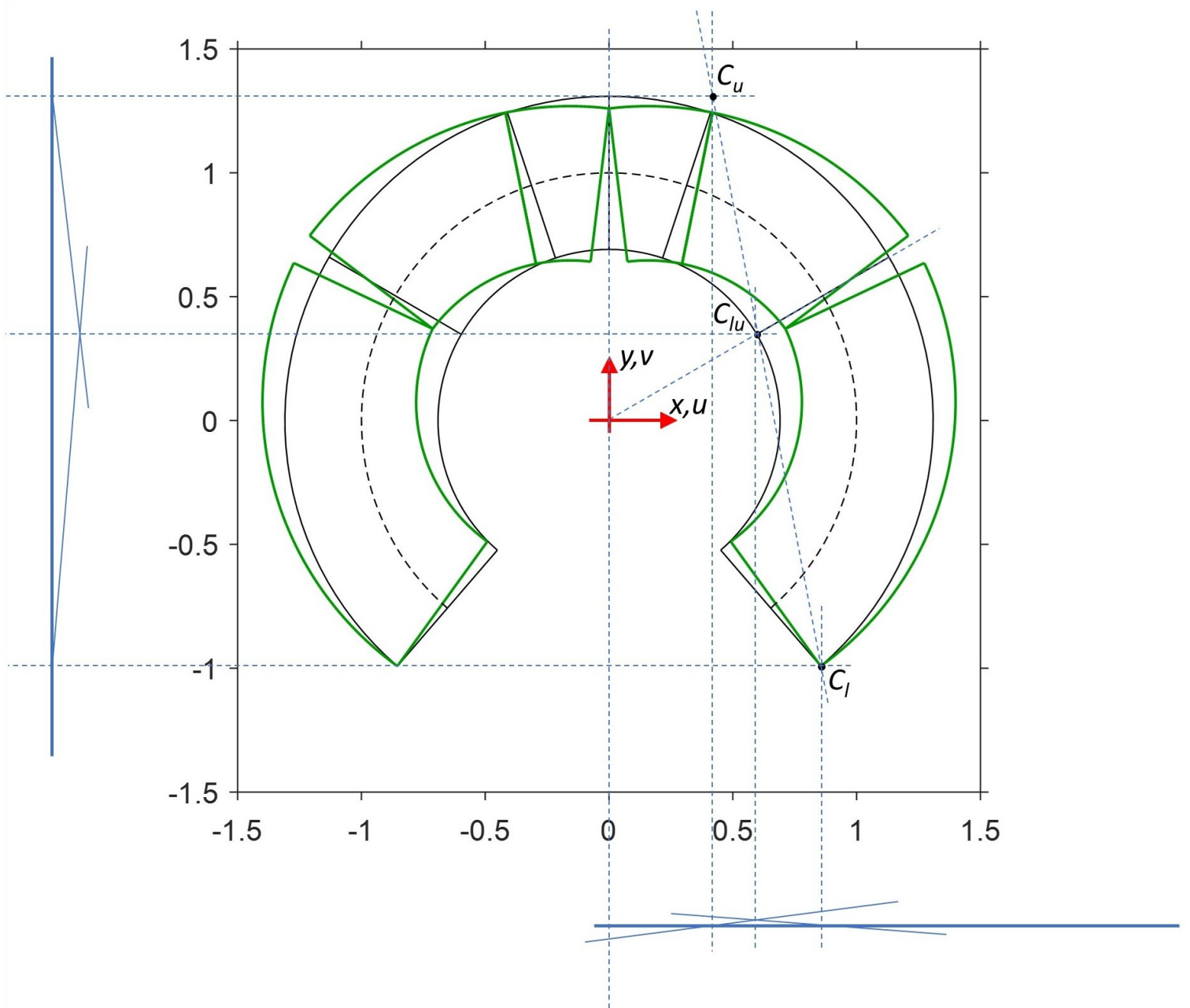


Figure 24: Kinematics of the Purely-Rotational collapse mode.

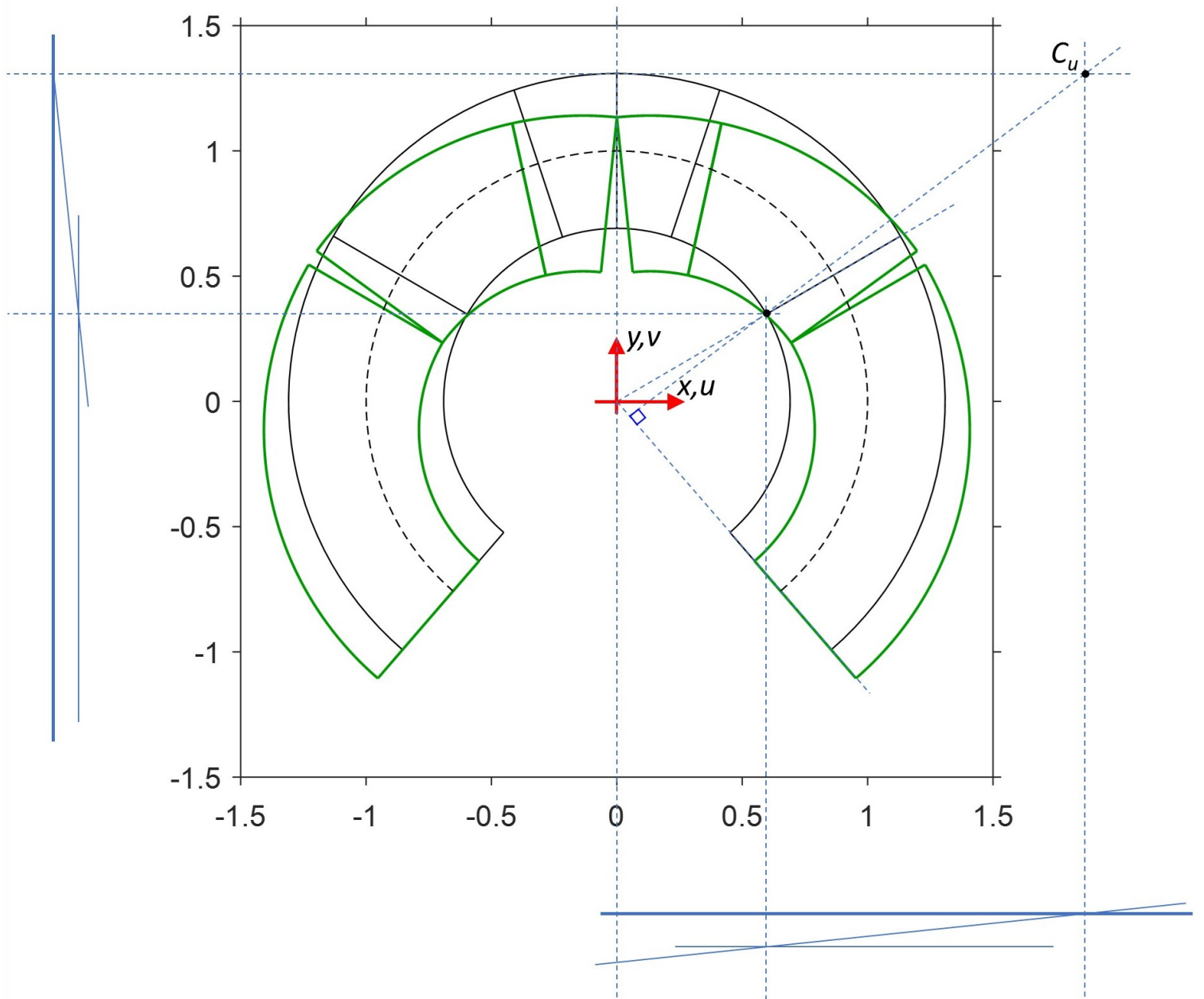


Figure 25: Kinematics of the mixed Sliding-Rotational collapse mode.

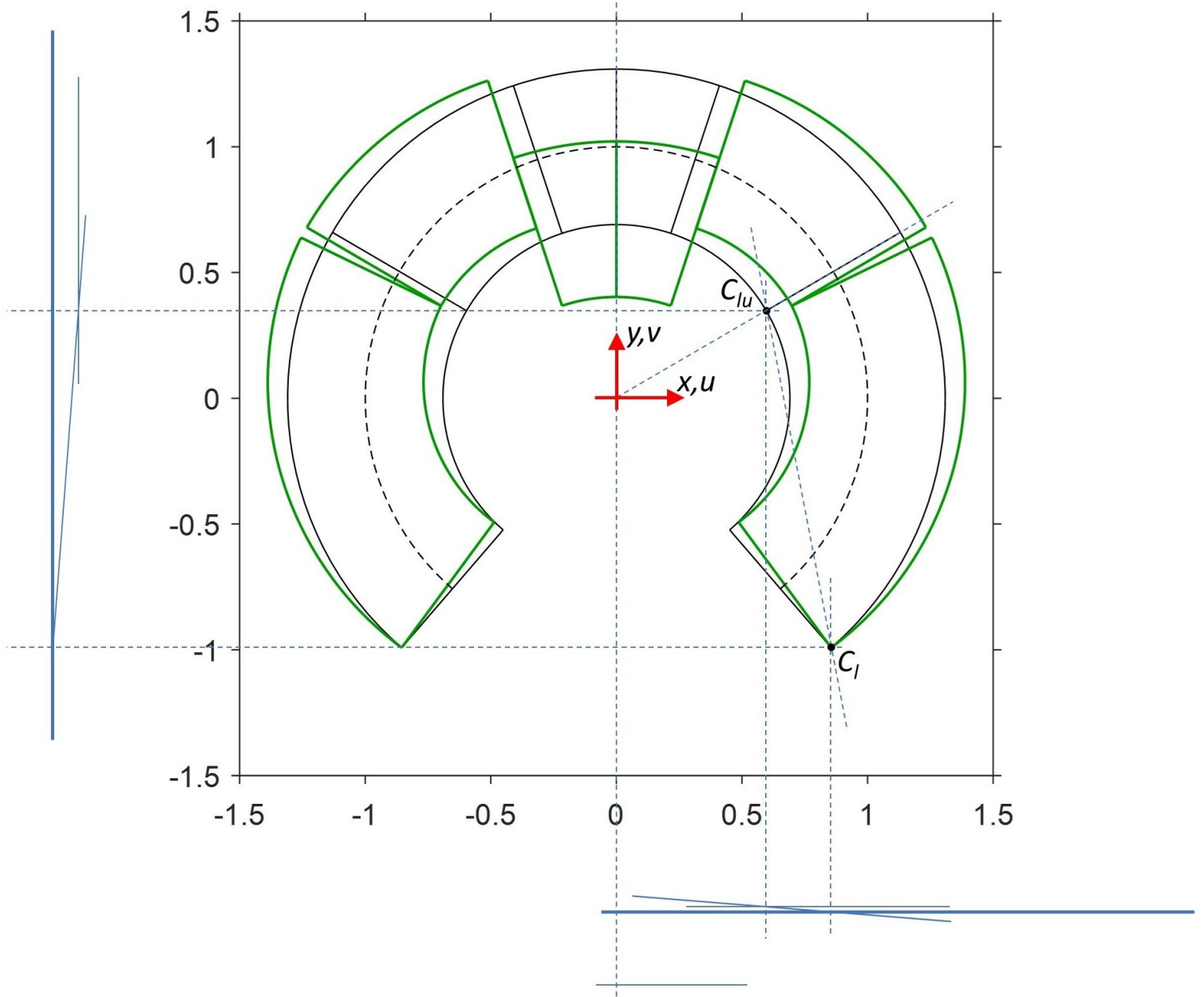


Figure 26: Kinematics of the mixed Rotational-Sliding collapse mode.

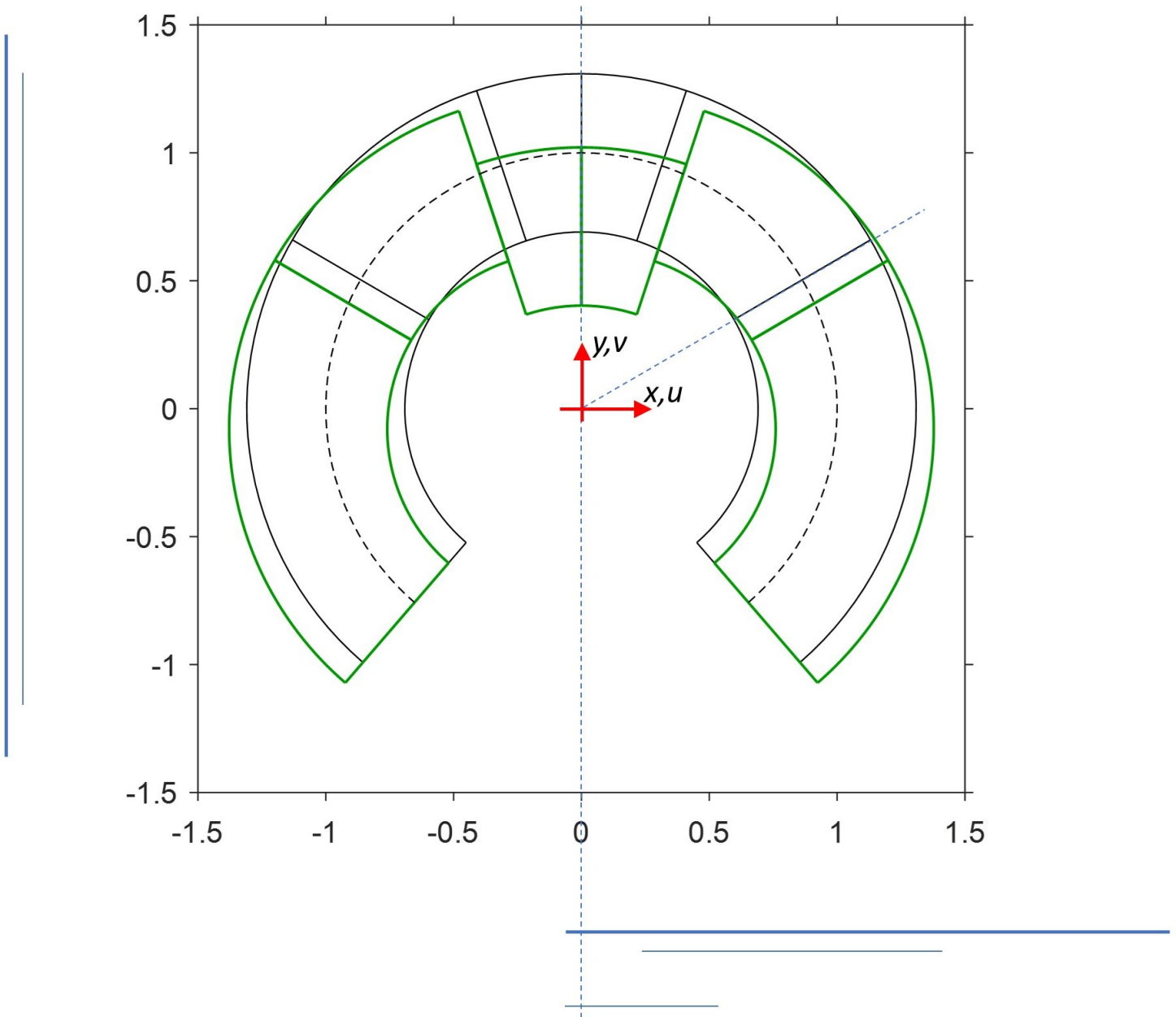


Figure 27: Kinematics of the Purely-Sliding collapse mode.